

---

Wayne State University Dissertations


---

January 2019

## Rare-Earth-Activated Group Vi D0 Metal Oxides As Thermosensitive Phosphors

Samarage Sameera Perera  
Wayne State University, sspperera@gmail.com

Follow this and additional works at: [https://digitalcommons.wayne.edu/oa\\_dissertations](https://digitalcommons.wayne.edu/oa_dissertations)

 Part of the [Inorganic Chemistry Commons](#), and the [Materials Science and Engineering Commons](#)

---

### Recommended Citation

Perera, Samarage Sameera, "Rare-Earth-Activated Group Vi D0 Metal Oxides As Thermosensitive Phosphors" (2019). *Wayne State University Dissertations*. 2289.  
[https://digitalcommons.wayne.edu/oa\\_dissertations/2289](https://digitalcommons.wayne.edu/oa_dissertations/2289)

This Open Access Dissertation is brought to you for free and open access by DigitalCommons@WayneState. It has been accepted for inclusion in Wayne State University Dissertations by an authorized administrator of DigitalCommons@WayneState.

**RARE-EARTH-ACTIVATED GROUP VI  $d^0$  METAL OXIDES AS  
THERMOSENSITIVE PHOSPHORS**

by

**SAMARAGE SAMEERA PRASAD PERERA**

**DISSERTATION**

Submitted to the Graduate School

of Wayne State University

Detroit, Michigan

in partial fulfillment of the requirements

for the degree of

**DOCTOR OF PHILOSOPHY**

2019

MAJOR: CHEMISTRY

Approved By:

---

Advisor

---

Date

## DEDICATION

To my mentors, family, and friends

## ACKNOWLEDGEMENTS

It is my great pleasure to pay my sincere gratitude to my advisor Prof. Federico A. Rabuffetti, for his continuous guidance throughout my Ph.D. research work in his laboratory at Wayne State University. I thank him for unwavering support and mentorship throughout my doctoral studies. With him, I learned how to conduct research towards academic excellence.

I am also grateful to Prof. Stephanie L. Brock, Prof. Mary Kay Pflum, and Prof. Ivan Avrutsky for serving on my Ph.D. committee, and providing valuable suggestions and feedback to improve my research.

I am indebted to our collaborator Prof. Leopoldo Suescun for sharing his sound knowledge in crystallography and structural characterization during his stay at the Wayne State University. I would also like to thank beamline scientists and staff members in 11-BM-B, 11-ID-B, and 20-BM-B beamlines at the Advanced Photon Source at Argonne National Laboratory for their help with my experiments.

I am very grateful to Prof. S.D.M. Chinthanka at the Department of Chemistry, University of Sri Jayewardenepura, for his guidance and support to complete my masters' degree.

Melissa Rochon does a wonderful job to ensure that graduate students fulfill all the requirements to complete their Ph.D. successfully. Her assistance is greatly appreciated. I am also grateful to other staff members of the chemistry department, including the late Mary Wood, Kellie Lauder, Diane Kudla (retired), Bernadette Miesik, Jacqueline Baldyga, and Tenecia Smith.

Thanks go to staff members in the Lumigen Instrument Center for their assistance with powder X-ray diffraction and ICP–MS experiments. Special thanks go to our system administrator Nestor Ocampo for resolving IT related issues.

I should also be thanking Science Store staff for helping me with purchasing materials and sample shipments.

It is my pleasure to thank all my labmates including, Tauni Dissanayake, Dinesh Amarasinghe, Dulani Dhanapala, Hashini Munasinghe, Regina Szlag, and Hermes Benicio for providing me an exciting environment and for their invaluable friendship. I also want to thank present and past undergraduate researchers in Rabuffetti group including Ci Lee, Emily Yatooma, Todd Yee, Natalie Mannino, and Laura Mendoza.

I gratefully acknowledge my true friends both in the United States and Sri Lanka. Especially, Dr. Ruchira Liyanage, Dr. Da Li, and Dr. Malsha Hettiarachchi for fruitful discussions about scientific research.

Last but not least, I am eternally grateful to my parents, wife, brother, and aunt for their unconditional love and support in all my endeavors. This journey would not have been possible without the support of my family.

## TABLE OF CONTENTS

Dedication.....	ii
Acknowledgements.....	iii
List of Figures.....	ix
List of Tables.....	xiv
Chapter 1. Introduction.....	1
1.1. Rare-Earth-Activated Materials for Optical Temperature Sensing.....	2
1.2 Applications of rare-earth-activated thermosensitive phosphors.....	10
1.3. Thesis Statement.....	12
1.3.1. Group VI $d^0$ Metal Oxides: Compositionally Tunable Hosts.....	13
1.3.2. Chemically Substituted $\text{Na}_w\text{La}(\text{MO}_4)_w$ as Thermosensitive Phosphors.....	15
1.4. Dissertation Organization.....	17
Chapter 2. Materials Synthesis and Characterization Techniques.....	18
2.1. Materials.....	18
2.2. Experimental Techniques.....	18
2.2.1. Synthesis.....	18
2.2.1.1. Conventional Solid-State Synthesis of $\text{NaLa}_{1-x}\text{RE}_x(\text{MoO}_4)_2$ .....	18
2.2.1.2. Conventional Solid-State Synthesis of $\text{NaLa}_{1-x}\text{RE}_x(\text{WO}_4)_2$ .....	19
2.2.1.3. Conventional Solid-State Synthesis of $\text{Na}_5\text{La}_{1-x}\text{RE}_x(\text{MoO}_4)_4$ .....	20
2.2.1.4. Conventional Solid-State Synthesis of $\text{Na}_5\text{La}_{1-x}\text{RE}_x(\text{WO}_4)_4$ .....	20
2.2.1.5. Microwave Heating.....	21
2.2.2. Materials Characterization.....	22
2.2.2.1. Powder X-ray Diffraction.....	22

2.2.2.2. Synchrotron Powder X-ray Diffraction .....	22
2.2.2.3 Rietveld Analysis .....	22
2.2.2.4. Inductively Coupled Plasma Mass Spectrometry (ICP–MS) .....	23
2.2.2.5. Room-Temperature Spectrofluorometry.....	23
2.2.2.6. Variable Temperature Spectrofluorometry .....	23
2.2.2.7. Luminescence Intensity Ratio.....	24
Chapter 3. Dysprosium-Activated Schelite-Type Oxides as Thermosensitive Phosphors.....	27
3.1. Introduction.....	27
3.2. Experimental.....	29
3.2.1. Solid-State Synthesis.....	29
3.2.1.2. Synthesis of $\text{NaLa}_{1-x}\text{Dy}_x(\text{MO}_4)_2$ and $\text{Na}_5\text{La}_{1-x}\text{Dy}_x(\text{MO}_4)_4$ (M = Mo, W)	29
3.2.2. Powder X-ray Diffraction (PXRD) .....	29
3.2.3. Rietveld Analysis .....	30
3.2.4. Variable-Temperature Spectrofluorometry .....	31
3.3. Results and Discussion .....	31
3.4. Conclusions.....	55
Chapter 4. Synthesis, Structural Characterization, and Room Temperature Photoluminescence of $\text{NaYb}(\text{MO}_4)_2$ (M = Mo, W) .....	56
4.1. Introduction.....	56
4.2. Experimental.....	58
4.2.1. Synthesis of $\text{NaYb}(\text{MoO}_4)_2$ and $\text{NaYb}(\text{WO}_4)_2$ .....	58
4.2.2. Synchrotron Powder X-ray Diffraction.....	58
4.2.3. Rietveld Analysis .....	59
4.2.4. Elemental Analysis.....	59

4.2.5. Upconversion Spectrofluorometry .....	59
4.3. Results and Discussion .....	60
4.4. Conclusions.....	71
Chapter 5. Europium-Activated NaYb(MO <sub>4</sub> ) <sub>2</sub> (M = Mo, W) as a Dual-Emitter	
Thermosensitive Phosphor.....	73
5.1. Introduction.....	73
5.2. Experimental .....	74
5.2.1. Solid-State Synthesis of NaYb <sub>0.95</sub> Eu <sub>0.05</sub> (MoO <sub>4</sub> ) <sub>2</sub> and NaYb <sub>0.95</sub> Eu <sub>0.05</sub> (WO <sub>4</sub> ) <sub>2</sub> .....	74
5.2.2. Powder X-ray Diffraction (XRD).....	75
5.2.3. Rietveld Analysis .....	75
5.2.4. Variable-Temperature Upconversion Spectrofluorometry.....	75
5.3. Results and Discussion .....	76
5.3.1. Structural Characterization of NaYb <sub>0.95</sub> Eu <sub>0.05</sub> (MO <sub>4</sub> ) <sub>2</sub> .....	76
5.3.2. Temperature-Dependent Photoluminescence.....	77
5.4. Conclusions.....	86
Chapter 6. Dysprosium and Praseodymium-Coactivated NaLa(MoO <sub>4</sub> ) <sub>2</sub>	
Thermosensitive Phosphor Using Microwave Heating .....	88
6.1. Introduction.....	88
6.2. Experimental .....	89
6.2.1. Synthesis.....	89
6.2.1.1. Synthesis of NaLa <sub>0.95</sub> Dy <sub>0.025</sub> Pr <sub>0.025</sub> (MoO <sub>4</sub> ) <sub>2</sub> Using Microwave Heating..	89
6.2.1.2. Conventional Solid-State Synthesis of NaLa <sub>0.975</sub> Dy <sub>0.025</sub> Pr <sub>0.025</sub> (MoO <sub>4</sub> ) <sub>2</sub> ..	90
6.2.2. Rietveld Analysis .....	90
6.2.3. Spectrofluorometry.....	91



6.3. Results and Discussion .....	91
6.3.1. Structural Characterization of $\text{NaLa}_{0.95}\text{Dy}_{0.025}\text{Pr}_{0.025}(\text{MoO}_4)_2$ .....	91
6.3.2. Steady-State Photoluminescence.....	93
6.3.2.1. Room-Temperature Steady-State Photoluminescence.....	93
6.3.2.2. Temperature-Dependent Steady-State Photoluminescence .....	93
6.4 Conclusions.....	100
Chapter 7. Conclusions and Perspectives .....	101
References .....	105
Appendix A. Permission/License Agreements for Copyrighted Materials .....	113
Appendix B. Permission/License Agreements for Copyrighted Materials.....	114
Abstract.....	115
Autobiographical Statement.....	117

## LIST OF FIGURES

<b>Figure 1.1.</b> Schematic representation of (a) downconversion (b) upconversion mechanisms. ....	3
<b>Figure 1.2.</b> Schematic diagram of an experimental setup used for surface temperature sensing of an object. Thermosensitive phosphor coated on the object is excited using a laser, and the emission is collected using a photomultiplier tube detector. ....	10
<b>Figure 1.3.</b> Connectivity of REO <sub>8</sub> and MO <sub>4</sub> polyhedra in (a) NaRE(MO <sub>4</sub> ) <sub>2</sub> and (b) Na <sub>5</sub> RE(MO <sub>4</sub> ) <sub>4</sub> . (c) REO <sub>8</sub> polyhedra in NaRE(MO <sub>4</sub> ) <sub>2</sub> share edges and are connected through RE–O–RE bridges. These polyhedral share corners with MO <sub>4</sub> polyhedra forming RE–O–M bridges. (d) REO <sub>8</sub> polyhedra in Na <sub>5</sub> RE(MO <sub>4</sub> ) <sub>4</sub> are isolated from each other and share corners with MO <sub>4</sub> polyhedra forming RE–O–M–O–RE bridges. ....	14
<b>Figure 2.1.</b> (a) Diagram of a typical reaction system employed to synthesize rare-earth activated NaLa(MoO <sub>4</sub> ) <sub>2</sub> using microwave heating. (b) Digital picture of the reaction system immediately after heating in the microwave oven for 3 minutes at a power of 900 W. ....	21
<b>Figure 2.2.</b> Energy level diagram of a rare-earth ion featuring thermally couple levels. (b) Temperature-dependent changes in the intensities of the photoluminescence emission bands corresponding to the transitions from thermally coupled levels to the ground state. ....	25
<b>Figure 3.1.</b> Dieke diagram of Dy <sup>3+</sup> depicting blue emission from the thermally coupled levels <sup>4</sup> I <sub>15/2</sub> and <sup>4</sup> F <sub>9/2</sub> . ....	28
<b>Figure 3.2.</b> Rietveld analysis of the NaLa <sub>1-x</sub> Dy <sub>x</sub> (MoO <sub>4</sub> ) <sub>2</sub> series. Experimental (○) and calculated patterns (—) are shown along with difference curves (—). Tick marks ( ) correspond to the calculated position of the diffraction maxima. ....	32
<b>Figure 3.3.</b> Rietveld analysis of the NaLa <sub>1-x</sub> Dy <sub>x</sub> (WO <sub>4</sub> ) <sub>2</sub> series. Experimental (○) and calculated patterns (—) are shown along with difference curves (—). Tick marks ( ) correspond to the calculated position of the diffraction maxima. ....	33
<b>Figure 3.4.</b> Rietveld analysis of the Na <sub>5</sub> La <sub>1-x</sub> Dy <sub>x</sub> (MoO <sub>4</sub> ) <sub>4</sub> series. Experimental (○) and calculated patterns (—) are shown along with difference curves (—). Tick marks ( ) correspond to the calculated position of the diffraction maxima. ....	34
<b>Figure 3.5.</b> Rietveld analysis of the Na <sub>5</sub> La <sub>1-x</sub> Dy <sub>x</sub> (WO <sub>4</sub> ) <sub>4</sub> series. Experimental (○) and calculated patterns (—) are shown along with difference curves (—). Tick marks ( ) correspond to the calculated position of the diffraction maxima. ....	35

- Figure 3.6.** Unit cell constants and volume ( $a$ ,  $c$ , and  $V$ ) as a function of the  $\text{Dy}^{3+}$  concentration are plotted for (e)  $\text{NaLa}_{1-x}\text{Dy}_x(\text{MoO}_4)_2$ , (f)  $\text{NaLa}_{1-x}\text{Dy}_x(\text{WO}_4)_2$ , (g)  $\text{Na}_5\text{La}_{1-x}\text{Dy}_x(\text{MoO}_4)_4$ , and (h)  $\text{Na}_5\text{La}_{1-x}\text{Dy}_x(\text{WO}_4)_4$ . Linear fits are depicted as dashed lines; the corresponding  $R^2$  residuals are given. .... 37
- Figure 3.7.** Temperature-dependent excitation and emission spectra of (a)  $\text{NaLa}_{0.95}\text{Dy}_{0.05}(\text{MoO}_4)_2$ , (b)  $\text{NaLa}_{0.975}\text{Dy}_{0.025}(\text{WO}_4)_2$ , (c)  $\text{Na}_5\text{La}_{0.9}\text{Dy}_{0.1}(\text{MoO}_4)_4$ , and (d)  $\text{Na}_5\text{La}_{0.9}\text{Dy}_{0.1}(\text{WO}_4)_4$ . Blue emission bands centered at 454 and 484 nm arise from the relaxation of the  $^4I_{15/2}$  and  $^4F_{9/2}$  thermally coupled levels of  $\text{Dy}^{3+}$ . Plots shown in the insets correspond to the room-temperature integrated intensity of the emission band at 484 nm as a function of the  $\text{Dy}^{3+}$  concentration; dashed lines are guides-to-the-eye. .... 38
- Figure 3.8.** Temperature-dependent excitation and emission spectra of the  $\text{NaLa}_{1-x}\text{Dy}_x(\text{MoO}_4)_2$  series in the 300–700 K temperature range. .... 39
- Figure 3.9.** Temperature-dependent excitation and emission spectra of the  $\text{NaLa}_{1-x}\text{Dy}_x(\text{WO}_4)_2$  series in the 300–700 K temperature range. .... 39
- Figure 3.10.** Temperature-dependent excitation and emission spectra of the  $\text{NaLa}_{1-x}\text{Dy}_x(\text{MoO}_4)_4$  series in the 300–700 K temperature range. .... 40
- Figure 3.11.** Temperature-dependent excitation and emission spectra of the  $\text{Na}_5\text{La}_{1-x}\text{Dy}_x(\text{WO}_4)_4$  series in the 300–700 K temperature range. .... 40
- Figure 3.12.** (a) Luminescence intensity ratio ( $R(T)$ ), (b) absolute sensitivity ( $S_A$ ), and (c) relative sensitivity ( $S_R$ ) of  $\text{NaLa}_{0.95}\text{Dy}_{0.05}(\text{MoO}_4)_2$ ,  $\text{NaLa}_{0.975}\text{Dy}_{0.025}(\text{WO}_4)_2$ ,  $\text{Na}_5\text{La}_{0.9}\text{Dy}_{0.1}(\text{MoO}_4)_4$ , and  $\text{Na}_5\text{La}_{0.9}\text{Dy}_{0.1}(\text{WO}_4)_4$ . Analytical expressions used to fit experimental  $R(T)$  values are given. The corresponding fits are depicted as dashed lines and  $R^2$  residuals are given. Dotted lines shown in (b) and (c) are guides-to-the-eye. .... 42
- Figure 3.13.** Luminescence intensity ratio ( $R(T)$ ), absolute sensitivity ( $S_A$ ), and relative sensitivity ( $S_R$ ) of phosphors belonging to the (a)  $\text{NaLa}_{1-x}\text{Dy}_x(\text{MoO}_4)_2$  and (b)  $\text{NaLa}_{1-x}\text{Dy}_x(\text{WO}_4)_2$  series. Analytical expressions used to fit experimental  $R(T)$  values are given. The corresponding fits are depicted as dashed lines and  $R^2$  residuals are given. Dotted lines shown in  $S_A(T)$  and  $S_R(T)$  plots are guides-to-the-eye. .... 43
- Figure 3.14.** Luminescence intensity ratio ( $R(T)$ ), absolute sensitivity ( $S_A$ ), and relative sensitivity ( $S_R$ ) of phosphors belonging to the (a)  $\text{Na}_5\text{La}_{1-x}\text{Dy}_x(\text{MoO}_4)_4$  and (b)  $\text{Na}_5\text{La}_{1-x}\text{Dy}_x(\text{WO}_4)_4$  series. Analytical expressions used to fit experimental  $R(T)$  values are given. The corresponding fits are depicted as dashed lines and  $R^2$  residuals are given. Dotted lines shown in  $S_A(T)$  and  $S_R(T)$  plots are guides-to-the-eye. .... 44

<b>Figure 3.15.</b> Arrhenius-type plots for phosphors belonging to the (a) $\text{NaLa}_{1-x}\text{Dy}_x(\text{MoO}_4)_2$ , $\text{NaLa}_{1-x}\text{Dy}_x(\text{WO}_4)_2$ , $\text{Na}_5\text{La}_{1-x}\text{Dy}_x(\text{MoO}_4)_4$ , and $\text{Na}_5\text{La}_{1-x}\text{Dy}_x(\text{WO}_4)_4$ .....	46
<b>Figure 3.16.</b> Map of relative sensitivity values at 350 and 700 K as a function of host composition and $\text{Dy}^{3+}$ concentration.....	48
<b>Figure 3.17.</b> Map of relative sensitivity values at 300 K as a function of host composition and $\text{Dy}^{3+}$ concentration.....	49
<b>Figure 3.18.</b> Luminescence intensity ratios of (a) $\text{NaDy}(\text{MoO}_4)_2$ and (b) $\text{Na}_5\text{La}_{0.5}\text{Dy}_{0.5}(\text{WO}_4)_4$ as a function of the heating–cooling cycle number.....	51
<b>Figure 4.1.</b> Crystal structure of $\text{NaYb}(\text{MO}_4)_2$ . $\text{Na}^+$ and $\text{Yb}^{3+}$ are depicted as statistically distributed over the same crystallographic site. The shortest distance between two adjacent Na/Yb sites in the unit cell is $\sim 3.8 \text{ \AA}$ .....	57
<b>Figure 4.2.</b> Rietveld analyses of the synchrotron XRD patterns of (a) $\text{NaYb}(\text{MoO}_4)_2$ and (b) $\text{NaYb}(\text{WO}_4)_2$ . The experimental ( $\circ$ ) and calculated ( $\text{---}$ ) patterns are shown along with the difference curve ( $\text{---}$ ) and the tick marks ( $ $ ). .....	60
<b>Figure 4.3.</b> Upconversion luminescence spectra of (a) $\text{NaYb}(\text{MoO}_4)_2$ and (b) $\text{NaYb}(\text{WO}_4)_2$ under 973 nm excitation (490 mW). Spectra collected between 300 and 850 nm (slit width $\sim 5$ nm) revealed strong NIR emission ( $\sim 795$ nm) due to two-photon upconversion of $\text{Yb}^{3+}$ -sensitized $\text{Tm}^{3+}$ impurities ( $\sim 1$ ppm). Insets: spectra collected between 450 and 700 nm (slit width $\sim 1$ nm) exhibited blue ( $\sim 475$ nm), green ( $\sim 510\text{--}560$ nm), and red ( $\sim 640\text{--}670$ nm) emission bands. Green and red emissions resulted from two-photon upconversion of $\text{Yb}^{3+}$ -sensitized $\text{Er}^{3+}$ impurities ( $\sim 1$ ppm). The likely origin of the blue emission was the cooperative interaction between a pair of neighboring $\text{Yb}^{3+}$ ions (see text for details). Digital pictures of the polycrystalline powders showing blue emission under 973 nm excitation (650 mW) are provided. ....	62
<b>Figure 4.4.</b> Dieke diagrams of $\text{Er}^{3+}$ , $\text{Yb}^{3+}$ , $\text{Yb}^{3+}\text{--Yb}^{3+}$ dimers, and $\text{Tm}^{3+}$ . Non-radiative energy-transfer from the $\text{Yb}^{3+}$ sensitizer to the $\text{Er}^{3+}$ and $\text{Tm}^{3+}$ activators is depicted with dotted arrows. Curly arrows indicate vibrational relaxation. Radiative emissions from $\text{Er}^{3+}$ , $\text{Tm}^{3+}$ , and $\text{Yb}^{3+}\text{--Yb}^{3+}$ dimers are indicated with solid arrows. ....	64
<b>Figure 4.5.</b> Double logarithmic plot showing the power dependence of the integrated intensities of the NIR ( $\circ$ , 795 nm), blue ( $\square$ , 475 nm), green ( $\triangle$ , 525 nm), and red ( $\diamond$ , 650 nm) emission bands of $\text{NaYb}(\text{MoO}_4)_2$ and $\text{NaYb}(\text{WO}_4)_2$ under 973 nm excitation. Linear fits are shown as dashed lines; the corresponding slopes ( $n$ ) and fit residuals ( $R^2$ ) are given. Note the linear dependence of the NIR upconversion emission in the entire power range. ....	65

- Figure 4.6.** Downconversion luminescence spectra of  $\text{NaYb}(\text{MoO}_4)_2$  and  $\text{NaYb}(\text{WO}_4)_2$  under 973 nm excitation (650 mW). ..... 70
- Figure 4.7.** Decay curves of the 475 and 1003 nm emissions of  $\text{NaYb}(\text{MoO}_4)_2$  (left panels) and  $\text{NaYb}(\text{WO}_4)_2$  (right panels) under 973 nm excitation (650 mW). Monoexponential fits are depicted as solid red lines; the corresponding lifetimes  $\tau$  are given..... 71
- Figure 5.1.** Rietveld analysis of the PXRD patterns of (a)  $\text{NaYb}_{0.95}\text{Eu}_{0.05}(\text{MoO}_4)_2$  and (b)  $\text{NaYb}_{0.95}\text{Eu}_{0.05}(\text{WO}_4)_2$ . Experimental ( $\circ$ ) and calculated ( $\text{---}$ ) patterns are shown along with the difference curve ( $\text{---}$ ). Tick marks ( $|$ ) correspond to the calculated positions of the diffraction maxima. .... 76
- Figure 5.2.** Temperature-dependent emission spectra of (a)  $\text{NaYb}_{0.95}\text{Eu}_{0.05}(\text{MoO}_4)_2$  and (b)  $\text{NaYb}_{0.95}\text{Eu}_{0.05}(\text{WO}_4)_2$  collected under 973 nm excitation. Spectra for  $\text{NaYb}_{0.95}\text{Eu}_{0.05}(\text{MoO}_4)_2$  and  $\text{NaYb}_{0.95}\text{Eu}_{0.05}(\text{WO}_4)_2$  were recorded in 100–500 and 100–600 K temperature range, respectively. The blue emission band centered at  $\sim 21065 \text{ cm}^{-1}$  ( $\sim 474 \text{ nm}$ ) originate from the cooperative emission of  $\text{Yb}^{3+}\text{--Yb}^{3+}$  dimers. The red emission band centered at  $16260 \text{ cm}^{-1}$  ( $\sim 615 \text{ nm}$ ) is due to the intraconfigurational f–f transition of  $\text{Eu}^{3+}$ . Weak bands in the green (at  $\sim 19000$  and  $18350 \text{ cm}^{-1}$ ) and red ( $\sim 15350 \text{ cm}^{-1}$ ) regions are due to the two-photon upconversion from  $\text{Er}^{3+}$  impurities. .... 78
- Figure 5.3.** Integrated intensities of blue and red bands of (a)  $\text{NaYb}_{0.95}\text{Eu}_{0.05}(\text{MoO}_4)_2$  and (b)  $\text{NaYb}_{0.95}\text{Eu}_{0.05}(\text{WO}_4)_2$  as a function of temperature. Quenching temperatures computed for both blue and red bands of  $\text{NaYb}_{0.95}\text{Eu}_{0.05}(\text{MoO}_4)_2$  are lower than the corresponding values computed for  $\text{NaYb}_{0.95}\text{Eu}_{0.05}(\text{WO}_4)_2$ . Digital pictures of the phosphors showing luminescence under 973 nm excitation are shown as the insets..... 80
- Figure 5.4.** Double logarithmic plots showing the power dependence of the integrated intensities of the blue ( $21065 \text{ cm}^{-1}$ ) and red ( $16260 \text{ cm}^{-1}$ ) emission bands of  $\text{NaYb}_{0.95}\text{Eu}_{0.05}(\text{MoO}_4)_2$  and  $\text{NaYb}_{0.95}\text{Eu}_{0.05}(\text{WO}_4)_2$  under 973 nm excitation. Linear fits are shown as dashed lines; the corresponding slopes ( $n$ ) and fit residuals( $R^2$ ) are given. .... 81
- Figure 5.5.** Dieke diagrams of  $\text{Yb}^{3+}$ ,  $\text{Yb}^{3+}\text{--Yb}^{3+}$  dimers, and  $\text{Eu}^{3+}$ . Non-radiative energy-transfer from  $\text{Yb}^{3+}\text{--Yb}^{3+}$  dimers to neighboring  $\text{Eu}^{3+}$  is depicted with a dashed-arrow. Curly arrows indicate vibrational relaxations. Radiative emission from  $\text{Yb}^{3+}\text{--Yb}^{3+}$  dimers and  $\text{Eu}^{3+}$  are indicated with solid arrows. .... 82
- Figure 5.6.** (a) Luminescence intensity ratio ( $R(T)$ ), (b) absolute sensitivity ( $S_A$ ), and (c) relative sensitivity ( $S_R$ ) of  $\text{NaLa}_{0.95}\text{Eu}_{0.05}(\text{MoO}_4)_2$  and  $\text{NaLa}_{0.95}\text{Eu}_{0.05}(\text{WO}_4)_2$ , Analytical expressions used to fit experimental  $R(T)$  values are given. The

	corresponding fits are depicted as dashed lines and $R^2$ residuals are given. Dotted lines shown in (b) and (c) are guides-to-the-eye. ....	84
<b>Figure 6.1.</b>	Dieke diagram of $Dy^{3+}$ and $Pr^{3+}$ ions. Intraconfigurational $f-f$ transitions responsible for emissions from $Dy^{3+}$ (blue and green) and $Pr^{3+}$ (red) observed in $NaLa_{0.95}Dy_{0.025}Pr_{0.025}(MoO_4)_2$ .....	89
<b>Figure 6.2.</b>	Rietveld analysis of the PXRD pattern of (a) $NaLa_{0.95}Dy_{0.025}Pr_{0.025}(MoO_4)_2$ experimental (○) and calculated (—) patterns are shown along with the difference curve (—). Tick marks ( ) correspond to the calculated positions of the diffraction maxima. (b) Comparison between the PXRD patterns of $NaLa_{0.95}Dy_{0.025}Pr_{0.025}(MoO_4)_2$ synthesized using conventional solid-state and microwave heating methods. ....	92
<b>Figure 6.3.</b>	Comparison of the photoluminescence (a) excitation and (b) emission spectra collected for $NaLa_{0.95}Dy_{0.025}Pr_{0.025}(MoO_4)_2$ synthesized using conventional solid-state and microwave heating methods. Nearly identical luminescence response was observed for both samples. ....	93
<b>Figure 6.4.</b>	Temperature-dependent (a) excitation and (b) emission spectra recorded in the 250–700 K temperature range for $NaLa_{0.95}Dy_{0.025}Pr_{0.05}(MoO_4)_2$ . Excitation spectra consisting of a series of narrow bands responsible for $f-f$ transitions are stronger than the charge-transfer band. Emission spectra exhibits bands originate from $Dy^{3+}$ (blue and green) and $Pr^{3+}$ (red). (c) Integrated intensities of the green ( $^4F_{9/2} \rightarrow ^6H_{13/2}$ ) and red ( $^1D_2 \rightarrow ^3H_4$ ) bands as a function of temperature. (d) The temperature-driven color change is displayed in the CIE diagram. $NaLa_{0.95}Dy_{0.025}Pr_{0.05}(MoO_4)_2$ powder luminescing at 250 (yellow) and 700 K (red) are shown in the insets.....	95
<b>Figure 6.5.</b>	(a) Luminescence intensity ratio ( $R(T)$ ), (b) absolute sensitivity ( $S_A$ ), and (c) relative sensitivity ( $S_R$ ) of $NaLa_{0.95}Dy_{0.025}Pr_{0.025}(MoO_4)_2$ in the low and high temperature regimes. Analytical expressions used to fit experimental $R(T)$ values are given. The corresponding fits are depicted as dashed lines and $R^2$ residuals are given. Dotted lines shown in (c)–(f) are guides-to-the-eye.....	99

## LIST OF TABLES

<b>Table 2.1.</b> Optimization of Synthesis Conditions for $\text{NaLa}_{1-x}\text{RE}_x(\text{MoO}_4)_2$ .....	19
<b>Table 2.2.</b> Optimization of Synthesis Conditions for $\text{NaLa}_{1-x}\text{RE}_x(\text{WO}_4)_2$ .....	19
<b>Table 3.1.</b> Synthesis Conditions for $\text{NaLa}_{1-x}\text{Dy}_x(\text{MoO}_4)_2$ and $\text{Na}_5\text{La}_{1-x}\text{Dy}_x(\text{MoO}_4)_4$ .....	30
<b>Table 3.2.</b> Structural Parameters of $\text{NaLa}_{1-x}\text{Dy}_x(\text{MoO}_4)_2$ and $\text{Na}_5\text{La}_{1-x}\text{Dy}_x(\text{MoO}_4)_4$ .....	36
<b>Table 3.3.</b> Experimental and Calculated Energy Gap Between Thermally Coupled Levels of $\text{Dy}^{3+}$ .....	47
<b>Table 3.4.</b> Relative Thermometric Sensitivities $S_R$ ( $\text{K}^{-1}$ ) of $\text{Dy}^{3+}$ -Activated Phosphors .....	50
<b>Table 3.5.</b> Repeatability of $\text{NaDy}(\text{MoO}_4)_2$ (at 700 K) and $\text{Na}_5\text{La}_{0.5}\text{Dy}_{0.5}(\text{WO}_4)_4$ (at 350 K) .....	51
<b>Table 3.6.</b> Thermometric Performance of $\text{Dy}^{3+}$ -Activated Phosphors.....	52
<b>Table 3.7.</b> Temperature Resolution of $\text{NaDy}(\text{MoO}_4)_2$ at 700 K.....	53
<b>Table 3.8.</b> Temperature Resolution of $\text{Na}_5\text{La}_{0.5}\text{Dy}_{0.5}(\text{WO}_4)_4$ at 350 K .....	54
<b>Table 4.1.</b> Structural Parameters of $\text{NaYb}(\text{MoO}_4)_2$ and $\text{NaYb}(\text{WO}_4)_2$ .....	61
<b>Table 5.1.</b> Structural Parameters of $\text{NaYb}_{0.95}\text{Eu}_{0.05}(\text{MoO}_4)_2$ and $\text{NaYb}_{0.95}\text{Eu}_{0.05}(\text{WO}_4)_2$ .....	77
<b>Table 5.2.</b> Maximum Relative Thermometric Sensitivities ( $S_{R \max}$ ) of Dual-Emitter Phosphors. ....	86
<b>Table 6.1.</b> Structural Parameters of $\text{NaLa}_{0.95}\text{Dy}_{0.025}\text{Pr}_{0.025}(\text{MoO}_4)_2$ .....	92
<b>Table 6.2.</b> Relative Thermometric Sensitivities of $\text{Dy}^{3+}$ and $\text{Pr}^{3+}$ -Activated Phosphors .....	98

## CHAPTER 1. INTRODUCTION

Phosphors is a class of materials that exhibits luminescence when excited using radiation such as ultraviolet, near-infrared (NIR), or an electron beam.<sup>1</sup> A typical phosphor consists of an inorganic host and rare-earth ions (i.e., activators), which emit light when excited.<sup>1</sup> These rare-earth-activated phosphors have been investigated as functional materials in areas such as solid-state lasers<sup>2-4</sup>, and solid-state lighting<sup>5-7</sup>. Recently, rare-earth activated materials have attracted the attention as phosphors for optical temperature sensing in the fields of engineering,<sup>8</sup> biosensing,<sup>9</sup> and electronics.<sup>10</sup> Thermosensitive phosphors consist of a host matrix and luminescent emitters offer a non-contact temperature sensing technique that uses distinct changes in the luminescence signal with temperature. The advantage of this method lies in its potential to determine the surface temperature of objects in challenging environments (e.g., gas turbines, hot gas streams, and nuclear power plants)<sup>11-12</sup> where conventional contact thermometry is difficult to apply. Recently, many types of rare-earth activated materials (e.g., glass,<sup>13</sup> oxides,<sup>14-15</sup> fluorides,<sup>16</sup> polymeric nanostructures,<sup>17</sup> and metal organic frameworks<sup>18</sup>) have been investigated as thermosensitive phosphors to probe cryogenic (below 250 K), physiological (303–313 K), intermediate (500–1000 K), and high (above 1000 K) temperatures. The promising behavior of thermosensitive phosphors featuring rare-earth ions make them ideal candidates for non-contact temperature sensing.

To exploit the potential of thermosensitive phosphors, they must be synthesized using the right combination of rare-earth activators and hosts. The performance of thermosensitive phosphors is often evaluated using their thermometric sensitivity (see equation 2.4). One of the major limitations of currently available thermosensitive phosphors is that they exhibit thermometric sensitivity less than  $0.5 \times 10^{-2} \text{ K}^{-1}$  at temperatures above 500 K. Therefore, researches over the last two decades have been focused on exploring new hosts–activator



combinations that could improve the thermometric performance of phosphors. Rare-earth-activated glasses, oxides, and polymers have been extensively investigated for cryogenic and intermediate temperature sensing,<sup>14, 19-21</sup> and some of these research work has been dedicated to developing new synthetic routes for rare-earth activated phosphors.<sup>22</sup> Very recently, Rabuffetti group reported rare-earth-activated fluorohalide and oxide phosphors (see **Chapter 3**) for low and intermediate temperature sensing, respectively.<sup>22-23</sup> This dissertation research is focused on the synthesis and investigation of thermometric response of rare-earth-activated group VI metal oxide thermosensitive phosphors with the aim of understanding how to tailor the thermometric response by rationally manipulating the chemical composition and the crystal structure of phosphors. The research work includes the development of synthetic methods to prepare rare-earth-activated group VI metal oxide phosphors of chemical formula  $(A)_x(RE)_y(MO_4)_w$  ( $A$  = alkaline or alkaline-earth;  $RE$  = yttrium and rare-earth;  $M$  = Mo, W), and investigating their thermometric response in intermediate temperatures.

This chapter describes the background information relevant to, synthesis, temperature-dependent thermometric response, and application of rare-earth-activated phosphors for temperature sensing.

### **1.1. Rare-Erath-Activated Materials for Optical Temperature Sensing**

Two types of rare-earth activated thermosensitive phosphors have been developed for optical temperature sensing: upconverting and downconverting phosphors. In downconverting thermosensitive phosphors, rare-earth ions such as  $Eu^{3+}$ ,  $Dy^{3+}$ , and  $Tb^{3+}$  have been extensively used as activators.<sup>15, 24-26</sup> Presence of a broad charge-transfer band in the excitation spectrum (e.g., in metalates) allows the excitation of these phosphors using UV, near-UV, and blue light. The subsequent transfer of energy from host to activator ions results in photoluminescence emission in

the visible or NIR region (i.e., Stokes emission) (see **Figure 1.1a**). In the case of upconverting phosphors, in addition to the activator, another rare-earth ion is used as the sensitizer. As shown in **Figure 1.1b**, upon excitation using NIR light, energy is absorbed by the sensitizer and transferred to the activator. As a result of sequential absorption of two or more photons by the sensitizer and subsequent transfer of energy to the activator ions leads to a photoluminescence emission at a shorter wavelength than the excitation wavelength (i.e., anti-Stokes emission).  $\text{Yb}^{3+}$  is commonly used as the sensitizer in upconverting phosphors as it has a large absorption cross-section in the NIR region ( $\sim 980$  nm).

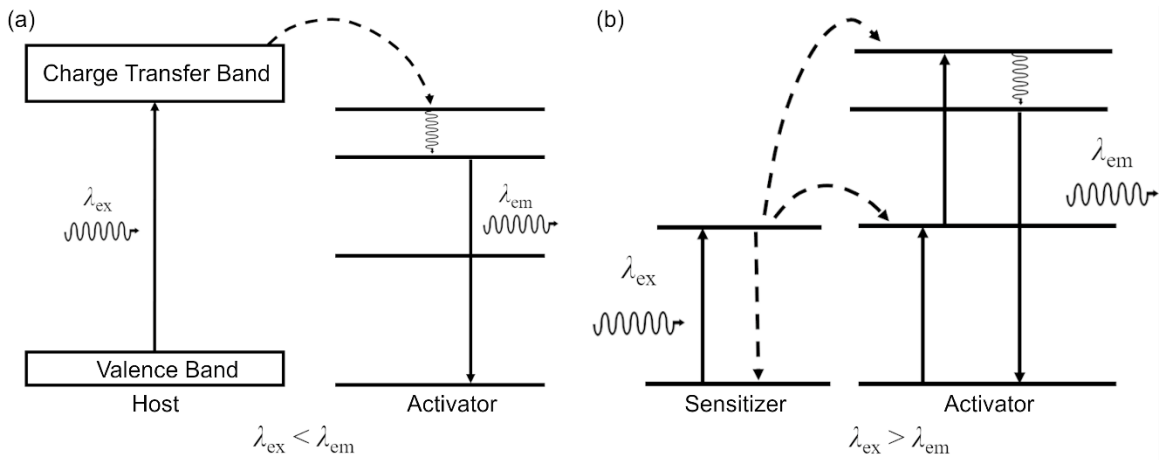


**Figure 1.1.** Schematic representation of (a) downconversion (b) upconversion mechanisms.

Over the past decade, rare-earth-activated upconverting glass materials have been studied for optical temperature sensing. Pisarski et al. studied the temperature-dependent luminescence response of rare-earth activated upconverting tungsten–tellurite glass.<sup>27</sup>  $\text{Yb}^{3+}$  and  $\text{Er}^{3+}$  were employed as sensitizer and activator, respectively.  $\text{Yb}^{3+}$  and  $\text{Er}^{3+}$  codoped tungsten–tellurite glass was synthesized using the melt quenching method. A mixture of  $\text{Yb}_2\text{O}_3$ ,  $\text{Er}_2\text{O}_3$ ,  $\text{WO}_3$ , and  $\text{TeO}_2$  was heated at  $700$  °C in a furnace until the material was converted into a transparent liquid. Then the hot liquid was quenched to room temperature to obtain rare-earth activated glass. Green

emission bands resulted from Yb<sup>3+</sup>-to-Er<sup>3+</sup> two-photon upconversion under 980 nm excitation was employed for optical temperature sensing. The temperature-dependent response of the green emission bands centered at 527 nm ( $^2H_{11/2} \rightarrow ^4I_{15/2}$ ) and 551 nm ( $^4S_{3/2} \rightarrow ^4I_{15/2}$ ) in 300–690 K temperature range was studied. Thermometric sensitivity reached to a maximum of  $2.8 \times 10^{-2} \text{ K}^{-1}$  at 500 K and then gradually decreased with temperature. Yb<sup>3+</sup> and Er<sup>3+</sup> codoped lead germanate glasses were also studied as optical temperature sensors by the same research group. Glass was synthesized by heating a mixture of PbO, GeO<sub>2</sub>, Ga<sub>2</sub>O<sub>3</sub>, Er<sub>2</sub>O<sub>3</sub>, and Yb<sub>2</sub>O<sub>3</sub> at 1100 °C until the material was melted. Transparent glass was obtained by quenching the melt to room temperature. The temperature-dependent response of green emission bands of Er<sup>3+</sup> activator under 980 nm was investigated in 300–620 K temperature range. Maximum thermometric sensitivity of  $1.4 \times 10^{-2} \text{ K}^{-1}$  was observed at 300 K. Although Er<sup>3+</sup> is often coupled with Yb<sup>3+</sup> to develop upconverting materials, Haouari et al. studied the downconversion luminescence of Er<sup>3+</sup>-doped fluoro-tellurite glass in 83–833 K temperature range under 476 nm excitation. Authors suggested that direct excitation of Er<sup>3+</sup> employing 476 nm provides a better signal-to-noise ratio for the photoluminescence emission at temperatures above 400 K than using 980 nm NIR light to excite Er<sup>3+</sup> via energy-transfer from Yb<sup>3+</sup> to Er<sup>3+</sup>. In Er<sup>3+</sup>-doped fluoro-tellurite glass, the thermometric sensitivity increased with temperature and reached a maximum of  $7.2 \times 10^{-3} \text{ K}^{-1}$  at 550 K. However, at temperatures above 550 K, sensitivity gradually decreased due to thermal quenching. In addition to thermal quenching, concentration quenching of the luminescence signal was also observed in Er<sup>3+</sup>-doped fluoro-tellurite glass and this was attributed to the clustering of rare-earth activator ions.

Recently, rare-earth-activated polymers and metal organic frameworks attracted the attention as materials for optical temperature sensing.<sup>28-29</sup> Miyata et al. reported the potential of employing

a coordination polymer activated with  $\text{Tb}^{3+}$  and  $\text{Eu}^{3+}$  for optical temperature sensing.<sup>28</sup> The polymer was synthesized by combining terbium and europium hexafluoro acetylacetonato ( $\text{Tb}_{1-x}\text{Eu}_x(\text{hfa})_3$ ) with 4,4-bis(diphenylphosphoryl) biphenyl  $[\text{Tb}_{0.99}\text{Eu}_{0.01}(\text{hfa})_3(\text{dpbp})]_n$ . Temperature-dependent luminescence response of the polymer was investigated in 200–400 K temperature range.  $\text{Tb}^{3+}$  in the rare-earth activated polymer was directly excited using 365 nm light to obtain the green emission ( $\sim 543$  nm) resulted from  $^5D_4 \rightarrow ^7F_5$  transition. The red emission ( $\sim 613$  nm) was observed as a result of the energy-transfer from  $\text{Tb}^{3+}$  ( $^5D_4$ ) to  $\text{Eu}^{3+}$  ( $^5D_1$ ). Temperature-dependent changes in the intensities of both green and red emission bands were employed for optical temperature sensing. Maximum thermometric sensitivity of  $0.83 \times 10^{-2} \text{ K}^{-1}$  was observed at 200 K. Although the maximum thermometric sensitivity was comparable to the other reported values for lanthanide coordination polymers, working temperature range of  $[\text{Tb}_{0.99}\text{Eu}_{0.01}(\text{hfa})_3(\text{dpbp})]_n$  was restricted to 200 K (200–400 K) due to the low thermal stability of the  $\text{Tb}_{0.99}\text{Eu}_{0.01}(\text{hfa})_3$  complex. Cui et al. investigated  $\text{Tb}^{3+}$  and  $\text{Eu}^{3+}$ -activated 2,5-dimethoxy-1,4-benzenedicarboxylate tetra hydrate  $[(\text{Eu}_x\text{Tb}_{1-x})_2(\text{DMBDC})_3(\text{H}_2\text{O})_4]$  as a mixed-lanthanide metal organic framework (MOF) thermometer in 10–300 K temperature range.<sup>18</sup> The luminescence emissions from  $\text{Tb}^{3+}$  and  $\text{Eu}^{3+}$  under 355 nm excitation was used to probe the temperature of the MOF. Interestingly, upon increasing the temperature from 10 to 300 K, the color of the photoluminescence emission changed from green to red. In this study, authors concluded that  $(\text{Eu}_x\text{Tb}_{1-x})_2(\text{DMBDC})_3(\text{H}_2\text{O})_4$  MOF is suitable for low temperature sensing (i.e., below 300 K) as it exhibited the maximum sensitivity at 10 K. Careful inspection of working temperature ranges and maximum thermometric sensitivities of the reported rare-earth activated polymers and metal organic frameworks reveals that these materials suffer from low thermal stability and luminescence quenching, which hinders their potential as optical temperature sensors.

Rabuffetti group recently reported a study on Yb<sup>3+</sup> and Er<sup>3+</sup> codoped SrFCl and SrFBr upconverting nanocrystals for optical temperature sensing. Temperature-dependent luminescence emission of Er<sup>3+</sup> activator was investigated in 100–450 K temperature range. Distinct changes in the intensities of the green emission bands at 525 ( $^2H_{11/2} \rightarrow ^4I_{15/2}$ ) and 545 nm ( $^4S_{3/2} \rightarrow ^4I_{15/2}$ ) were used for optical temperature sensing. Thermometric performance was investigated in two temperature regimes: low (100–275 K) and high (325–450 K). In the low-temperature regime, Yb:Er:SrFCl and Yb:Er:SrFBr displayed the maximum thermometric sensitivities of  $3.2 \times 10^{-2} \text{ K}^{-1}$  (125 K) and  $2.1 \times 10^{-2} \text{ K}^{-1}$  (175 K), respectively. In the high-temperature regime, sensitivities were  $9.4 \times 10^{-3} \text{ K}^{-1}$  (325 K) for Yb:Er:SrFCl and  $1.1 \times 10^{-2} \text{ K}^{-1}$  (300 K), for Yb:Er:SrFCl, respectively. These values were comparable to those observed in Yb:Er:NaYF<sub>4</sub> nanocrystals at 300 K. Rabuffetti group also focusses on developing rare-earth activated phosphors using metal oxide hosts such as molybdates,<sup>23</sup> tungstates,<sup>23</sup> niobates, tantalates and vanadates. Chemical and thermal stability, ability to incorporate rare-earth activators while preserving the average crystal structure make them ideal candidates as hosts for thermosensitive phosphors. These metal oxide hosts are doped with trivalent rare-earth ions to obtain photoluminescence emission under ultraviolet (UV) and near-infrared excitation. Rare-earth-activated metal oxides have been investigated as downconverting phosphors for optical temperature sensing in the intermediate and high temperatures. Meert and coworkers investigated the potential of CaEu<sub>2</sub>(WO<sub>4</sub>)<sub>4</sub> in the 300–475 K temperature range.<sup>30</sup> In their study, temperature-dependent changes in the intensities of photoluminescence emission bands originating from  $^5D_1 \rightarrow ^7F_0$  (~535 nm) and  $^5D_0 \rightarrow ^7F_0$  (~585 nm) transitions of Eu<sup>3+</sup> were used for temperature sensing. Maximum thermometric sensitivity of  $1.4 \times 10^{-2} \text{ K}^{-1}$  was observed at 300 K. However, the thermometric sensitivity decreased with temperature and reached a minimum of  $4.7 \times 10^{-3} \text{ K}^{-1}$  at 475 K indicating the negative impact of

thermal quenching on the thermometric performance of the phosphor. Dy<sup>3+</sup>-activated Y<sub>3</sub>Al<sub>5</sub>O<sub>12</sub> was investigated as a thermosensitive phosphor in 293–1293 K temperature range by Chepyga et al.<sup>19</sup> Distinct changes in intensities of the photoluminescence emission bands of Dy<sup>3+</sup> centered at 458 nm (<sup>4</sup>I<sub>15/2</sub> → <sup>6</sup>H<sub>15/2</sub>) and 483 nm (<sup>4</sup>F<sub>9/2</sub> → <sup>6</sup>H<sub>15/2</sub>) were employed to determine the temperature of the phosphors. Further, in this study, the potential of employing a mixture of two Dy<sup>3+</sup>-activated phosphors for optical temperature sensing was investigated. Five phosphor mixtures with different compositions were prepared by varying the ratio between Dy:YAlO<sub>3</sub> and Dy:Y<sub>3</sub>Al<sub>5</sub>O<sub>12</sub>. Their thermometric performance was investigated in 293–1293 K temperature range. The phosphor mixture consists of 85 % (W/W) Dy<sup>3+</sup>-activated YAlO<sub>3</sub> exhibited the highest thermometric performance. However, similar to what was observed by Meert and coworkers, the thermometric performance of the phosphor mixtures deteriorated with temperature due to thermal quenching. Hertle et al. suggested codoping different rare-earth ions in a single host as a strategy to overcome the effect of thermal quenching on thermometric performance of downconverting phosphors.<sup>19</sup> The attempts were made to utilize the energy-transfer between different rare-earth ions to mitigate the effect of thermal quenching. In their work, temperature-dependent luminescence response of Dy:Tb:Y<sub>3</sub>Al<sub>5</sub>O<sub>12</sub> and Dy:Tm:Y<sub>3</sub>Al<sub>5</sub>O<sub>12</sub> were investigated in 300–1600 K temperature range. Interestingly, Dy:Tb:Y<sub>3</sub>Al<sub>5</sub>O<sub>12</sub> exhibited two-fold improvement in thermometric sensitivity compared to Dy:Y<sub>3</sub>Al<sub>5</sub>O<sub>12</sub>. This considerable improvement in thermometric sensitivity was attributed to the energy-transfer between Dy<sup>3+</sup> and Tb<sup>3+</sup>, which improved the luminescence signal originated from <sup>4</sup>F<sub>9/2</sub> → <sup>6</sup>H<sub>15/2</sub> (~483 nm) transition in Dy<sup>3+</sup>. In contrast, Dy<sup>3+</sup> and Tm<sup>3+</sup> codoped Y<sub>3</sub>Al<sub>5</sub>O<sub>12</sub> did not display any improvements in the photoluminescence emission. In fact, upon codoping Y<sub>3</sub>Al<sub>5</sub>O<sub>12</sub> with Dy<sup>3+</sup> and Tm<sup>3+</sup>, the intensity of the photoluminescence emission band from Dy<sup>3+</sup> (~483 nm) decreased. This was attributed to the energy-transfer from <sup>4</sup>F<sub>9/2</sub> level of Dy<sup>3+</sup>

to  $^1G_4$  level of  $Tm^{3+}$ . As a result of this energy transfer, electron population in the  $^4F_{9/2}$  level of  $Dy^{3+}$  decreased, which reduced the intensity of the photoluminescence emission band at  $\sim 483$  nm. Although the authors suggested that  $Dy^{3+}:Tb^{3+}:Y_3Al_5O_{12}$  has the potential to be used as a thermosensitive phosphor in high-temperatures (i.e., above 1000 K), decrease in thermometric sensitivity with temperature was identified as a major limitation.

Rare-earth-activated metal oxides have also been investigated as upconverting thermosensitive phosphors. Owing to the efficient energy-transfer between  $Yb^{3+}$  and  $Er^{3+}$  ions,  $Yb^{3+}$ - $Er^{3+}$  sensitizer-activator pair has been intensively employed in upconverting thermosensitive phosphors.<sup>27, 31-33</sup> Yang and coworkers studied the temperature-dependent photoluminescence response of  $Yb^{3+}$  and  $Er^{3+}$  codoped  $NaY(MoO_4)_2$  prepared using hydrothermal synthesis.<sup>33</sup> Two green bands at  $\sim 536$  and  $\sim 558$  nm resulted from  $Yb^{3+}$ -to- $Er^{3+}$  two-photon upconversion were employed for temperature sensing. Bands centered at  $\sim 536$  and  $\sim 558$  nm were attributed to the  $^2H_{11/2} \rightarrow ^4I_{15/2}$  and  $^4S_{3/2} \rightarrow ^4I_{15/2}$  transitions of  $Er^{3+}$ , respectively. The dependence of the intensities of green emission bands on  $Er^{3+}$  and  $Yb^{3+}$  concentrations and the temperature were studied. First, the dependence of the photoluminescence emission intensity on  $Er^{3+}$  concentration was studied. Room temperature photoluminescence of series of phosphors of chemical formula  $NaY_{0.95-x}Yb_{0.05}Er_x(MoO_4)_2$  ( $x = 0.01, 0.02, \text{ and } 0.03$ ) was investigated to this end. The highest photoluminescence emission intensity of the green bands was observed for  $NaY_{0.93}Yb_{0.05}Er_{0.02}(MoO_4)_2$ . Next,  $Yb^{3+}$  concentration was systematically varied while keeping the  $Er^{3+}$  concentration at  $x = 0.02$ . Room temperature photoluminescence of series of phosphors of chemical formula  $NaY_{0.98-x}Yb_xEr_{0.02}(MoO_4)_2$  was investigated, and the highest emission intensity of the green bands was obtained for  $NaY_{0.88}Yb_{0.1}Er_{0.02}(MoO_4)_2$ . Based on the results of room temperature photoluminescence studies,  $NaY_{0.88}Yb_{0.1}Er_{0.02}(MoO_4)_2$  was employed for optical

temperature sensing. Phosphor was excited using 980 nm laser and the photoluminescence emission was recorded in 303–503 K temperature range. Upon increasing the temperature, thermometric sensitivity gradually increased and reached a maximum value of  $0.97 \times 10^{-2} \text{ K}^{-1}$  at 493 K. However, at temperatures above 493 K, thermometric sensitivity gradually decreased due to the effect of thermal quenching. In another study, Quintanilla et al. investigated the potential of employing Yb:Er:LiNbO<sub>3</sub> as a phosphor for optical temperature sensing.<sup>32</sup> Green emission band originated from  ${}^2H_{11/2} \rightarrow {}^4I_{15/2}$  (~530 nm) and  ${}^4S_{3/2} \rightarrow {}^4I_{15/2}$  (~550 nm) transitions in Er<sup>3+</sup> activator was employed for optical temperature sensing. Temperature-dependent luminescence response of microcrystalline LiNbO<sub>3</sub> particles with dopant contents of 0.2 mol% (Er<sup>3+</sup>) and 0.7 mol% (Yb<sup>3+</sup>) was investigated in 285–773 K, and the highest thermometric sensitivity of  $\sim 1.4 \times 10^{-2} \text{ K}^{-1}$  was obtained at 400 K. Careful evaluation of thermometric performance of already reported upconverting phosphors featuring Yb<sup>3+</sup>–Er<sup>3+</sup> sensitizer–activator pair reveals that the thermometric sensitivity gradually decreases at temperatures above 400 K.

Although Yb<sup>3+</sup>–Er<sup>3+</sup> has been intensively employed as a sensitizer–activator pair in upconverting thermosensitive phosphors, Yb<sup>3+</sup>–Tm<sup>3+</sup><sup>34</sup> and Yb<sup>3+</sup>–Ho<sup>3+</sup><sup>5</sup> have also been investigated as sensitizer–activator pairs in upconverting thermosensitive phosphors. Lojpur et al. studied the thermometric response of Yb:Tm:Y<sub>2</sub>O<sub>3</sub> and Yb:Ho:Y<sub>2</sub>O<sub>3</sub> in 10–300 K temperature range.<sup>21</sup> In Yb:Tm:Y<sub>2</sub>O<sub>3</sub>, blue ( ${}^1G_4 \rightarrow {}^3H_6$ ) and NIR ( ${}^3H_4 \rightarrow {}^3H_6$ ) photoluminescence emissions from Tm<sup>3+</sup> was used for optical temperature sensing, and the maximum sensitivity of  $0.78 \times 10^{-2} \text{ K}^{-1}$  was obtained at 250 K. In the case of Yb:Ho:Y<sub>2</sub>O<sub>3</sub>, green (~550 nm) and red (~755 nm) emission bands resulted from  ${}^5S_2 \rightarrow {}^5I_8$  and  ${}^5S_2 \rightarrow {}^5I_7$  transition of Ho<sup>3+</sup> were used for temperature sensing, respectively. Maximum thermometric sensitivity of  $0.46 \times 10^{-2} \text{ K}^{-1}$  was obtained at 85 K. The outcome of these two studies suggested that both Yb:Tm:Y<sub>2</sub>O<sub>3</sub> and Yb:Ho:Y<sub>2</sub>O<sub>3</sub> upconverting



phosphors are suitable for cryogenic temperature sensing as they show their maximum thermometric sensitivities at temperatures below 300 K.

## 1.2 Applications of rare-earth-activated thermosensitive phosphors

In the field of engineering, rare-earth-activated thermosensitive phosphors have been employed to probe the surface temperature distribution of objects such as propeller blades in gas turbines,<sup>35</sup> micro-electronics,<sup>10</sup> and hot gas and liquid streams.<sup>35</sup> In addition, the temperature inside combustion engines have also been determined using rare-earth-activated thermosensitive

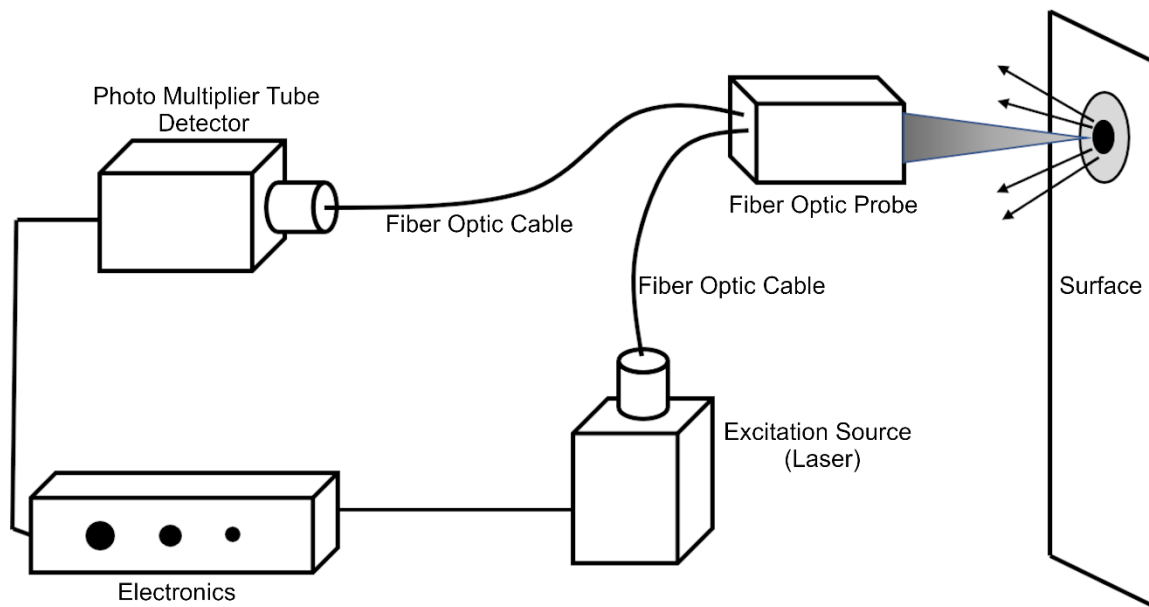


**Figure 1.2.** Schematic diagram of an experimental setup used for surface temperature sensing of an object. Thermosensitive phosphor coated on the object is excited using a laser, and the emission is collected using a photomultiplier tube detector.

phosphors.<sup>36</sup> **Figure 1.2** shows the simplified schematic diagram of the setup, which is used to determine the surface temperature of objects using rare-earth activated thermosensitive phosphors. First, the thermosensitive phosphor is coated on the surface, and then it is excited using an excitation source (laser). Power of the laser is controlled to provide enough energy to excite the phosphor. Photoluminescence emission is collected either using a photomultiplier tube (PMT) detector or an Intensified Charged Coupled Device (ICCD) camera.

Aldén et al. has studied the potential of using Eu:BaMg<sub>2</sub>Al<sub>10</sub>O<sub>17</sub> (BAM), which is one of the commercially available thermosensitive phosphors to measure the surface temperature of gas turbine rotor blades spinning at a 21000 rpm.<sup>37</sup> The blades were spray-coated with Eu:BaMg<sub>2</sub>Al<sub>10</sub>O<sub>17</sub>, and excited using a Nd:YAG laser that produces 355 nm UV light. An ICCD camera equipped with filters were used to record the images. Authors have highlighted the advantage of employing phosphors with a short lifetime for 2D measurements on fast-moving objects. Measurements have also been made at a single point of the propeller surface using Eu:Mg<sub>4</sub>FGeO<sub>6</sub> as a thermosensitive phosphor. Phosphor was excited at 266 nm using a Nd:YAG laser, and the photoluminescence emission from Eu<sup>3+</sup> was detected with a photomultiplier tube detector. In this study, authors were able to measure the temperature at a precision of 97 % at 1000 K revealing the potential of employing rare-earth activated phosphors for high-temperature sensing. Measuring the temperature of a liquid or a gas stream is one of the major challenges encountered in the fields of mechanical and chemical engineering.<sup>35</sup> As a promising solution, rare-earth activated thermosensitive phosphors have been employed to measure the temperature of laminar and turbulent fluid streams. Omrane et al. has measured the temperature of a heated gas flow using Eu:Mg<sub>4</sub>FGeO<sub>6</sub> as a thermosensitive phosphor. First, phosphor particles were seeded into the hot gas, and then the gas stream was sent through a nozzle. Phosphor particles were excited using Nd:YAG laser, and the emission was detected using an ICCD camera equipped with filters. The temperature of the gas was probed under both turbulent and laminar flow conditions. In a similar study, temperature of a hot gas stream was probed using Yb:Er:Y<sub>2</sub>O<sub>2</sub>S upconverting thermosensitive phosphor.<sup>38</sup> However, owing to the thermal quenching of the phosphor, authors were unable to measure the temperature above 473 K. Measuring the temperature of a moving solvent droplet is a challenging task to perform using conventional temperature sensing methods

such as thermometers and thermocouples. Traditionally, infrared thermometers have been used to determine the temperature of oil or solvent droplets that comes out of a nozzle. The change in the radius of the infrared beam with distance from the optical aperture (beam divergence) makes the temperature measurements of small objects less reliable using infrared thermometers. Omrane and coworkers have successfully mapped the temperature distribution of a freefalling hot toluene droplet using Eu:Y<sub>2</sub>O<sub>2</sub>S as thermosensitive phosphor.<sup>39</sup> Temperature of the core and the outer surface of the toluene droplet was determined as ~328 and 381 K, respectively. The experimental outcomes of these studies reveal the potential of employing rare-earth-activated thermosensitive phosphors for temperature determination in environments where conventional temperature sensing methods are not possible.

### 1.3. Thesis Statement

Current library of thermosensitive phosphors consists of large number of rare-earth activated oxide thermosensitive phosphors. However, these thermosensitive phosphors offer limited thermometric sensitivity and suffer from thermal quenching in the intermediate temperature range (i.e., 500–1000 K). The rational design of thermosensitive phosphors that show adequate thermometric sensitivity (i.e. higher than  $0.5 \times 10^{-2} \text{ K}^{-1}$  at temperatures above 500 K) and low thermal quenching in intermediate temperatures remains challenging. To address this challenge, it is essential to acquire knowledge on how to utilize the phosphor's chemical composition and the crystal structure as levers to tailor the thermometric response. This dissertation seeks to bridge this knowledge gap through a systematic investigation of the temperature-dependent luminescence response of phosphors derived from chemically and structurally tunable hosts. Group VI  $d^0$  metal oxides of chemical formula  $A_u\text{RE}_v(\text{MO}_4)_w$  (A = alkaline or alkaline-earth; RE = yttrium and rare-earth; M = Mo, W) consisting of MO<sub>4</sub> and REO<sub>8</sub>

building blocks are used as hosts. Employing these chemically and structurally tunable hosts allows to systematically investigate the composition- and structure-related changes in temperature-dependent luminescence response of thermosensitive phosphors. This, in turn, should lay the groundwork to design thermosensitive phosphors with tailored thermometric response.

### 1.3.1. Group VI $d^0$ Metal Oxides: Compositionally Tunable Hosts

Due to their compositional and structural tunability, scheelite-type and scheelite-related group VI  $d^0$  metal oxides of chemical formula  $A_uRE_v(MO_4)_w$  have been widely investigated as functional materials in the fields of solid-state lighting,<sup>40-41</sup> solid-state lasers,<sup>42-43</sup> optical temperature-sensing,<sup>30</sup> and light upconversion.<sup>44</sup> Compositional and structural tunability make group VI metalates an ideal family of materials to identify design principles for thermosensitive phosphors. In this dissertation, double and quadruple metalates of chemical formulas  $NaLa(MO_4)_2$  and  $Na_5La(MO_4)_4$ , respectively are investigated as hosts for thermosensitive phosphors. Crystal structures of  $NaLa(MO_4)_2$  and  $Na_5La(MO_4)_4$  are displayed in **Figures 1.1a and b**, respectively. Both metalates crystallize in the  $I4_1/a$  tetragonal space-group.<sup>45</sup> The building block of these oxides consists of  $MO_4$  tetrahedra isolated from each other. The connectivity of the  $REO_8$  and  $MO_4$  polyhedra in  $NaLa(MO_4)_2$  and  $Na_5La(MO_4)_4$  are shown in **Figures 1.1c and d**, respectively. In double metalates, sodium and rare-earth ions are statistically distributed over the  $4b$  site and are coordinated by eight oxide ions forming  $NaO_8$  and  $REO_8$  dodecahedra. Each  $Na/REO_8$  polyhedron shares edges with four neighboring  $Na/REO_8$  polyhedra and corners with eight  $MO_4$  tetrahedra. In contrast, the rare-earth oxide sublattice in quadruple metalates consists of  $REO_8$  polyhedra, that are isolated from each other. Rare-earth and transition metal oxide sublattices are connected via corner-sharing of  $REO_8$  and  $MO_4$  polyhedra.

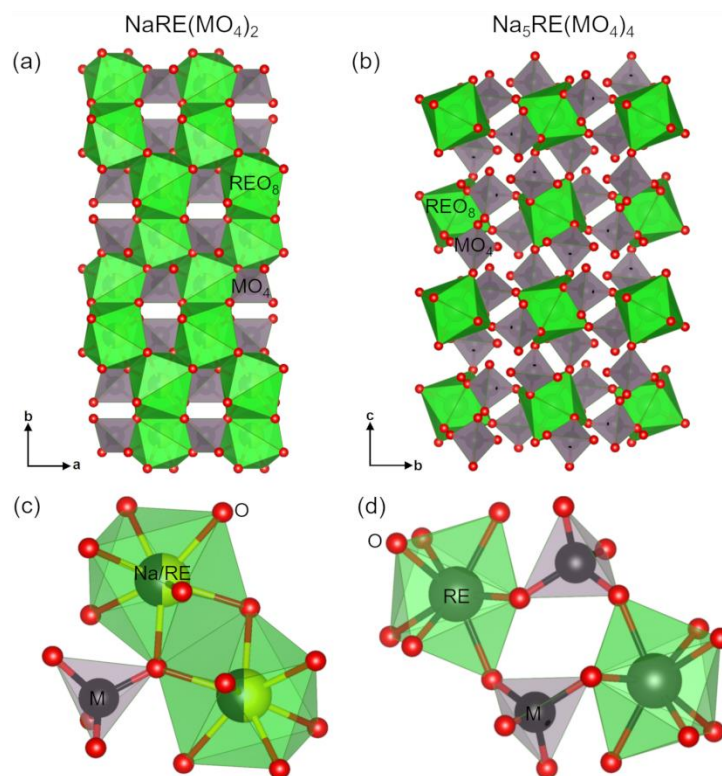


**Figure 1.3.** Connectivity of REO<sub>8</sub> and MO<sub>4</sub> polyhedra in (a) NaRE(MO<sub>4</sub>)<sub>2</sub> and (b) Na<sub>5</sub>RE(MO<sub>4</sub>)<sub>4</sub>. (c) REO<sub>8</sub> polyhedra in NaRE(MO<sub>4</sub>)<sub>2</sub> share edges and are connected through RE–O–RE bridges. These polyhedra share corners with MO<sub>4</sub> polyhedra forming RE–O–M bridges. (d) REO<sub>8</sub> polyhedra in Na<sub>5</sub>RE(MO<sub>4</sub>)<sub>4</sub> are isolated from each other and share corners with MO<sub>4</sub> polyhedra forming RE–O–M–O–RE bridges.

Upon changing the chemical composition of the host, the topology of the rare-earth and the transition metal oxide sublattices (i.e., the connectivity between the REO<sub>8</sub>–MO<sub>4</sub> and REO<sub>8</sub>–REO<sub>8</sub> polyhedra) changes. The composition-driven structural changes in the hosts are expected to have an impact on host-activator and activator-activator energy-transfer processes, which, ultimately, govern the thermometric response of the phosphors. Therefore, employing the above-mentioned scheelite-type and scheelite-related metalates as hosts for thermosensitive phosphors provides a starting point to systematically investigate how the chemical composition and the crystal structure affect the thermometric response of the thermosensitive phosphors.

### 1.3.2. Chemically Substituted $\text{Na}_x\text{La}(\text{MO}_4)_w$ as Thermosensitive Phosphors

Substitution of optically silent lanthanum ion in  $\text{Na}_x\text{La}(\text{MO}_4)_w$  with optically active rare-earths has been widely used as a strategy to develop luminescent materials.<sup>5-6, 46-47</sup> Lanthanum being a stoichiometric component of the hosts is expected to facilitate incorporation of rare-earth activators. Two strategies are used for chemical substitution. First, the substitution of lanthanum ion with a single rare-earth emitter such as  $\text{Dy}^{3+}$ ,  $\text{Eu}^{3+}$ , and  $\text{Ho}^{3+}$ . These rare-earth ions feature thermally coupled levels whose photoluminescence emission depends directly on temperature. However, single-emitter thermosensitive phosphors resulted from this strategy exhibit a decrease in their thermometric sensitivity with temperature due to thermal quenching of the photoluminescence emission. Very recently, a second strategy has been introduced; that is employing the photoluminescence emission from two emitter ions incorporated into a single host to mitigate the effect of thermal quenching of photoluminescence emission on thermometric sensitivity. To this end, dual-emitter thermosensitive phosphors coupling two rare-earth emitters with distinct thermal quenching characteristics or a rare-earth emitter with a transition metal (e.g.,  $\text{Cr}^{3+}$ ,  $\text{Mn}^{4+}$ ) have been investigated.<sup>24, 48</sup>

The objective of the work presented in this dissertation is to gain understanding of how to tailor the thermometric response of thermosensitive phosphors via rational manipulation of their chemical composition and crystal structure. Towards this goal, temperature-dependent luminescence response of single- and dual-emitter thermosensitive phosphors was investigated using two approaches. In the first approach, the dependence of the thermometric response of single-emitter thermosensitive phosphors on their composition and the crystals structure was investigated. The effect of the activator concentration and the hosts' composition on thermometric performance was evaluated. The focus was placed on employing the compositional tuning of

single-emitter thermosensitive phosphors to tailor their thermometric response. A series of  $\text{Dy}^{3+}$ -activated  $\text{NaLa}(\text{MO}_4)_2$  and  $\text{Na}_5\text{La}(\text{MO}_4)_4$  downconverting phosphors were investigated to this end. These phosphors were excited in the UV wavelengths, and their temperature-dependent photoluminescence emission was collected in the visible region. In the second approach, the thermometric response of dual-emitter thermosensitive phosphors was investigated. The experimental outcomes were discussed with an eye toward understanding how to enhance the synthetic control over the thermometric response of thermosensitive phosphors using pairs of luminescent emitters. Two types of dual-emitter phosphors were investigated: downconverting and upconverting thermosensitive phosphors. Within the scope of this dissertation, temperature-dependent luminescence response of dual-emitter downconverting phosphor,  $\text{Dy}^{3+}$  and  $\text{Pr}^{3+}$ -coactivated  $\text{NaLa}(\text{MoO}_4)_2$  was investigated in 100–600 K temperature range. Green and red photoluminescence emission bands from  $\text{Dy}^{3+}$  and  $\text{Pr}^{3+}$ , respectively, were employed to probe the temperature. However, employing downconverting thermosensitive phosphors for some practical applications are hindered owing to the absorption of UV light by the upper layers of the thermal barrier coating.<sup>20</sup> In contrast, the upconverting thermosensitive phosphors, which emit in the visible region under the excitation of near-infrared light (NIR) have the potential to overcome this problem. Therefore, temperature-dependent luminescence of two upconverting phosphors was investigated. Motivated by the studies on NIR-to-blue upconversion in stoichiometric  $\text{NaYb}(\text{MO}_4)_2$ ,<sup>49</sup>  $\text{Eu}^{3+}$ -activated  $\text{NaYb}(\text{MO}_4)_2$  dual-emitter thermosensitive phosphors were developed. Cooperative blue luminescence from  $\text{Yb}^{3+}$ – $\text{Yb}^{3+}$  dimers and the red emission from  $\text{Eu}^{3+}$  activator ions were employed to probe the temperature. Thermometric response of  $\text{Eu}^{3+}$ -activated  $\text{NaYb}(\text{MoO}_4)_2$  and  $\text{NaYb}(\text{WO}_4)_2$  was investigated in 100–500 K and 100–600 K temperature

range, respectively. The temperature-dependent color change of the photoluminescence emission in both dual-emitter downconverting and upconverting thermosensitive phosphors are highlighted.

#### 1.4. Dissertation Organization

This dissertation contains seven chapters. **Chapter 2** describes the material synthesis and characterization techniques used in the work presented, including formal definitions of the metrics used to assess thermometric performance. **Chapter 3** focuses on the synthesis, crystal structure, and thermometric performance of downconverting,  $\text{Dy}^{3+}$ -activated  $\text{A}_u\text{RE}_v(\text{MO}_4)_w$  single-emitter thermosensitive phosphors. **Chapter 4** describes the synthesis, crystal structure, and room temperature luminescence response of  $\text{NaYb}(\text{MoO}_4)_2$  and  $\text{NaYb}(\text{WO}_4)_2$  phosphors. **Chapter 5** is dedicated to studying the thermometric response of upconverting  $\text{Eu}^{3+}$ -activated  $\text{NaYb}(\text{MoO}_4)_2$  and  $\text{NaYb}(\text{WO}_4)_2$ . **Chapter 6** focuses on the synthesis and thermometric performance  $\text{Dy}^{3+}$  and  $\text{Pr}^{3+}$ -coactivated  $\text{NaLa}(\text{MoO}_4)_2$ . A summary of the research work presented throughout this dissertation is given in **Chapter 7** along with future research directions.

Each chapter is divided into four sections: **Introduction** provides a short review of already reported investigations related to the work presented in the chapter. **Experimental** describes the synthesis and characterization techniques used in the study. **Results and Discussion** focuses on the interpretation of experimental results and discusses the significance of the research findings related to the scientific problem being solved. Finally, **Conclusions and Perspectives** provides a summary of the work presented in the thesis and highlights the impact of the research findings on the area of research under investigation.



## CHAPTER 2. MATERIALS SYNTHESIS AND CHARACTERIZATION TECHNIQUES

This chapter describes the experimental and characterization techniques used for the work presented in this dissertation.

### 2.1. Materials

Throughout the thesis, a number of rare-earth-activated scheelite and scheelite-type group VI metal oxides were synthesized. All starting materials were purchased from commercial sources and used without further purification.

### 2.2. Experimental Techniques

#### 2.2.1. Synthesis

All the samples were synthesized using high temperature solid-state reactions. Conventional solid-state and microwave heating methods were employed.

##### 2.2.1.1. Conventional Solid-State Synthesis of $\text{NaLa}_{1-x}\text{RE}_x(\text{MoO}_4)_2$ .

$\text{Na}_2\text{CO}_3$  (99.5%),  $\text{La}_2\text{O}_3$  (99.9%),  $\text{MoO}_3$  (99.5%), and  $\text{RE}_2\text{O}_3$  (>99.5%) was used for the synthesis. All chemicals were purchased from Sigma-Aldrich and used as received. Stoichiometric amounts of starting materials were mixed with a small amount of acetone and ground in an agate mortar to make a homogeneous mixture. Powder mixtures were heated either in alumina crucibles ( $\sim 5 \text{ cm}^3$ ) or combustion boats ( $\sim 6 \text{ cm}^3$ ) under air. First, attempts were made to synthesize phase-pure  $\text{NaLa}(\text{MoO}_4)_2$ . Heating and cooling rates, reaction temperatures, and total heating times used for each trial are shown in **Table 2.1**. When the heating rate was faster than  $5^\circ\text{C}/\text{min}$ ,  $\text{MoO}_3$  was susceptible to sublimation, and  $\text{Na}_2\text{Mo}_2\text{O}_7$  was observed as the major phase. Further, at temperatures below  $800^\circ\text{C}$ , unreacted  $\text{MoO}_3$  and  $\text{Na}_2\text{MoO}_4$  were observed as impurity phases. The optimized synthesis conditions were employed to prepare  $\text{NaLa}_{1-x}\text{RE}_x(\text{MoO}_4)_2$  phosphors.

**Table 2.1.** Optimization of Synthesis Conditions for  $\text{NaLa}_{1-x}\text{RE}_x(\text{MoO}_4)_2$ 

Heating rate ( $^{\circ}\text{C min}^{-1}$ )	Cooling rate ( $^{\circ}\text{C min}^{-1}$ )	Reaction temperature ( $^{\circ}\text{C}$ )	Total reaction time (h)	Major phase	Impurity phase
10	10	600	18 (6+6+6)	$\text{Na}_2\text{Mo}_2\text{O}_7$	$\text{MoO}_3$
10	5	650	18 (6+6+6)	$\text{Na}_2\text{Mo}_2\text{O}_7$	$\text{MoO}_3$
5	5	650	18 (6+6+6)	$\text{NaLa}(\text{MoO}_4)_2$	$\text{Na}_2\text{Mo}_2\text{O}_7$ ,
5	5	700	18 (6+6+6)	$\text{NaLa}(\text{MoO}_4)_2$	$\text{Na}_2\text{MoO}_4$
5	5	750	18 (6+6+6)	$\text{NaLa}(\text{MoO}_4)_2$	$\text{Na}_2\text{MoO}_4$
5	5	800	18 (6+6+6)	$\text{NaLa}(\text{MoO}_4)_2$	None
5	5	800	12 (6+6)	$\text{NaLa}(\text{MoO}_4)_2$	None

**2.2.1.2. Conventional Solid-State Synthesis of  $\text{NaLa}_{1-x}\text{RE}_x(\text{WO}_4)_2$ .**

$\text{Na}_2\text{CO}_3$  (99.5%),  $\text{La}_2\text{O}_3$  (99.9%),  $\text{WO}_3$  (99.9%), and  $\text{RE}_2\text{O}_3$  (>99.5%) was used for the synthesis. Stoichiometric amounts of starting materials were mixed with a small amount of acetone and ground in an agate mortar to make a homogeneous mixture. Powder mixtures were heated either in alumina crucibles ( $\sim 5 \text{ cm}^3$ ) or combustion boats ( $\sim 6 \text{ cm}^3$ ) under air. First, attempts were made to synthesize phase-pure  $\text{NaLa}(\text{WO}_4)_2$ . Heating and cooling rates, reaction temperatures, and total heating times used for each trial are shown in **Table 2.2**. When the reaction temperature was below  $800 \text{ }^{\circ}\text{C}$ , unreacted  $\text{WO}_3$  was observed as an impurity phase. The optimized synthesis conditions were employed to prepare  $\text{NaLa}_{1-x}\text{RE}_x(\text{MoO}_4)_2$  phosphors.

**Table 2.2.** Optimization of Synthesis Conditions for  $\text{NaLa}_{1-x}\text{RE}_x(\text{WO}_4)_2$ 

Heating rate ( $^{\circ}\text{C min}^{-1}$ )	Cooling rate ( $^{\circ}\text{C min}^{-1}$ )	Reaction temperature ( $^{\circ}\text{C}$ )	Total reaction time (h)	Major phase	Impurity phase
5	5	800	12 (6+6)	$\text{NaLa}(\text{WO}_4)_2$	$\text{WO}_3$
5	5	850	12 (6+6)	$\text{NaLa}(\text{WO}_4)_2$	None

### 2.2.1.3. Conventional Solid-State Synthesis of $\text{Na}_5\text{La}_{1-x}\text{RE}_x(\text{MoO}_4)_4$ .

Preparation of  $\text{Na}_5\text{La}_{1-x}\text{RE}_x(\text{MoO}_4)_4$  was first attempted using  $\text{Na}_2\text{CO}_3$  (99.5%),  $\text{La}_2\text{O}_3$  (99.9%),  $\text{MoO}_3$  (99.9%), and  $\text{RE}_2\text{O}_3$  (>99.5%) as starting materials. Upon using  $\text{Na}_2\text{CO}_3$  as a starting material, it was impossible to avoid the formation of  $\text{Na}_2\text{MoO}_4$  impurity phase. As a solution,  $\text{Na}_2\text{MoO}_4$  was used as a starting material.  $\text{Na}_2\text{MoO}_4$  was prepared in house using conventional solid-state reactions.  $\text{Na}_2\text{CO}_3$  (99.5%), and  $\text{MoO}_3$  (99.5%) were used as starting materials. Stoichiometric amounts of the starting materials were mixed with a small volume of acetone and ground in an agate mortar for ~20 min. The unreacted homogeneous mixture was placed in an alumina crucible and heated at 600 °C under air for 6h. After an intermediate grinding, powder was reheated under identical conditions to obtain polycrystalline powders. As prepared  $\text{Na}_2\text{MoO}_4$  was used along with other starting materials to synthesize  $\text{Na}_5\text{La}_{1-x}\text{RE}_x(\text{MoO}_4)_4$ . Heating and cooling rates, reaction temperature, and reaction time was carefully controlled to avoid the formation of  $\text{NaRE}(\text{MoO}_4)_2$  impurity phase. (see **Table 3.1**)

### 2.2.1.4. Conventional Solid-State Synthesis of $\text{Na}_5\text{La}_{1-x}\text{RE}_x(\text{WO}_4)_4$ .

Preparation of  $\text{Na}_5\text{La}_{1-x}\text{RE}_x(\text{WO}_4)_4$  was first attempted using  $\text{Na}_2\text{CO}_3$  (99.5%),  $\text{La}_2\text{O}_3$  (99.9%),  $\text{WO}_3$  (99.9%), and  $\text{RE}_2\text{O}_3$  (>99.5%) as starting materials. Upon using  $\text{Na}_2\text{CO}_3$  as a starting material, it was impossible to avoid the formation of  $\text{Na}_2\text{WO}_4$  impurity phase. As a solution,  $\text{Na}_2\text{WO}_4$  was used as a starting material.  $\text{Na}_2\text{WO}_4$  was prepared in house using conventional solid-state reactions.  $\text{Na}_2\text{CO}_3$  (99.5%), and  $\text{MoO}_3$  (99.5%) were used as starting materials. Stoichiometric amounts of the starting materials were mixed with a small volume of acetone and ground in an agate mortar for ~20 min. The unreacted homogeneous mixtures were placed in alumina crucibles and heated at 600 °C under air for 12h. After an intermediate grinding, powder was reheated under identical conditions to obtain polycrystalline powders. As prepared

$\text{Na}_2\text{WO}_4$  was used along with other starting materials to synthesize  $\text{Na}_5\text{La}_{1-x}\text{RE}_x(\text{WO}_4)_4$ . Heating and cooling rates, reaction temperature, and reaction time was carefully controlled to avoid the formation of  $\text{NaRE}(\text{WO}_4)_2$  impurity phase. (see **Table 3.1**)

### 2.2.1.5. Microwave Heating.

Microwave heating method is an energy-efficient synthesis route to prepare rare-earth activated metalates. A new synthesis protocol was developed to prepare rare-earth activated  $\text{NaLa}(\text{MoO}_4)_2$ . Stoichiometric amounts of starting materials were mixed with a small amount of acetone and ground in an agate mortar to make a homogeneous powder mixture. The powder mixture was transferred into an alumina crucible and covered with an alumina plate to prevent contamination of the powder mixture. Next, as shown in **Figure 2.1**, the alumina crucible was partially immersed in a secondary porcelain crucible filled with activated charcoal granules. Activated charcoal serves as the susceptor<sup>50</sup>, which absorbs electromagnetic waves (microwave) and subsequently transfers the energy to alumina crucible containing the powder mixture. Crucibles were heated in a microwave oven operating at a frequency of 2450 MHz with 1200 W

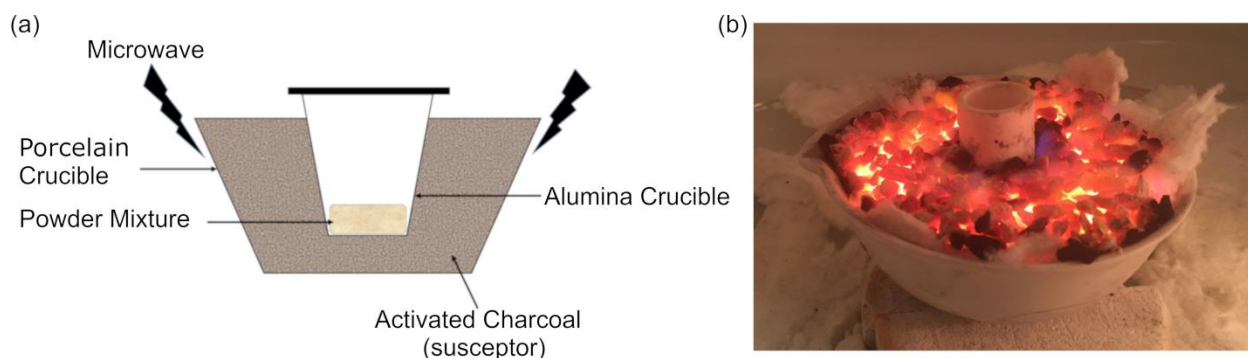


**Figure 2.1.** (a) Diagram of a typical reaction system employed to synthesize rare-earth activated  $\text{NaLa}(\text{MoO}_4)_2$  using microwave heating. (b) Digital picture of the reaction system immediately after heating in the microwave oven for 3 minutes at a power of 900 W.

maximum output power (Panasonic electronics). The reaction temperature and the total heating time was optimized to obtain the target product.

## **2.2.2. Materials Characterization**

### **2.2.2.1. Powder X-ray Diffraction**

Powder X-ray diffraction patterns of synthesized patterns were collected using a Bruker D2 Phaser diffractometer operated at 30 kV and 10 mA. Cu  $K\alpha$  radiation ( $\lambda = 1.5418 \text{ \AA}$ ) was employed. A nickel filter was utilized to remove Cu  $K\beta$ . Diffractograms were collected in the  $10\text{--}80^\circ 2\theta$  range. The step size and step time were adjusted to obtain a diffraction pattern with an adequate resolution (e.g., step size of  $0.0125^\circ$  and a step time of 1.25 s).

### **2.2.2.2. Synchrotron Powder X-ray Diffraction**

X-ray diffraction patterns were collected at the 11-BM of the Advanced Photon Source at the Argonne National Laboratory. The high flux and resolution of synchrotron radiation provide more structural information compare to a laboratory-based bench top diffractometer. Powder samples were packed in Kapton tubes and diffraction patterns were collected in the transmission mode. The incident photon energy of 29.936 keV ( $\lambda = 0.4141650 \text{ \AA}$ ) was used for the data collection. Appropriate step size and scan speed were employed to obtain a diffraction pattern with an adequate signal-to-noise ratio.

### **2.2.2.3 Rietveld Analysis**

This is a standard method of analyzing X-ray diffraction patterns of crystalline materials. Rietveld analysis of PXRD patterns was performed using the General Structure Analysis System (GSAS) with the graphical user interphase (EXPGUI) software. Crystal structures were refined using the appropriate space group. The parameters including scale factor, background, peak shape, lattice constants, isotropic displacement parameter for all atoms were refined. The occupancy of

each site was fixed according to the nominal composition of the crystal structure being refined. Residual  $R_{wp}$  values and visual inspection of the difference curves of the Rietveld fits were employed to assess the quality of the refined structural models.

#### **2.2.2.4. Inductively Coupled Plasma Mass Spectrometry (ICP–MS)**

ICP–MS is an analytical technique employed for elemental analysis. In the dissertation research, ICP–MS analyses were performed using a 7700 Series ICP–MS analyzer (Agilent Technologies). First, a series of standard solutions over the desired concentration range was prepared using commercially available single-element standards. Double deionized water (18.1 M $\Omega$ ) was used for dilution. Fifty milligrams of powder sample were digested in concentrated HCl at 60 °C to prepare the solution containing the analyte.

#### **2.2.2.5. Room-Temperature Spectrofluorometry**

Spectrofluorometric analyses were carried out using a Fluorolog 3–222 fluorometer (Horiba Scientific) featuring R928p and R2658p photomultiplier tubes. Two excitation sources were employed: Continuous wave Xe lamp (450 W) and A PSU-III-LED (Opto Engine, LLC) continuous-wave 973 nm laser (beam dimensions  $\sim 5 \times 8$  mm<sup>2</sup>). Spectra were recorded in the front-face geometry. Appropriate bandpass filters were employed when necessary.

#### **2.2.2.6. Variable Temperature Spectrofluorometry**

Temperature-dependent spectrofluorometric studies were performed using a VPF–800 variable-temperature stage (Janis Research Company, LLC). This stage was equipped with a custom-made sample holder consisting of a copper block with a 12 mm diameter by 0.8 mm deep sample cavity. Powder samples were held in place by a fluorescence-free UV grade fused silica window secured by a stainless-steel retainer and four spring-loaded screws. A Lake Shore 335–3060 controller (Lake Shore Cryotronics, Inc.) and a thermocouple directly connected to the

copper holder provided temperature readings with a  $\pm 0.2$  K accuracy. Once loaded in the variable-temperature stage, samples were degassed by heating at 700 K for 2 h under vacuum ( $<1$  mTorr). A heating rate of  $5 \text{ K min}^{-1}$  was employed. Samples were allowed to dwell for  $\sim 10$  minutes at the target temperature prior to data collection.

### 2.2.2.7. Luminescence Intensity Ratio

Temperature-dependent changes in the intensity of the emission bands,<sup>51</sup> lifetime of the excited emissive states,<sup>14</sup> and the relative shift of the emission bands<sup>52</sup> can be employed to probe the temperature of luminescent materials. Owing to the simplicity, quick response, and being independent of the measuring conditions have made the luminescence intensity ratio ( $R$ ) the most common method used for optical temperature sensing. This method is often employed for phosphors that have rare-earth emitters featuring thermally coupled levels. As shown in **Figure 2.2a**, in a rare-earth ion, the energy gap between two thermally coupled levels is  $\sim 200\text{--}2000 \text{ cm}^{-1}$ , and they are separated by at least  $3000 \text{ cm}^{-1}$  from the next lower-lying state.<sup>14, 20, 53</sup> Upon changing the temperature, the population of the upper ( $U$ ) and the lower ( $L$ ) thermally coupled levels change regularly, which changes the intensities of the emission bands corresponding to the transitions from thermally coupled levels to the ground state.

As given in equation (1.1), the luminescence intensity ratio is computed using the integrated intensities of the emission bands originate from the thermally coupled levels of the rare-earth emitter.

$$R(T) = \frac{I_U}{I_L} \quad (2.1)$$

Where  $R(T)$  is the luminescence intensity ratio.  $I_U$  and  $I_L$  are the integrated intensities of the emission bands corresponding to the transitions from the upper and the lower thermally coupled

levels to the ground state, respectively. Then, the experimental  $R(T)$  values are fit with a Boltzmann type distribution given by equation (1.2).

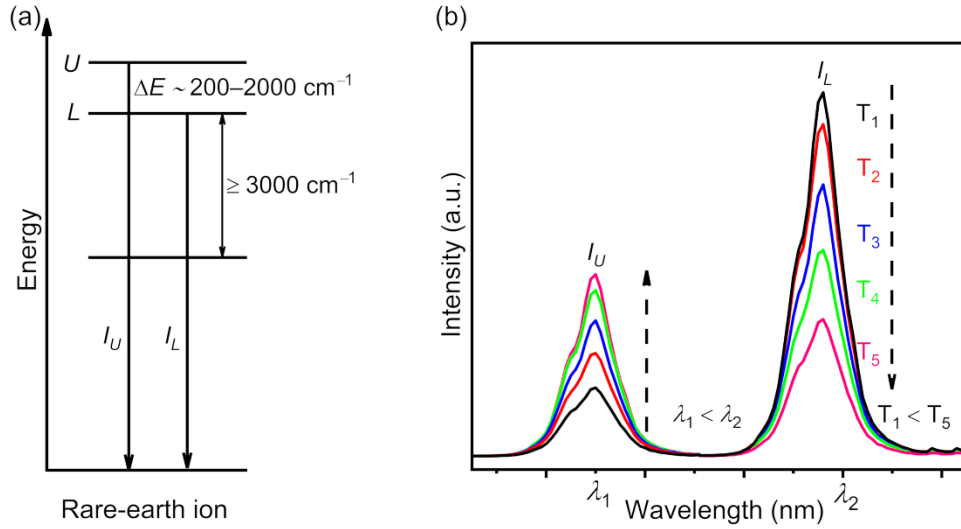


**Figure 2.3.** Energy level diagram of a rare-earth ion featuring thermally couple levels. (b) Temperature-dependent changes in the intensities of the photoluminescence emission bands corresponding to the transitions from thermally coupled levels to the ground state.

$$R = A \times \exp \left[ - \frac{\Delta E_{fit}}{k_B T} \right] + B \quad (2.2)$$

Here,  $\Delta E_{fit}$  is the energy gap between the thermally coupled levels.  $k_B$  is the Boltzmann constant.  $A$  and  $B$  are constants obtained from the fitting.  $B$  constant is added as an offset to account for the stray light originating from the energy levels other than the thermally coupled levels and the excitation source.<sup>51</sup> Four thermometric parameters are computed to assess the performance of characteristics: absolute sensitivity, relative sensitivity, repeatability, and temperature resolution. Absolute sensitivity ( $S_A$ ) is defined as a quotient of the change in luminescent intensity ratio as a function of temperature (equation 1.3.)

$$S_A = \frac{dR(T)}{dT} \quad (2.3)$$



Relative sensitivity (equation 1.4) allows the performance of thermosensitive phosphors to be compared.

$$S_R = \frac{1}{R(T)} \frac{dR(T)}{dT} \quad (2.4)$$

The precision of a series of measurements is given by the repeatability value. Repeatability measurement should be done under the same conditions: measurement procedure, measuring system, operating conditions, and operator.<sup>54</sup> The repeatability of a series of measurements can be calculated using equation (1.5).  $R_i(T)$  is the value of the luminescence intensity ratio in the  $i$ th cycle and  $\langle R(T) \rangle$  is the mean value of the ratio computed over  $n$  cycles.

$$\text{Repeatability (at } T) = 100 \times \left[ 1 - \frac{\max[R_i(T) - \langle R(T) \rangle]}{\langle R(T) \rangle} \right] \quad (2.5)$$

Temperature resolution is defined as the smallest change in temperature that causes a noticeable change in luminescence intensity ratio, and it is calculated using equation (1.6).

$$\Delta T \text{ (at } T) = \frac{\Delta R(T)}{S_A(T)} \quad (2.6)$$

where  $\Delta R(T)$  is the standard deviation of a series of  $R(T)$  values.  $S_A$  is the absolute temperature at temperature  $T$ .

## CHAPTER 3. DYSPROSIUM-ACTIVATED SCHEELITE-TYPE OXIDES AS THERMOSENSITIVE PHOSPHORS

*J. Mater. Chem. C*, 2019, 7601-7608

### 3.1. Introduction

Rare-earth-activated scheelite and scheelite-type phosphors are being actively developed as optical temperature sensors for physiological (298–323 K)<sup>55-56</sup> and intermediate (<1000 K) ranges.<sup>57-58</sup> These oxides of general formula  $A_xRE_y(MO_4)_z$  (A = alkali or alkaline-earth; RE = yttrium or rare-earth; M = Mo, W) offer unparalleled chemical and structural tunability. In principle, this enables compositional control of structural features relevant to temperature-dependent energy-transfer via chemical substitution, making scheelite and scheelite-type oxides an ideal platform to develop thermosensitive phosphors with tailored sensitivity. Double and quadruple molybdates and tungstates of formulas  $NaRE(MO_4)_2$  and  $Na_5RE(MO_4)_4$ , respectively, constitute archetypical examples of this structural diversity. Their crystal structures are shown in **Figures 1.1a** and **1.1b** and depict tetragonal unit cells featuring  $REO_8$  dodecahedra and  $MO_4$  tetrahedra as building blocks.<sup>56, 59</sup> In both oxides,  $MO_4$  tetrahedra are isolated from each other. By contrast, the connectivity of  $REO_8$  polyhedra drastically changes upon going from  $NaRE(MO_4)_2$  to  $Na_5RE(MO_4)_4$ . As discussed in **Chapter 1**, in  $NaRE(MO_4)_2$ , each  $REO_8$  polyhedra is connected to four neighboring polyhedra via edge-sharing, giving rise to RE–O–RE bridges that extend along axes *a*, *b*, and *c*. Additionally, each  $MO_4$  tetrahedron connects eight  $REO_8$  polyhedra via RE–O–M–O–RE bridges. In  $Na_5RE(MO_4)_4$ , on the other hand,  $REO_8$  polyhedra are isolated from each other and only RE–O–M–O–RE bridges are present; those bridges connect each  $MO_4$  tetrahedron to two  $REO_8$  polyhedra. One may hypothesize that compositional control of the dimensionality of the rare-earth sublattice, rare-earth–rare-earth distance, and  $REO_8$ – $MO_4$  connectivity serves as a lever to tailor the thermometric sensitivity of scheelite-type phosphors.

Although rare-earth activated scheelites are being pursued as down- and upconverting thermosensitive phosphors, no systematic investigations aimed at identifying compositions and structural motifs that maximize thermometric sensitivity have been reported. In addition, the vast majority of the reports on the thermometric performance of rare-earth-activated scheelites focuses on activators such as  $\text{Nd}^{3+}$ ,<sup>60</sup>  $\text{Eu}^{3+}$ ,  $\text{Eu}^{3+}$ ,<sup>30, 57</sup>  $\text{Yb}^{3+}$ - $\text{Nd}^{3+}$ ,<sup>58</sup>  $\text{Yb}^{3+}$ - $\text{Er}^{3+}$ ,<sup>61</sup> and  $\text{Yb}^{3+}$ - $\text{Ho}^{3+}$ .<sup>58, 62</sup> With the exception of a study on  $\text{Eu}^{3+}$ - $\text{Dy}^{3+}$  codoped  $\text{SrWO}_4$ ,<sup>55</sup> no reports exist on the performance of  $\text{Dy}^{3+}$ -activated scheelite and scheelite-type oxides, despite the importance of  $\text{Dy}^{3+}$  in phosphor

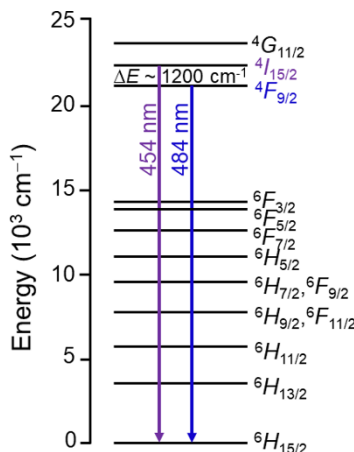


**Figure 3.1.** Dieke diagram of  $\text{Dy}^{3+}$  depicting blue emission from the thermally coupled levels  $^4I_{15/2}$  and  $^4F_{9/2}$ .

thermometry. As shown in **Figure 3.1**,  $\text{Dy}^{3+}$  ( $4f^9$ ) features a pair of levels whose emissions at 454 nm ( $^4I_{15/2} \rightarrow ^6H_{15/2}$ ) and 484 nm ( $^4F_{9/2} \rightarrow ^6H_{15/2}$ ) are thermally coupled. This coupling imparts thermometric functionality to  $\text{Dy}^{3+}$ -activated materials and has proven particularly useful in intermediate (<1000 K) and high-temperature (1000–1800 K) ranges.<sup>14, 20</sup> With the aim of bridging the abovementioned knowledge gaps, we report a systematic investigation of the thermometric performance of  $\text{Dy}^{3+}$ -activated double and quadruple molybdates and tungstates. Four series of scheelite-type oxides of formulas  $\text{NaLa}_{1-x}\text{Dy}_x(\text{MO}_4)_2$  and  $\text{Na}_5\text{La}_{1-x}\text{Dy}_x(\text{MO}_4)_4$  were synthesized in the solid-state. Their thermometric responses under steady-state ultraviolet excitation were

quantitatively interrogated between 300 and 700 K using the luminescence intensity ratio approach. Thermometric sensitivities were mapped as a function of the host's composition and activator concentration. Results from this analysis are discussed from the perspective of employing compositional tuning of Dy<sup>3+</sup>-activated scheelite-type phosphors to tailor their thermometric response. Finally, the sensitivities of NaLa<sub>1-x</sub>Dy<sub>x</sub>(MO<sub>4</sub>)<sub>2</sub> and Na<sub>5</sub>La<sub>1-x</sub>Dy<sub>x</sub>(MO<sub>4</sub>)<sub>4</sub> at 350 and 700 K are compared to those of other thermosensitive phosphors, including vanadates, niobates, aluminates, silicates, titanates, and zirconates typically used for intermediate- and high-temperature thermometry.

## 3.2. Experimental

### 3.2.1. Solid-State Synthesis

Conventional high-temperature solid-state reactions were employed to synthesize polycrystalline NaLa<sub>1-x</sub>Dy<sub>x</sub>(MO<sub>4</sub>)<sub>2</sub> and Na<sub>5</sub>La<sub>1-x</sub>Dy<sub>x</sub>(MO<sub>4</sub>)<sub>4</sub> (M = Mo, W;  $x = 0.000, 0.025, 0.050, 0.100, 0.500, 1.000$ ).

#### 3.2.1.2. Synthesis of NaLa<sub>1-x</sub>Dy<sub>x</sub>(MO<sub>4</sub>)<sub>2</sub> and Na<sub>5</sub>La<sub>1-x</sub>Dy<sub>x</sub>(MO<sub>4</sub>)<sub>4</sub> (M = Mo, W)

Series of NaLa<sub>1-x</sub>Dy<sub>x</sub>(MO<sub>4</sub>)<sub>2</sub> and NaLa<sub>1-x</sub>Dy<sub>x</sub>(MO<sub>4</sub>)<sub>4</sub> phosphors were synthesized according to protocol reported in **Chapter 2**. (see **sections 2.2.1.1–2.2.1.4**). Heating and cooling rates and reaction temperatures and times employed to synthesize NaLa<sub>1-x</sub>Dy<sub>x</sub>(MO<sub>4</sub>)<sub>2</sub> and NaLa<sub>1-x</sub>Dy<sub>x</sub>(MO<sub>4</sub>)<sub>4</sub> phosphors are given in **Table 3.1**. Polycrystalline samples were subjected to intermediate grindings to ensure the phase-purity of the final products.

### 3.2.2. Powder X-ray Diffraction (PXRD)

PXRD patterns were collected using a Bruker D2 Phaser diffractometer operated at 30 kV and 10 mA. Cu K $\alpha$  radiation ( $\lambda = 1.5418 \text{ \AA}$ ) was employed. A nickel filter was utilized to remove

Cu  $K\beta$  radiation. Diffractograms were collected in the  $10\text{--}80^\circ 2\theta$  range using a step size of  $0.025^\circ$  and a step time of 1.0 s. Diffraction patterns were recorded at room temperature.

**Table 3.1.** Synthesis Conditions for  $\text{NaLa}_{1-x}\text{Dy}_x(\text{MO}_4)_2$  and  $\text{Na}_5\text{La}_{1-x}\text{Dy}_x(\text{MO}_4)_4$

$x$	$\text{NaLa}_{1-x}\text{Dy}_x(\text{MO}_4)_2$						$\text{Na}_5\text{La}_{1-x}\text{Dy}_x(\text{MO}_4)_4$					
	Heating Rate ( $^\circ\text{C min}^{-1}$ )		Temperature ( $^\circ\text{C}$ )		Total Time (h)		Heating Rate ( $^\circ\text{C min}^{-1}$ )		Temperature ( $^\circ\text{C}$ )		Total Time (h)	
	Mo	W	Mo	W	Mo	W	Mo	W	Mo	W	Mo	W
0.000	5	5	800	850	12	12	5	3	600	650	30	8
0.025	5	5	800	850	12	12	5	3	600	625	42	18
0.050	5	5	800	850	12	12	5	3	600	600	12	96
0.100	5	5	800	850	12	12	5	3	600	600	12	20
0.500	5	5	800	850	12	12	5	3	600	625	30	18
1.000	5	5	800	850	12	12	5	3	600	625	30	24

### 3.2.3. Rietveld Analysis

Crystal structures were refined using the tetragonal space group  $I4_1/a$ . The following parameters were refined: (1) scale factor, (2) background, which was modeled using a shifted Chebyshev polynomial function, (3) peak shape, which was modeled using a modified Thompson–Cox–Hasting pseudo-Voigt function,<sup>63</sup> (4) lattice constants ( $a$  and  $c$ ), and (5) an isotropic displacement parameter for all metal atoms in the structure ( $U_{\text{iso}}^M$ ). The isotropic displacement parameter for all oxygen atoms ( $U_{\text{iso}}^O$ ) was constrained according to  $U_{\text{iso}}^O = 1.5 \times U_{\text{iso}}^M$ . For  $\text{NaLa}_{1-x}\text{Dy}_x(\text{MO}_4)_2$ , the occupancy of the rare-earth-containing  $4b$  site was fixed according to the nominal Na:La:Dy molar ratio of  $0.5:[0.5 \times (1 - x)]:[0.5 \times x]$ . In the case of  $\text{Na}_5\text{La}_{1-x}\text{Dy}_x(\text{MO}_4)_4$ , the occupancy of the rare-earth-containing  $4a$  site was fixed according to the nominal La:Dy molar ratio of  $(1 - x):x$ . Residual  $R_{\text{wp}}$  values and visual inspection of the difference curves of the Rietveld fits were employed to assess the quality of the refined structural models.

### 3.2.4. Variable-Temperature Spectrofluorometry

Spectrofluorometric analyses were carried out using a Fluorolog 3–222 fluorometer (Horiba Scientific) featuring a continuous wave Xe lamp (450 W). Temperature-dependent steady-state luminescence spectra were collected using a VPF–800 variable-temperature stage (Janis Research Company). Once loaded in the variable-temperature stage, samples were degassed by heating at 700 K (427 °C) for 2 h under vacuum (<1 mTorr). Emission spectra were collected in the 300–700 K temperature range at 50 K intervals. A heating rate of 5 K min<sup>-1</sup> was employed. Samples were allowed to dwell for ~10 min at the target temperature prior to data collection.

### 3.3. Results and Discussion

Rietveld analyses of PXRD data were performed to probe the phase-purity of the phosphors. Rietveld fits of the NaLa<sub>1-x</sub>Dy<sub>x</sub>(MO<sub>4</sub>)<sub>2</sub> and Na<sub>5</sub>La<sub>1-x</sub>Dy<sub>x</sub>(MO<sub>4</sub>)<sub>4</sub> tetragonal structures to the experimental PXRD patterns are shown in **Figures 3.4–3.5**. Plots of the unit cell constants and volume as a function of the Dy<sup>3+</sup> concentration are shown in **Figures 3.6**; numerical values are provided in the **Tables 3.2**. All the diffraction maxima are indexed to the corresponding scheelite-type phase, confirming the phase-purity of the phosphors. In the case of NaLa<sub>1-x</sub>Dy<sub>x</sub>(MO<sub>4</sub>)<sub>2</sub>, no secondary crystalline phases appear to be present. Obtaining phase-pure Na<sub>5</sub>La<sub>1-x</sub>Dy<sub>x</sub>(MO<sub>4</sub>)<sub>4</sub>, by contrast, was significantly more challenging due to the well-known tendency of NaLa<sub>1-x</sub>Dy<sub>x</sub>(MO<sub>4</sub>)<sub>2</sub> to form as a secondary phase.<sup>64</sup> Although this was avoided by carefully controlling reaction temperature and time, in some cases it came at the expense of having a small fraction of unreacted Na<sub>2</sub>MoO<sub>4</sub> or Na<sub>2</sub>WO<sub>4</sub> (<1 wt. %) in the final product. Very weak diffraction maxima corresponding to this ternary phase are observed in the PXRD patterns of Na<sub>5</sub>La<sub>0.9</sub>Dy<sub>0.1</sub>(MoO<sub>4</sub>)<sub>4</sub>, Na<sub>5</sub>Dy(MoO<sub>4</sub>)<sub>4</sub>, Na<sub>5</sub>La<sub>0.975</sub>Dy<sub>0.025</sub>(WO<sub>4</sub>)<sub>4</sub>, Na<sub>5</sub>La<sub>0.9</sub>Dy<sub>0.1</sub>(WO<sub>4</sub>)<sub>4</sub>, and Na<sub>5</sub>Dy(WO<sub>4</sub>)<sub>4</sub>. Lattice constants and unit cell volume show a linear contraction upon increasing

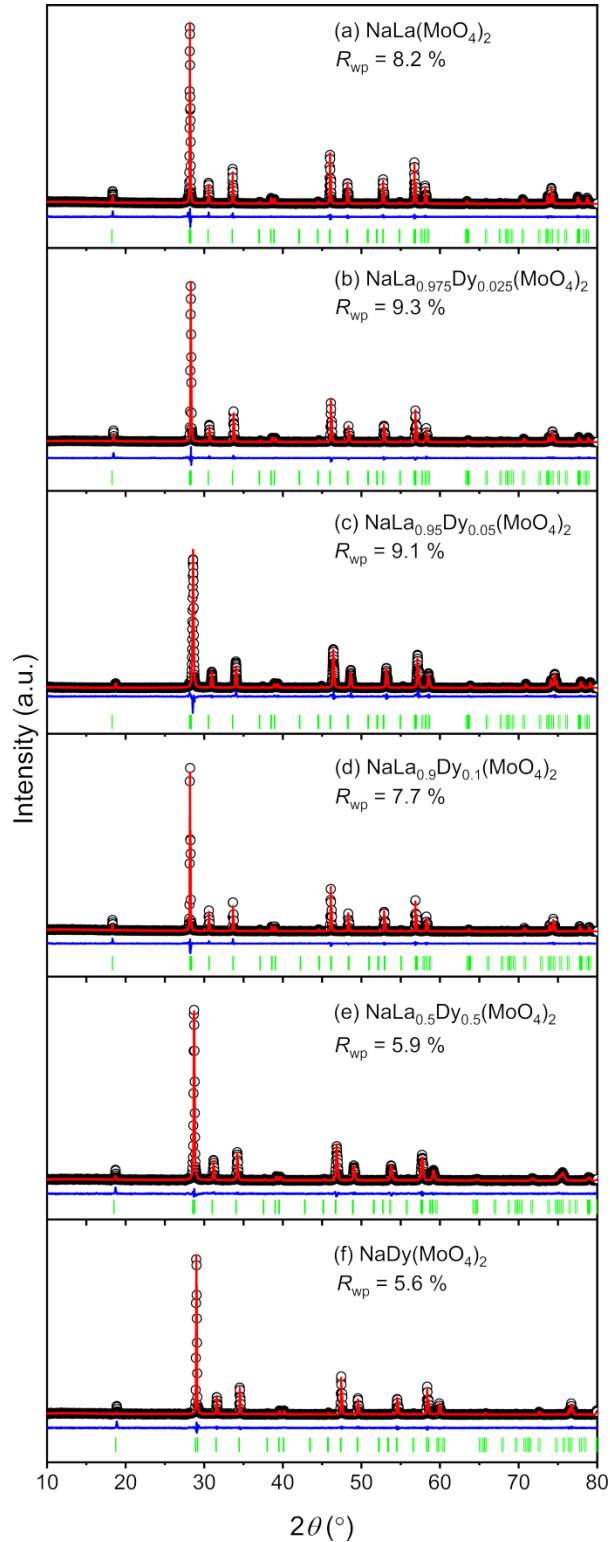


**Figure 3.2.** Rietveld analysis of the  $\text{NaLa}_{1-x}\text{Dy}_x(\text{MoO}_4)_2$  series. Experimental ( $\circ$ ) and calculated patterns ( $\rightarrow$ ) are shown along with difference curves ( $\leftarrow$ ). Tick marks ( $\updownarrow$ ) correspond to the calculated position of the diffraction maxima.

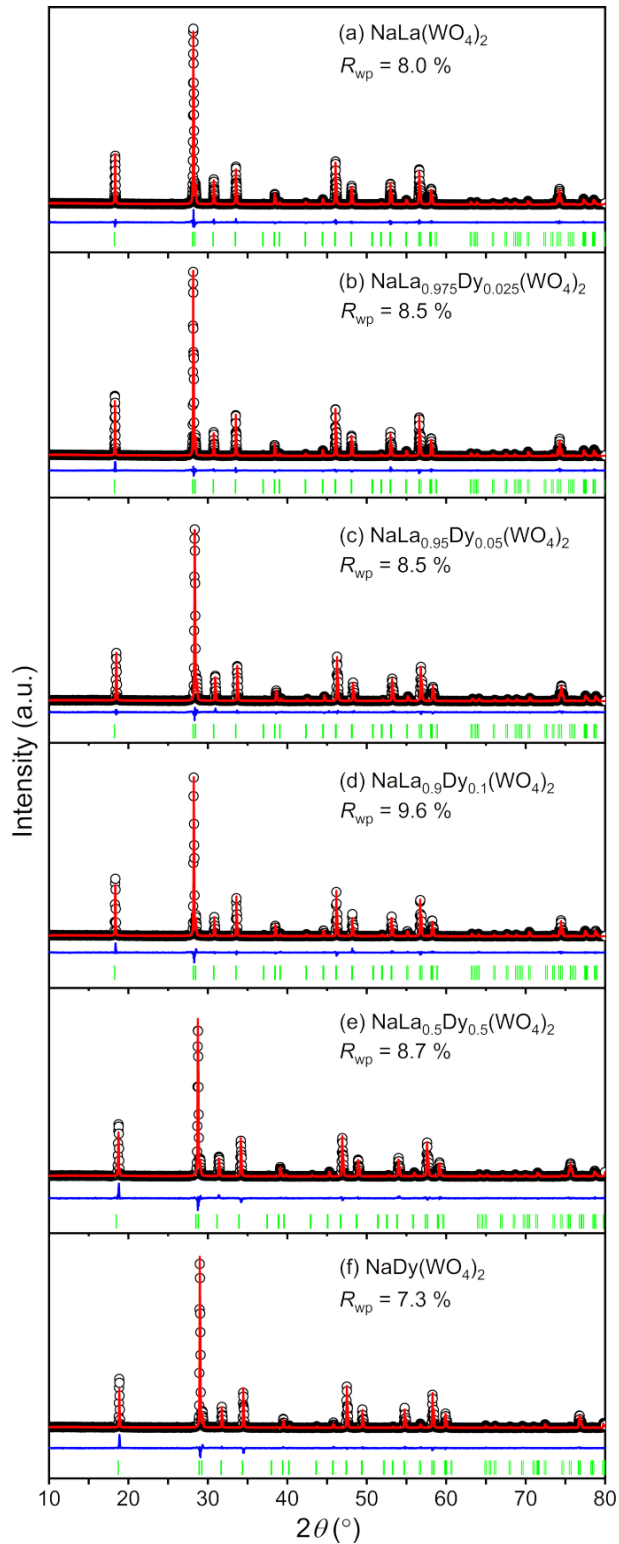


**Figure 3.3.** Rietveld analysis of the  $\text{NaLa}_{1-x}\text{Dy}_x(\text{WO}_4)_2$  series. Experimental (O) and calculated patterns (—) are shown along with difference curves (—). Tick marks (|) correspond to the calculated position of the diffraction maxima.



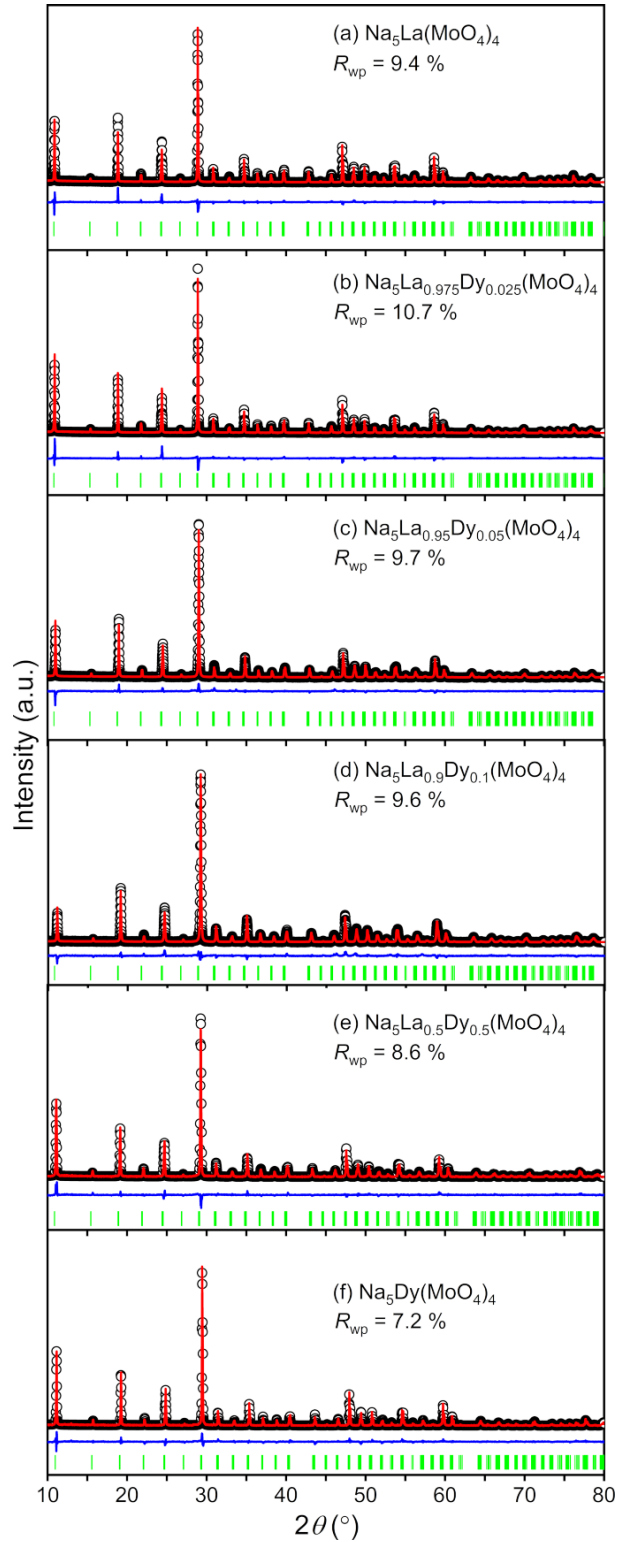


**Figure 3.4.** Rietveld analysis of the  $\text{Na}_5\text{La}_{1-x}\text{Dy}_x(\text{MoO}_4)_4$  series. Experimental ( $\circ$ ) and calculated patterns ( $\text{—}$ ) are shown along with difference curves ( $\text{—}$ ). Tick marks ( $\text{||}$ ) correspond to the calculated position of the diffraction maxima.

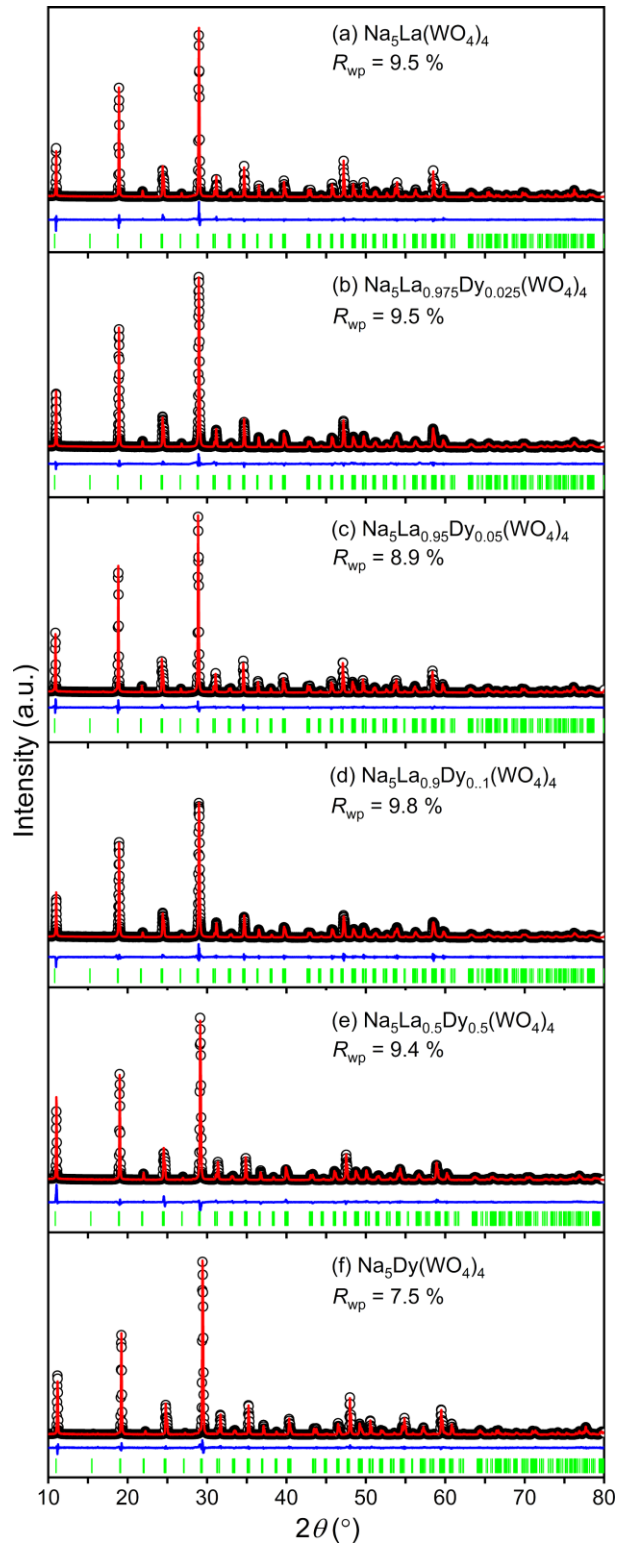


**Figure 3.5.** Rietveld analysis of the  $\text{Na}_5\text{La}_{1-x}\text{Dy}_x(\text{WO}_4)_4$  series. Experimental (O) and calculated patterns (—) are shown along with difference curves (—). Tick marks (|) correspond to the calculated position of the diffraction maxima.

**Table 3.2.** Structural Parameters of  $\text{NaLa}_{1-x}\text{Dy}_x(\text{MO}_4)_2$  and  $\text{Na}_5\text{La}_{1-x}\text{Dy}_x(\text{MO}_4)_4$ 

$\text{NaLa}_{1-x}\text{Dy}_x(\text{MoO}_4)_2$						
$x$	0.000	0.025	0.050	0.100	0.500	1.000
$a$ (Å)	5.34288(3)	5.33595(8)	5.33595(7)	5.32531(5)	5.26918(13)	5.21057(8)
$c$ (Å)	11.73410(9)	11.716208(19)	11.7161(2)	11.68853(13)	11.5370(4)	11.3629(2)
$V$ (Å <sup>3</sup> )	334.967(5)	334.097(11)	333.586(11)	331.474(7)	320.32(2)	308.504(12)
$U_{\text{iso}}^M$ (×100)	0.59(3)	1.67(5)	0.32(2)	1.11(5)	1.50(5)	1.44(6)
$U_{\text{iso}}^O$ (×100)	0.91(5)	2.57(8)	1.40(18)	1.66(7)	2.18(8)	2.19(8)
$R_{\text{wp}}$ (%)	8.2	9.3	9.1	7.7	5.9	5.6
$\text{NaLa}_{1-x}\text{Dy}_x(\text{WO}_4)_2$						
$x$	0.000	0.025	0.050	0.100	0.500	1.000
$a$ (Å)	5.35889(3)	5.35603(3)	5.35024(6)	5.34655(5)	5.28785(8)	5.22030(5)
$c$ (Å)	11.66772(9)	11.65948(8)	11.64224(16)	11.63262(14)	11.4875(2)	11.30518(16)
$V$ (Å <sup>3</sup> )	335.070(5)	334.476(4)	333.260(9)	332.525(8)	321.206(13)	308.084(9)
$U_{\text{iso}}^M$ (×100)	1.16(2)	1.13(3)	0.96(4)	0.94(4)	1.19(5)	1.99(5)
$U_{\text{iso}}^O$ (×100)	1.96(4)	1.52(4)	1.48(5)	1.44(6)	1.79(7)	2.89(7)
$R_{\text{wp}}$ (%)	8.0	8.5	8.5	9.6	8.7	7.3
$\text{Na}_5\text{La}_{1-x}\text{Dy}_x(\text{MoO}_4)_4$						
$x$	0.000	0.025	0.050	0.100	0.500	1.000
$a$ (Å)	11.57360(7)	11.57087(8)	11.56736(13)	11.56353(11)	11.48289(19)	11.38693(12)
$c$ (Å)	11.61945(9)	11.61605(12)	11.6153 (2)	11.6116(2)	11.5374(3)	11.43292(19)
$V$ (Å <sup>3</sup> )	1556.41(2)	1555.22(3)	1554.17(5)	1552.65(3)	1521.29(6)	1482.42(4)
$U_{\text{iso}}^M$ (×100)	0.20(3)	1.56(4)	0.55(4)	0.02(4)	1.81(6)	0.76(6)
$U_{\text{iso}}^O$ (×100)	0.30(5)	2.34(6)	0.82(6)	0.02(7)	2.61(9)	1.14(9)
$R_{\text{wp}}$ (%)	9.4	10.7	9.7	9.6	8.6	7.2
$\text{Na}_5\text{La}_{1-x}\text{Dy}_x(\text{WO}_4)_4$						
$x$	0.000	0.025	0.050	0.100	0.500	1.000
$a$ (Å)	11.62533(10)	11.62572(13)	11.62837(12)	11.62419(16)	11.54432(21)	11.44550(13)
$c$ (Å)	11.53952(14)	11.54320(18)	11.54188(17)	11.5362(2)	11.4530(3)	11.35432(18)
$V$ (Å <sup>3</sup> )	1559.55(4)	1560.15(5)	1560.68(4)	1558.79(6)	1526.35(7)	1487.41(4)
$U_{\text{iso}}^M$ (×100)	0.77(4)	1.22(3)	1.22(4)	0.76(3)	1.93(5)	1.03(4)
$U_{\text{iso}}^O$ (×100)	1.16(6)	1.64(5)	1.88(6)	1.14(5)	2.76(8)	1.49(6)
$R_{\text{wp}}$ (%)	9.5	9.5	8.9	9.8	9.4	7.5

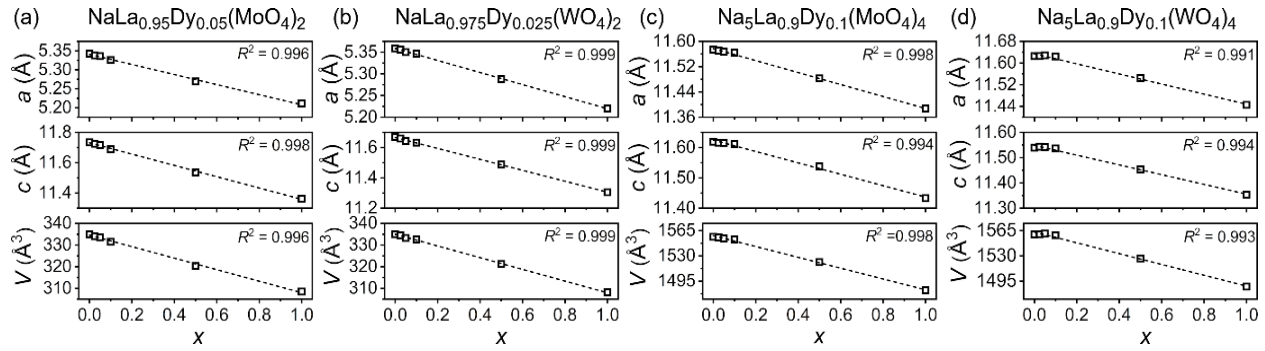


**Figure 3.6.** Unit cell constants and volume (a, c, and V) as a function of the Dy<sup>3+</sup> concentration are plotted for (e) NaLa<sub>1-x</sub>Dy<sub>x</sub>(MoO<sub>4</sub>)<sub>2</sub>, (f) NaLa<sub>1-x</sub>Dy<sub>x</sub>(WO<sub>4</sub>)<sub>2</sub>, (g) Na<sub>5</sub>La<sub>1-x</sub>Dy<sub>x</sub>(MoO<sub>4</sub>)<sub>4</sub>, and (h) Na<sub>5</sub>La<sub>1-x</sub>Dy<sub>x</sub>(WO<sub>4</sub>)<sub>4</sub>. Linear fits are depicted as dashed lines; the corresponding R<sup>2</sup> residuals are given.

the Dy<sup>3+</sup> concentration, as expected from ionic radius considerations (Dy<sup>3+</sup>: 1.083 Å, La<sup>3+</sup>: 1.216 Å).<sup>65</sup> The Na<sub>5</sub>La<sub>1-x</sub>Dy<sub>x</sub>(WO<sub>4</sub>)<sub>4</sub> series is the only exception to this trend. In this series, the unit cell volume is nearly constant between  $x = 0$  and 0.05. The temperature-dependent luminescence response of Dy<sup>3+</sup>-activated molybdates and tungstates was investigated using steady-state spectrofluorometry. Representative excitation and emission spectra collected between 300 and 700 K temperature range are given in **Figures 3.7a–d** for Na<sub>5</sub>La<sub>0.95</sub>Dy<sub>0.05</sub>(MoO<sub>4</sub>)<sub>2</sub>, Na<sub>5</sub>La<sub>0.975</sub>Dy<sub>0.025</sub>(WO<sub>4</sub>)<sub>2</sub>, Na<sub>5</sub>La<sub>0.9</sub>Dy<sub>0.1</sub>(MoO<sub>4</sub>)<sub>4</sub>, and Na<sub>5</sub>La<sub>0.9</sub>Dy<sub>0.1</sub>(WO<sub>4</sub>)<sub>4</sub>. At room temperature, these compositions display the highest emission intensity for the band at 484 nm, which is of central importance in our study (see insets in **Figures 3.7a–d**). Spectra corresponding to other compositions are given in the **Figures 3.8–3.11**. Excitation spectra were collected at 574 nm (<sup>4</sup>F<sub>9/2</sub> → <sup>6</sup>H<sub>13/2</sub>) because signal-to-noise ratios were significantly better than for spectra collected at 454 (<sup>4</sup>I<sub>15/2</sub> → <sup>6</sup>H<sub>15/2</sub>) or 484 nm (<sup>4</sup>F<sub>9/2</sub> → <sup>6</sup>H<sub>15/2</sub>). Excitation spectra consist of a broad band arising from an oxygen-to-metal p-to-d charge-transfer and a series of narrow bands resulting from intraconfigurational *f-f* transitions of Dy<sup>3+</sup>. The charge-transfer band maximum shifts to shorter wavelengths upon going from molybdates to tungstates. This blueshift (ca. 30 to 40 nm) reflects the higher energy of the excited state in the tungstates. Bands corresponding to the most intense

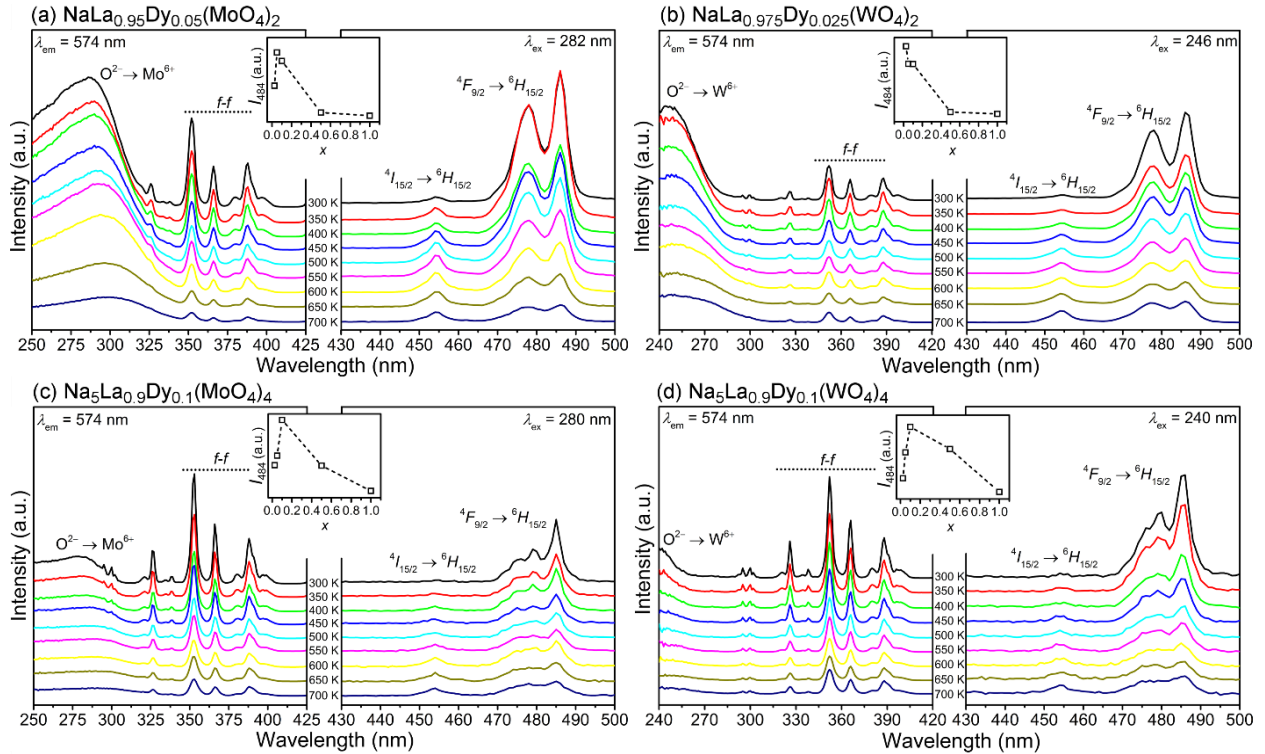


**Figure 3.7.** Temperature-dependent excitation and emission spectra of (a)  $\text{NaLa}_{0.95}\text{Dy}_{0.05}(\text{MoO}_4)_2$ , (b)  $\text{NaLa}_{0.975}\text{Dy}_{0.025}(\text{WO}_4)_2$ , (c)  $\text{Na}_5\text{La}_{0.9}\text{Dy}_{0.1}(\text{MoO}_4)_4$ , and (d)  $\text{Na}_5\text{La}_{0.9}\text{Dy}_{0.1}(\text{WO}_4)_4$ . Blue emission bands centered at 454 and 484 nm arise from the relaxation of the  ${}^4I_{15/2}$  and  ${}^4F_{9/2}$  thermally coupled levels of  $\text{Dy}^{3+}$ . Plots shown in the insets correspond to the room-temperature integrated intensity of the emission band at 484 nm as a function of the  $\text{Dy}^{3+}$  concentration; dashed lines are guides-to-the-eye.

$f-f$  transitions of  $\text{Dy}^{3+}$  are located at 328 ( ${}^6H_{15/2} \rightarrow {}^4F_{5/2}$ ), 353 ( ${}^6H_{15/2} \rightarrow {}^4I_{11/2}$ ,  ${}^6P_{7/2}$ ), 366 ( ${}^6H_{15/2} \rightarrow {}^6P_{5/2}$ ), and 388 nm ( ${}^6H_{15/2} \rightarrow {}^4I_{13/2}$ ,  ${}^4F_{7/2}$ ). We note that multiple assignments are possible because of the rich level structure of the  $4f^9$  energy manifold.<sup>66-67</sup> Excitation bands corresponding to  $f-f$  transitions are weaker than the charge-transfer band in  $\text{NaLa}_{1-x}\text{Dy}_x(\text{MO}_4)_2$  and stronger in  $\text{Na}_5\text{La}_{1-x}\text{Dy}_x(\text{MO}_4)_4$ , indicating that host-to-activator energy-transfer is more efficient in the former. Emission spectra were collected upon excitation of the host's charge-transfer and subsequent energy-transfer to the  $\text{Dy}^{3+}$  activator. All the phosphors exhibited yellow-green emission visible to the naked eye resulting from the  ${}^4F_{9/2} \rightarrow {}^6H_{13/2}$  transition (574 nm). For this study, however, it is blue emission bands located at 454 and 484 nm that are relevant. These

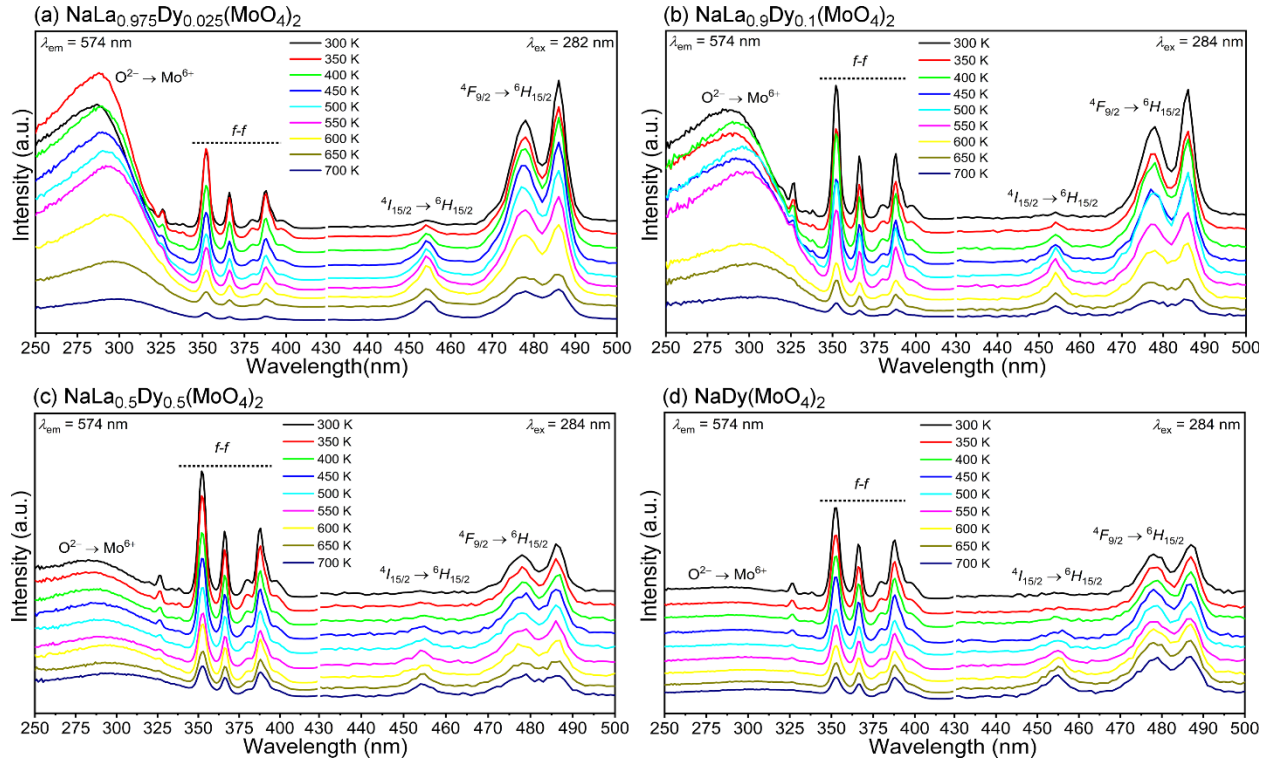


**Figure 3.8.** Temperature-dependent excitation and emission spectra of the  $\text{NaLa}_{1-x}\text{Dy}_x(\text{MoO}_4)_2$  series in the 300–700 K temperature range.

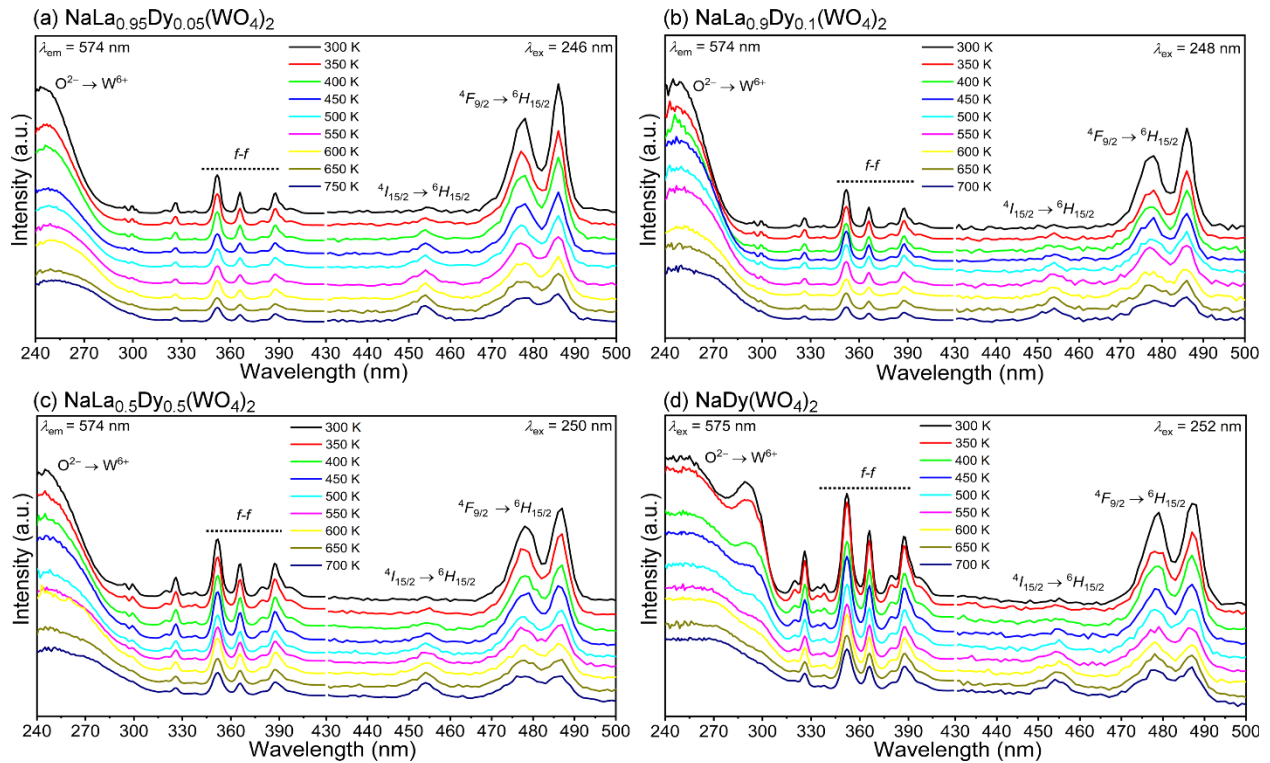


**Figure 3.9.** Temperature-dependent excitation and emission spectra of the  $\text{NaLa}_{1-x}\text{Dy}_x(\text{WO}_4)_2$  series in the 300–700 K temperature range.

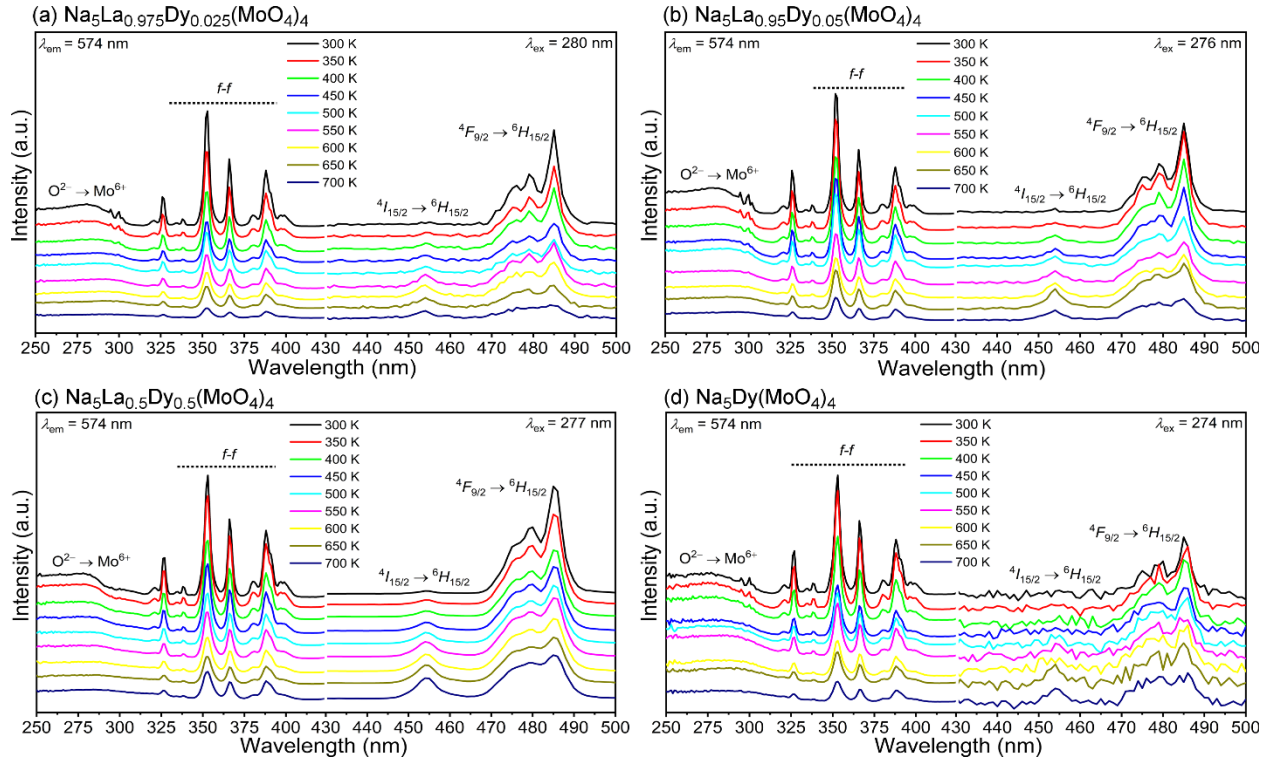


**Figure 3.11.** Temperature-dependent excitation and emission spectra of the  $\text{Na}_5\text{La}_{1-x}\text{Dy}_x(\text{MoO}_4)_4$  series in the 300–700 K temperature range.

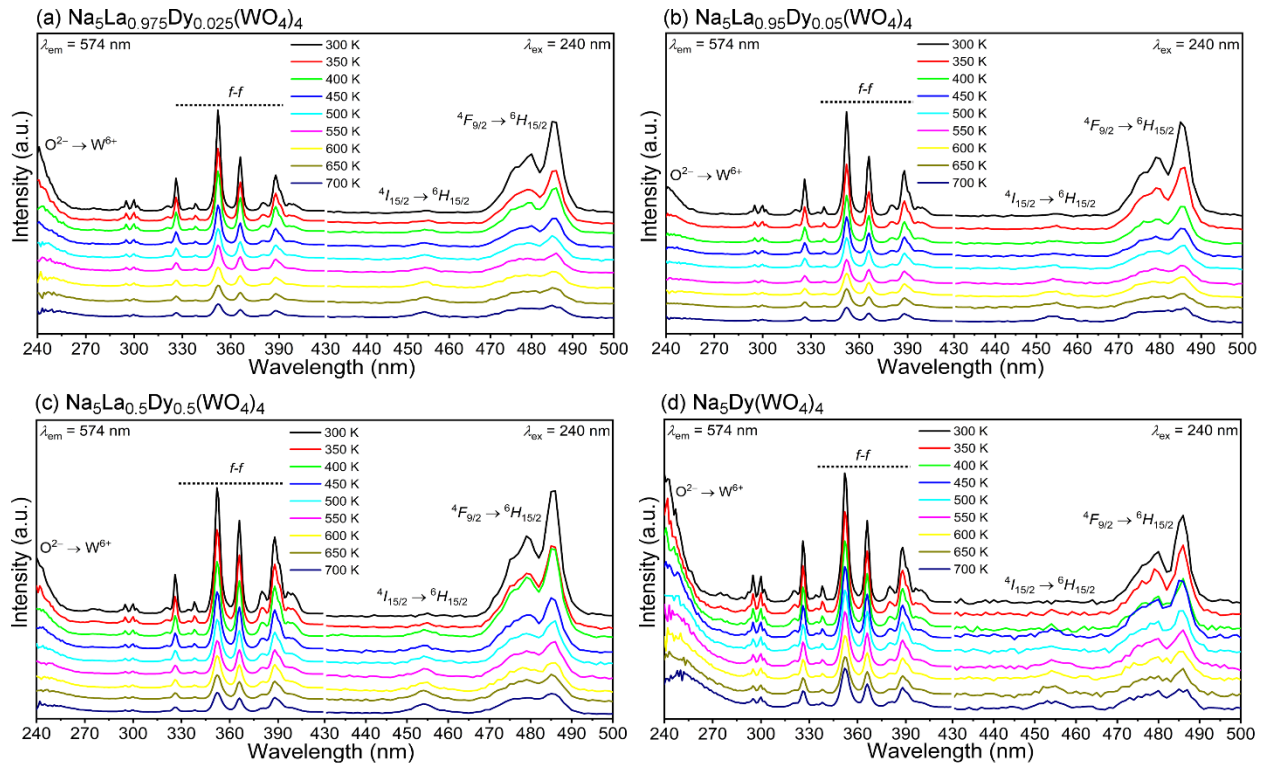


**Figure 3.10.** Temperature-dependent excitation and emission spectra of the  $\text{NaLa}_{1-x}\text{Dy}_x(\text{WO}_4)_4$  series in the 300–700 K temperature range.

bands arise from the radiative relaxation of thermally coupled levels  ${}^4I_{15/2}$  and  ${}^4F_{9/2}$  to the  ${}^6H_{15/2}$  ground state and impart optical temperature sensing functionality to the phosphors. Emission from the thermally coupled upper level  ${}^4I_{15/2}$  was not observed below room temperature. Therefore, temperature-dependent emission spectra were collected in the 300–700 K temperature range. Emission spectra were quantitatively analyzed to assess the performance of dysprosium-activated scheelite-type oxides as thermosensitive phosphors. To this end, the following three metrics were computed from the temperature-dependent emission spectra: luminescence intensity ratio  $R(T)$  (equation (1.1)), absolute sensitivity  $S_A$  (equation (1.3)), and relative sensitivity  $S_R$  (equation (1.4)). Relative sensitivity values allow the performance of thermosensitive phosphors to be compared.

$R(T)$  values were computed using the integrated intensities of the emission bands centered at 454 ( $I({}^4I_{15/2} \rightarrow {}^6H_{15/2})$ ) and 484 nm ( $I({}^4F_{9/2} \rightarrow {}^6H_{15/2})$ ). In the case of  $\text{NaLa}_{1-x}\text{Dy}_x(\text{MO}_4)_2$ , integrated intensities were obtained by fitting the band at 484 nm with two Gaussian curves. For  $\text{Na}_5\text{La}_{1-x}\text{Dy}_x(\text{MO}_4)_4$ , this band was fit with three Gaussian curves. The temperature dependence of  $R(T)$ ,  $S_A$ , and  $S_R$  values is shown in **Figures 3.12a–c** for  $\text{Na}_5\text{La}_{0.95}\text{Dy}_{0.05}(\text{MoO}_4)_2$ ,  $\text{Na}_5\text{La}_{0.975}\text{Dy}_{0.025}(\text{WO}_4)_2$ ,  $\text{Na}_5\text{La}_{0.9}\text{Dy}_{0.1}(\text{MoO}_4)_4$ , and  $\text{Na}_5\text{La}_{0.9}\text{Dy}_{0.1}(\text{WO}_4)_4$ ; plots for other compositions are provided in the **Figures 3.13 and 3.14**. All four compositions shown in **Figure 3.12a** display nearly identical  $R(T)$  values in the entire temperature range. Maxima are observed at 700 K, reflecting the thermalization of the  ${}^4F_{9/2}$  level to populate the  ${}^4I_{15/2}$  level.



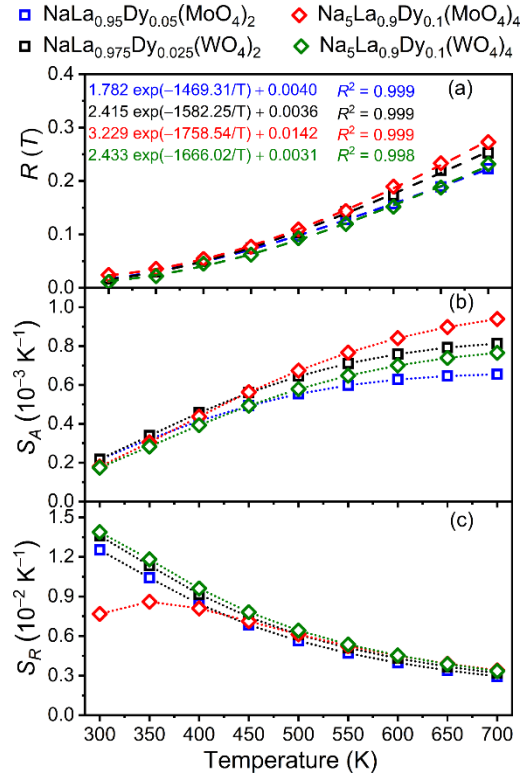


**Figure 3.12.** (a) Luminescence intensity ratio ( $R(T)$ ), (b) absolute sensitivity ( $S_A$ ), and (c) relative sensitivity ( $S_R$ ) of  $\text{NaLa}_{0.95}\text{Dy}_{0.05}(\text{MoO}_4)_2$ ,  $\text{NaLa}_{0.975}\text{Dy}_{0.025}(\text{WO}_4)_2$ ,  $\text{Na}_5\text{La}_{0.9}\text{Dy}_{0.1}(\text{MoO}_4)_4$ , and  $\text{Na}_5\text{La}_{0.9}\text{Dy}_{0.1}(\text{WO}_4)_4$ . Analytical expressions used to fit experimental  $R(T)$  values are given. The corresponding fits are depicted as dashed lines and  $R^2$  residuals are given. Dotted lines shown in (b) and (c) are guides-to-the-eye.

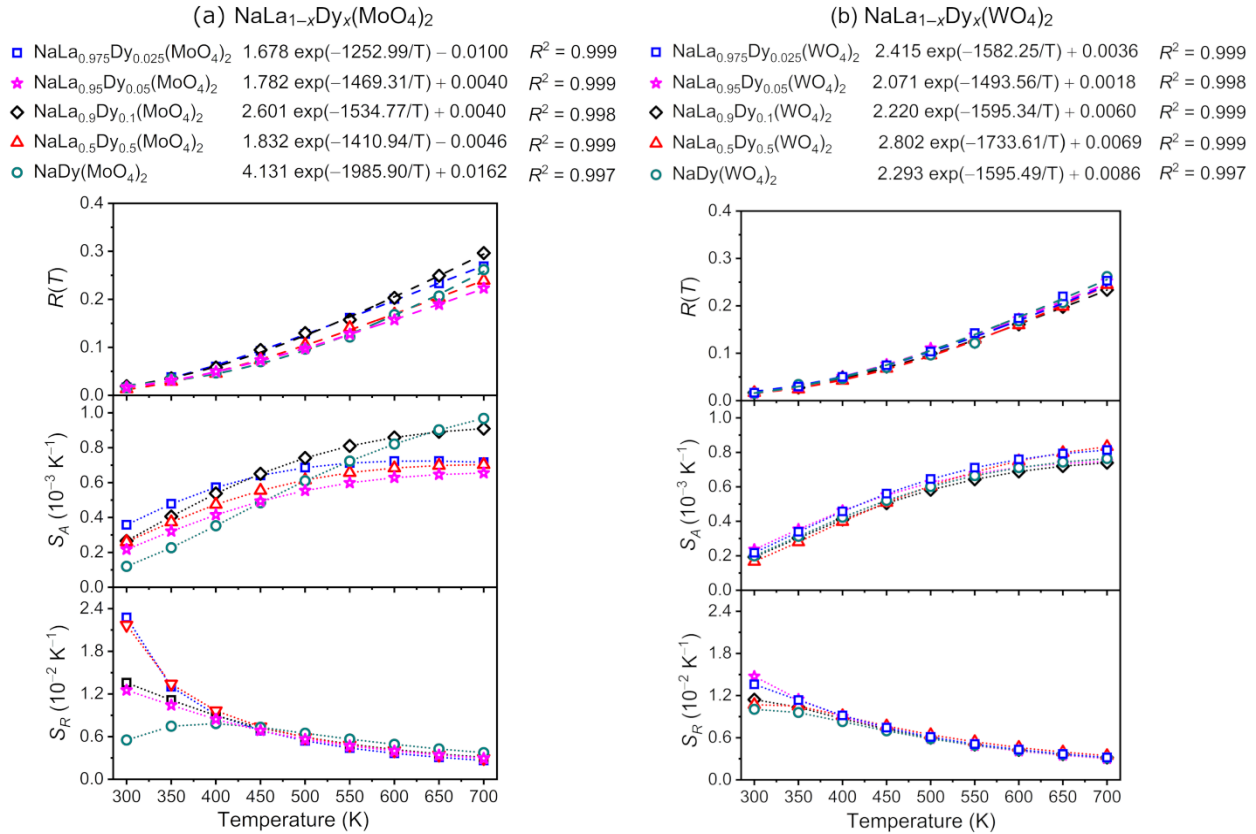


**Figure 3.13.** Luminescence intensity ratio ( $R(T)$ ), absolute sensitivity ( $S_A$ ), and relative sensitivity ( $S_R$ ) of phosphors belonging to the (a)  $\text{NaLa}_{1-x}\text{Dy}_x(\text{MoO}_4)_2$  and (b)  $\text{NaLa}_{1-x}\text{Dy}_x(\text{WO}_4)_2$  series. Analytical expressions used to fit experimental  $R(T)$  values are given. The corresponding fits are depicted as dashed lines and  $R^2$  residuals are given. Dotted lines shown in  $S_A(T)$  and  $S_R(T)$  plots are guides-to-the-eye.

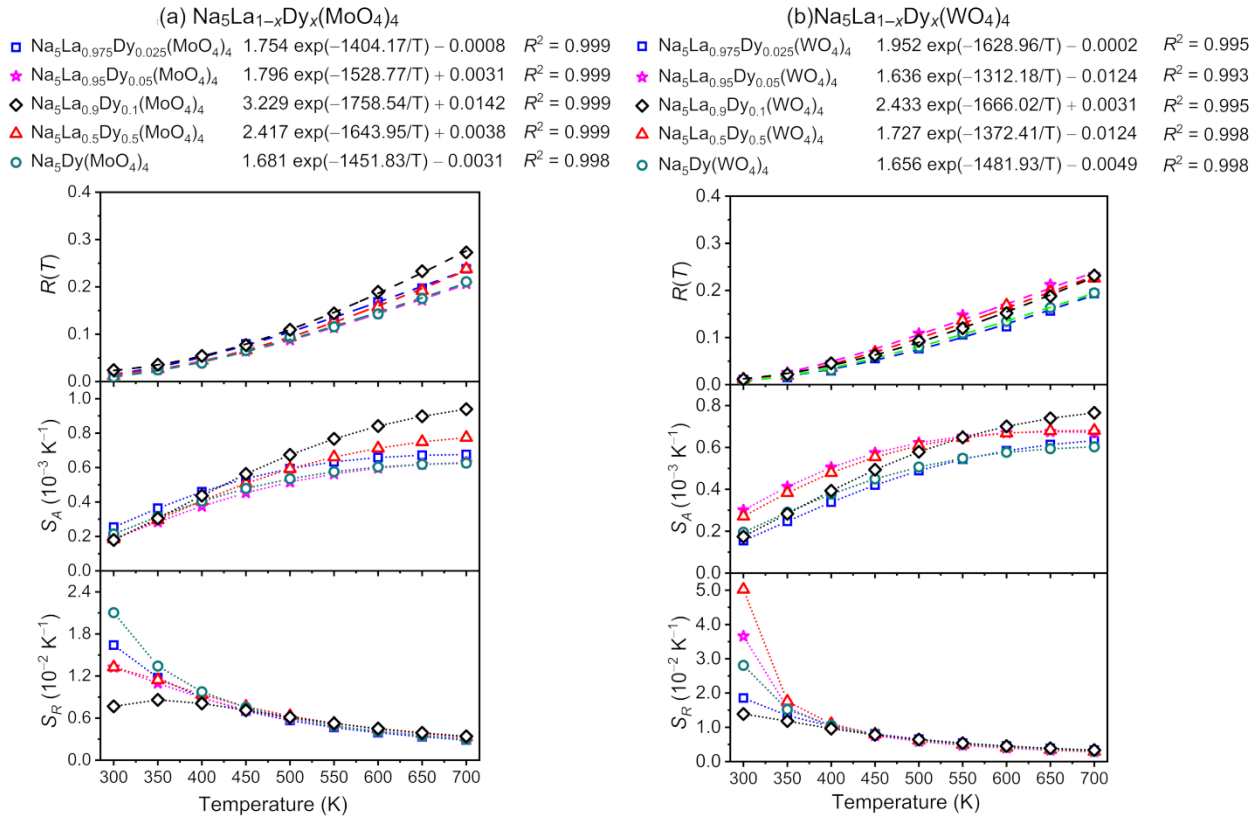


**Figure 3.14.** Luminescence intensity ratio ( $R(T)$ ), absolute sensitivity ( $S_A$ ), and relative sensitivity ( $S_R$ ) of phosphors belonging to the (a)  $\text{Na}_5\text{La}_{1-x}\text{Dy}_x(\text{MoO}_4)_4$  and (b)  $\text{Na}_5\text{La}_{1-x}\text{Dy}_x(\text{WO}_4)_4$  series. Analytical expressions used to fit experimental  $R(T)$  values are given. The corresponding fits are depicted as dashed lines and  $R^2$  residuals are given. Dotted lines shown in  $S_A(T)$  and  $S_R(T)$  plots are guides-to-the-eye.

Experimental  $R(T)$  values were fit with a Boltzmann-type distribution given by equation (1.2).<sup>20,21</sup> Adequate fits were obtained for all the compositions under investigation, validating thermal coupling (see also **Figures 3.15**). Calculated energy gaps ( $\Delta E_{fit}$ ), however, are systematically smaller than experimental values ( $\Delta E_{exp}$ ) estimated by computing the difference between the positions of the centroids of the 454 and 484 nm bands at 350 K (**Table 3.3**). Underestimation of the energy gap ranges from 95 to 350  $\text{cm}^{-1}$ . Exceptions to this trend are observed for (i)  $\text{NaLa}_{0.5}\text{Dy}_{0.5}(\text{WO}_4)_2$  and  $\text{Na}_5\text{La}_{0.9}\text{Dy}_{0.1}(\text{MoO}_4)_2$ , for which the calculated and experimental energy gaps show a nearly perfect match, and (ii)  $\text{NaDy}(\text{MoO}_4)_2$ , in which the

experimental gap is overestimated by  $162 \text{ cm}^{-1}$ . Discrepancies between calculated and experimental energy gaps reveal that temperature-dependent energy-transfer processes other than thermalization operate in almost all of the phosphors under investigation. Examples of these processes may include the nonradiative relaxation of the higher-lying levels to populate the  ${}^4I_{15/2}$  thermally coupled upper level and phonon-assisted cross-relaxation between the  ${}^4F_{9/2}$  and  ${}^6H_{15/2}$  levels of two  $\text{Dy}^{3+}$  activators.<sup>68-69</sup> Thermometric sensitivity values demonstrate, however, that the extent to which energy-transfer processes other than thermalization operate is not significant enough to cause a noticeable difference in thermometric performance, particularly above 400 K (vide infra). Absolute thermometric sensitivities increase with temperature and reach their maxima at 700 K, as shown in **Figure 3.12b**. More importantly, relative sensitivities shown in **Figure 3.12c** reveal that the thermometric performance of the phosphors above 400 K is nearly independent of chemical composition and crystal structure. Above this temperature,  $S_R(T)$  curves for all four compositions overlap and sensitivity values decrease to reach a minimum at 700 K.

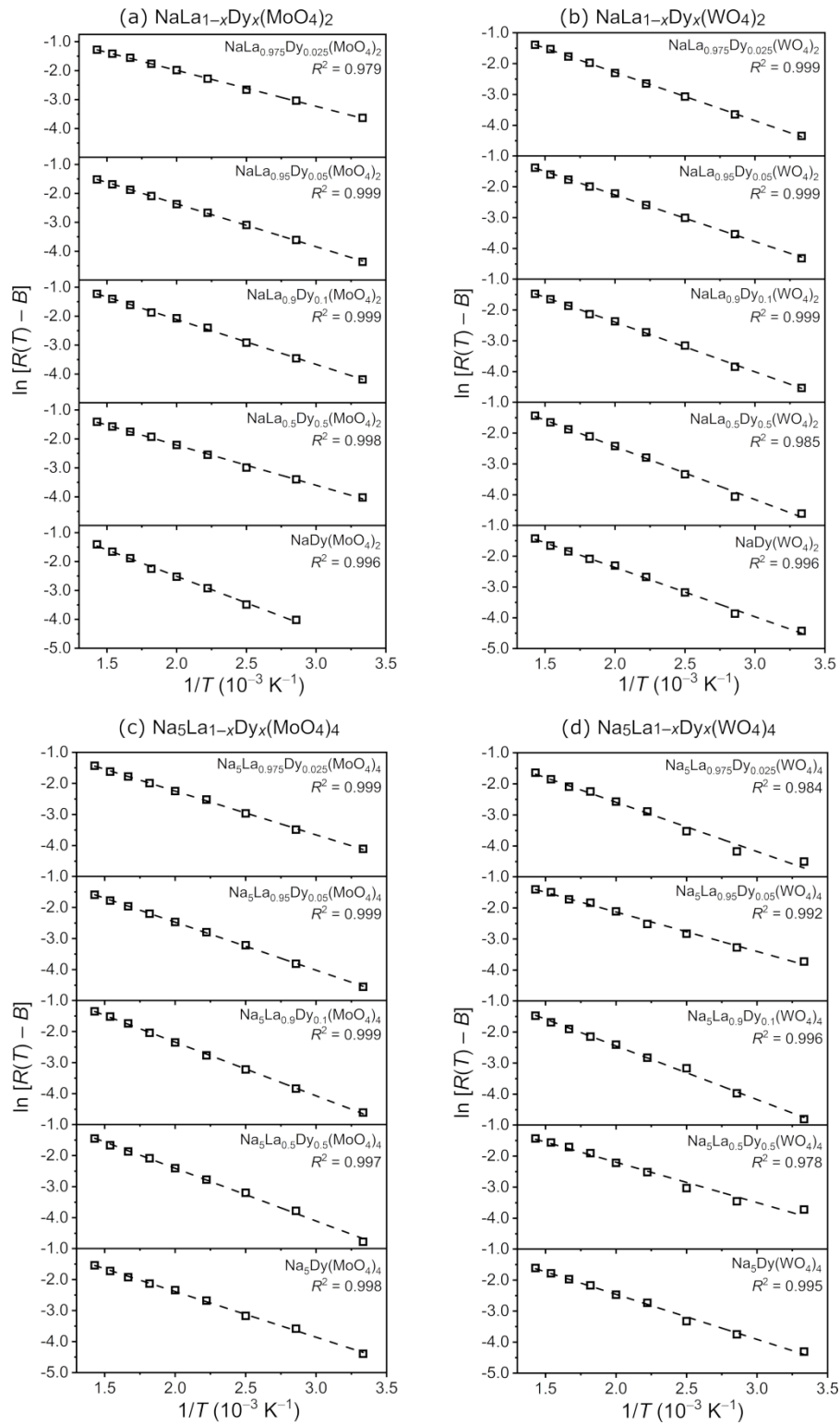


**Figure 3.15.** Arrhenius-type plots for phosphors belonging to the (a)  $\text{NaLa}_{1-x}\text{Dy}_x(\text{MoO}_4)_2$ ,  $\text{NaLa}_{1-x}\text{Dy}_x(\text{WO}_4)_2$ ,  $\text{Na}_5\text{La}_{1-x}\text{Dy}_x(\text{MoO}_4)_4$ , and  $\text{Na}_5\text{La}_{1-x}\text{Dy}_x(\text{WO}_4)_4$ .

**Table 3.3.** Experimental and Calculated Energy Gap Between Thermally Coupled Levels of Dy<sup>3+</sup>

Composition	$\Delta E_{exp}$ (cm <sup>-1</sup> )	$\Delta E_{fit}$ (cm <sup>-1</sup> )	$\Delta E_{fit} - \Delta E_{exp}$ (cm <sup>-1</sup> )
NaLa <sub>0.975</sub> Dy <sub>0.025</sub> (MoO <sub>4</sub> ) <sub>2</sub>	1222	871	-351
NaLa <sub>0.95</sub> Dy <sub>0.05</sub> (MoO <sub>4</sub> ) <sub>2</sub>	1234	1021	-213
NaLa <sub>0.9</sub> Dy <sub>0.1</sub> (MoO <sub>4</sub> ) <sub>2</sub>	1217	1067	-150
NaLa <sub>0.5</sub> Dy <sub>0.5</sub> (MoO <sub>4</sub> ) <sub>2</sub>	1227	981	-246
NaDy(MoO <sub>4</sub> ) <sub>2</sub>	1218	1380	162
NaLa <sub>0.975</sub> Dy <sub>0.025</sub> (WO <sub>4</sub> ) <sub>2</sub>	1242	1100	-142
NaLa <sub>0.95</sub> Dy <sub>0.05</sub> (WO <sub>4</sub> ) <sub>2</sub>	1227	1038	-189
NaLa <sub>0.9</sub> Dy <sub>0.1</sub> (WO <sub>4</sub> ) <sub>2</sub>	1233	1109	-124
NaLa <sub>0.5</sub> Dy <sub>0.5</sub> (WO <sub>4</sub> ) <sub>2</sub>	1218	1205	-13
NaDy(WO <sub>4</sub> ) <sub>2</sub>	1264	1109	-155
Na <sub>5</sub> La <sub>0.975</sub> Dy <sub>0.025</sub> (MoO <sub>4</sub> ) <sub>4</sub>	1207	976	-231
Na <sub>5</sub> La <sub>0.95</sub> Dy <sub>0.05</sub> (MoO <sub>4</sub> ) <sub>4</sub>	1235	1063	-172
Na <sub>5</sub> La <sub>0.9</sub> Dy <sub>0.1</sub> (MoO <sub>4</sub> ) <sub>4</sub>	1230	1222	-8
Na <sub>5</sub> La <sub>0.5</sub> Dy <sub>0.5</sub> (MoO <sub>4</sub> ) <sub>4</sub>	1240	1143	-97
Na <sub>5</sub> Dy(MoO <sub>4</sub> ) <sub>4</sub>	1195	1009	-186
Na <sub>5</sub> La <sub>0.975</sub> Dy <sub>0.025</sub> (WO <sub>4</sub> ) <sub>4</sub>	1229	1132	-97
Na <sub>5</sub> La <sub>0.95</sub> Dy <sub>0.05</sub> (WO <sub>4</sub> ) <sub>4</sub>	1199	912	-287
Na <sub>5</sub> La <sub>0.9</sub> Dy <sub>0.1</sub> (WO <sub>4</sub> ) <sub>4</sub>	1253	1158	-95
Na <sub>5</sub> La <sub>0.5</sub> Dy <sub>0.5</sub> (WO <sub>4</sub> ) <sub>4</sub>	1210	954	-256
Na <sub>5</sub> Dy(WO <sub>4</sub> ) <sub>4</sub>	1253	1030	-223

Relative thermometric sensitivity was systematically mapped at 350 and 700 K as a function of the host composition and activator concentration to identify compositions that exhibit maximum sensitivity. Maps of  $S_R$  values for all four metalate series and Dy<sup>3+</sup> concentrations studied in this work are shown in **Figure 3.16**. Inspection of maps at 350 and 700 K confirms that sensitivity values show little dependence on host composition and activator concentration.

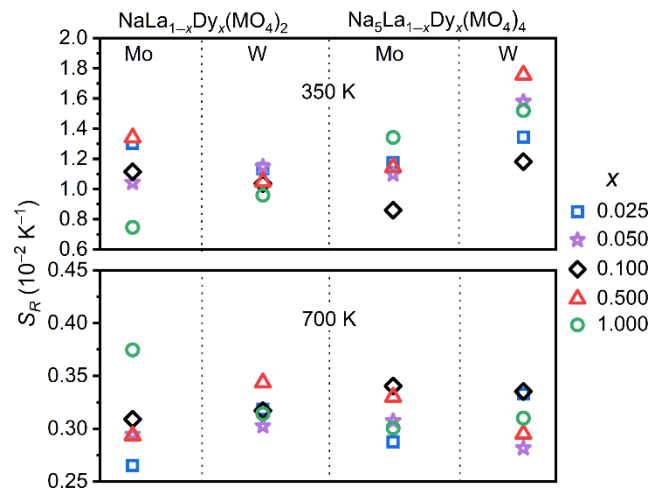


**Figure 3.16.** Map of relative sensitivity values at 350 and 700 K as a function of host composition and  $\text{Dy}^{3+}$  concentration.

Comparison of  $S_R$  values between different metalate series show that at 350 K almost all values fall within the  $1.0 \times 10^{-2} - 1.6 \times 10^{-2} \text{ K}^{-1}$  range. Likewise, at 700 K  $S_R$  values span a narrow range that goes from  $2.8 \times 10^{-3}$  to  $3.8 \times 10^{-3} \text{ K}^{-1}$ . Similar findings were reported by Nikolić et al. for a series of  $\text{Dy}^{3+}$ -activated  $\text{GdVO}_4$  phosphors.<sup>70</sup> The highest relative sensitivity is observed at 350 K for  $\text{Na}_5\text{La}_{0.5}\text{Dy}_{0.5}(\text{WO}_4)_4$  with a value of  $1.8 \times 10^{-2} \text{ K}^{-1}$ , indicating this is the best thermosensitive phosphor for near-room-temperature sensing. Mapping  $S_R$  values at 300 K further supports this conclusion (see **Figure 3.17**), although relative sensitivities computed at that temperature are less reliable as they tend to be affected by mathematical artifacts. At 700 K, the highest relative sensitivity is observed for  $\text{NaDy}(\text{MoO}_4)_2$  with a value of  $3.8 \times 10^{-3} \text{ K}^{-1}$ . Comparison of  $S_R$  values within any of the metalate series under investigation shows the lack of a clear dependence on  $\text{Dy}^{3+}$  concentration. At first this may suggest that the balance between energy-transfer processes that govern the thermometric sensitivity of  $\text{NaLa}_{1-x}\text{Dy}_x(\text{MO}_4)_2$  and  $\text{Na}_5\text{La}_{1-x}\text{Dy}_x(\text{MO}_4)_4$  shows little dependence on crystal-chemistry. A more sensible explanation is that crystal-chemical features common to both series of compounds (e.g., the vibrational energies of the  $\text{REO}_8$  and  $\text{MO}_4$  groups)

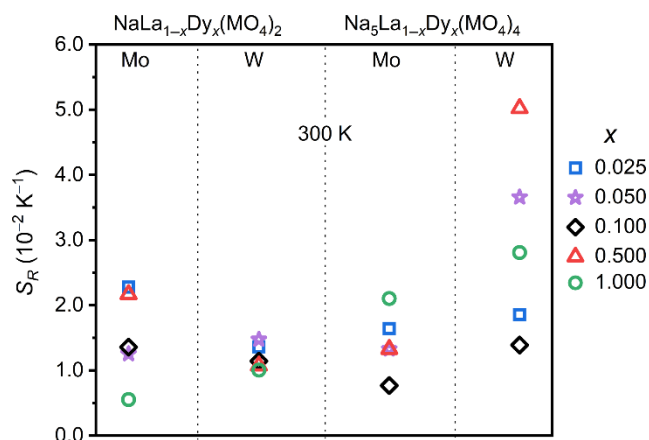


**Figure 3.17.** Map of relative sensitivity values at 300 K as a function of host composition and  $Dy^{3+}$  concentration.

dominate this balance, with differences in the dimensionality of the rare-earth sublattice and  $DyO_8-MO_4$  connectivity playing only a minor role. Regarding  $Dy^{3+}-Dy^{3+}$  interatomic distances and their effect on thermometric sensitivity, we note here that if this dependence exists, accurately establishing it requires structural models that account for activator clustering<sup>49, 71</sup> and rotational disorder of  $MO_4^{2-}$  tetrahedra,<sup>72-73</sup> phenomena that are known to occur in scheelite and scheelite-type oxides. In the absence of adequate models that account for local deviations from the average structure, systematically mapping thermometric sensitivity as a function of host composition and activator concentration appears to be a feasible approach to identify thermosensitive phosphors with maximum sensitivity. Inspection of  $S_R$  values given in **Table 3.4.** shows that the thermometric performance of scheelite-type oxides at 350 and 700 K is comparable to that reported for other  $Dy^{3+}$ -activated thermosensitive phosphors, including vanadates,<sup>70, 74</sup> niobates,<sup>75</sup> aluminates,<sup>76-77</sup> silicates,<sup>77</sup> titanates,<sup>15</sup> zirconates,<sup>77</sup> and fluorides.<sup>16</sup> This comparison highlights the potential of scheelite-type phosphors as optical sensors for intermediate temperatures (<1000 K).



**Table 3.4.** Relative Thermometric Sensitivities  $S_R$  ( $K^{-1}$ ) of  $Dy^{3+}$ -Activated Phosphors

Host	350 K	700 K	Reference
$NaDy(MoO_4)_2$	$7.5 \times 10^{-3}$	$3.8 \times 10^{-3}$	This work
$Na_5La_{0.5}Dy_{0.5}(WO_4)_4$	$1.8 \times 10^{-2}$	$3.0 \times 10^{-3}$	This work
$SrWO_4^a$	$1.7 \times 10^{-2}$		4
$GdVO_4$	$9 \times 10^{-3}$ – $1.3 \times 10^{-2}$	$4.0 \times 10^{-3}$ (675K)	20
$GdVO_4$	$1.5 \times 10^{-2}$		37
$YNbO_4$	$1.4 \times 10^{-2}$	$3.6 \times 10^{-3}$	54
$Y_4Al_2O_9$		$4.0 \times 10^{-3}$	55
$Y_3Al_5O_{12}$		$4.4 \times 10^{-3}$	56
$YAlO_3$		$4.7 \times 10^{-3}$	56
$Y_2SiO_5$		$4.1 \times 10^{-3}$	56
$Ca_2Al_2SiO_7$		$3.2 \times 10^{-3}$	56
$Gd_2Ti_2O_7$	$1.2 \times 10^{-2}$		57
$Y_2Zr_2O_7$		$5.6 \times 10^{-3}$	56
$BaYF_5$	$1.1 \times 10^{-2}$	$2.5 \times 10^{-3}$	58

<sup>a</sup> Codoped with  $Eu^{3+}$  and  $Dy^{3+}$ .

With this perspective in mind, we evaluated the repeatability and temperature resolution of  $NaDy(MoO_4)_2$  at 700 K and of  $Na_5La_{0.5}Dy_{0.5}(WO_4)_4$  at 350 K. Repeatability was probed by subjecting these phosphors to 10 heating–cooling cycles and extracting luminescence intensity ratios at the temperature of interest. Then, repeatability was calculated using equation (1.5). Results from repeatability tests are plotted in **Figure 3.18**; numeric data are given in the **Table 3.5**. The repeatability of  $NaDy(MoO_4)_2$  at 700 K was found to be 97.4% while that of  $Na_5La_{0.5}Dy_{0.5}(WO_4)_4$  at 350 K was equal to 93.4%. Next, the temperature resolution ( $\Delta T$ ) of the phosphors was estimated using two methods. In the first approach, it was computed using equation (1.6).  $\Delta R$  was estimated by collecting 50 spectra at the temperature of interest (700 K for  $NaDy(MoO_4)_2$  and 350 K for  $Na_5La_{0.5}Dy_{0.5}(WO_4)_4$ ). In the second approach, these 50 spectra and the corresponding  $R(T)$  calibration curve were used to calculate a series of temperature values. The standard deviation of these values was taken as an estimate of the phosphor's temperature

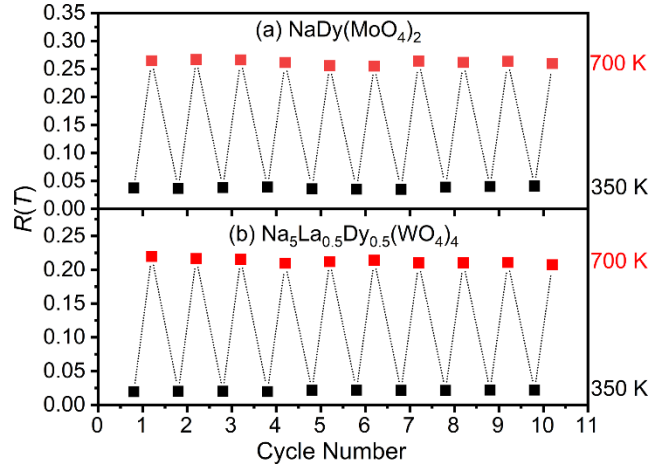


**Figure 3.18.** Luminescence intensity ratios of (a)  $\text{NaDy}(\text{MoO}_4)_2$  and (b)  $\text{Na}_5\text{La}_{0.5}\text{Dy}_{0.5}(\text{WO}_4)_4$  as a function of the heating–cooling cycle number.

**Table 3.5.** Repeatability of  $\text{NaDy}(\text{MoO}_4)_2$  (at 700 K) and  $\text{Na}_5\text{La}_{0.5}\text{Dy}_{0.5}(\text{WO}_4)_4$  (at 350 K)

$\text{NaDy}(\text{MoO}_4)_2$			$\text{Na}_5\text{La}_{0.5}\text{Dy}_{0.5}(\text{WO}_4)_4$		
Cycle #	$R(350\text{ K})$	$R(700\text{ K})$	Cycle #	$R(350\text{ K})$	$R(700\text{ K})$
1	0.03740	0.26476	1	0.01953	0.21956
2	0.03680	0.26672	2	0.02004	0.21657
3	0.03836	0.26638	3	0.02021	0.21530
4	0.03902	0.26159	4	0.01959	0.20966
5	0.03605	0.25586	5	0.02163	0.21205
6	0.03513	0.25507	6	0.02179	0.21392
7	0.03496	0.26408	7	0.02136	0.21019
8	0.03888	0.26166	8	0.02122	0.21029
9	0.04002	0.26370	9	0.02188	0.21067
10	0.04093	0.25978	10	0.02184	0.20738
$\langle R(700\text{ K}) \rangle$		0.26196	$\langle R(350\text{ K}) \rangle$		0.02091

resolution. Resolutions of 7.1 and 0.58 K were estimated for  $\text{NaDy}(\text{MoO}_4)_2$  at 700 K and for  $\text{Na}_5\text{La}_{0.5}\text{Dy}_{0.5}(\text{WO}_4)_4$  at 350 K, respectively. **Table 3.6** summarizes the thermometric performance of  $\text{NaDy}(\text{MoO}_4)_2$  and  $\text{Na}_5\text{La}_{0.5}\text{Dy}_{0.5}(\text{WO}_4)_4$ ; numeric data used to estimate resolution values are given in the **Tables 3.7 and 3.8**. **Table 3.6** also includes the mean values of the calculated temperatures,  $\langle T_{\text{calculated}} \rangle$ . For both phosphors, mean calculated temperatures were remarkably

close to the expected values (701 vs 700 K for  $\text{NaDy}(\text{MoO}_4)_2$  and 352 vs 300 K for  $\text{Na}_5\text{La}_{0.5}\text{Dy}_{0.5}(\text{WO}_4)_4$ ). Altogether, metrics given in **Table 3.6** provide a comprehensive evaluation of the sensitivity, resolution, accuracy, and repeatability of two scheelite-type thermosensitive phosphors and further underscore their potential as optical temperature sensors for intermediate temperatures.

**Table 3.6.** Thermometric Performance of  $\text{Dy}^{3+}$ -Activated Phosphors

	$\text{NaDy}(\text{MoO}_4)_2$ at 700 K	$\text{Na}_5\text{La}_{0.5}\text{Dy}_{0.5}(\text{WO}_4)_4$ at 350 K
Absolute Sensitivity $S_A$ ( $\text{K}^{-1}$ )	$9.8 \times 10^{-4}$	$3.8 \times 10^{-4}$
Relative Sensitivity $S_R$ ( $\text{K}^{-1}$ )	$3.8 \times 10^{-3}$	$1.8 \times 10^{-2}$
Repeatability (%) <sup>a</sup>	97.4	93.4
Resolution $\Delta T$ (K) <sup>b</sup>	7.1 <sup>c</sup>	0.58 <sup>c</sup>
	7.1 <sup>d</sup>	0.57 <sup>d</sup>
$\langle T_{\text{calculated}} \rangle$ (K) <sup>b</sup>	701	352

<sup>a</sup> Computed over 10 cycles.

<sup>b</sup> Computed using 50 spectral acquisitions.

<sup>c</sup> Computed using equation (6).

<sup>d</sup> Computed using calculated temperatures; see text for details.

**Table 3.7.** Temperature Resolution of NaDy(MoO<sub>4</sub>)<sub>2</sub> at 700 K

Spectrum #	$R(700\text{ K})$	Calculated $T^a$	Spectrum #	$R(700\text{ K})$	Calculated $T^a$
1	0.26898	710.80255	26	0.25939	701.10351
2	0.27030	712.13266	27	0.27039	712.22242
3	0.25419	695.78642	28	0.26785	709.66535
4	0.24905	690.51080	29	0.25020	691.69456
5	0.25146	692.98239	30	0.24556	686.90002
6	0.25817	699.85871	31	0.25922	700.92676
7	0.26716	708.97478	32	0.25876	700.45376
8	0.25215	693.69335	33	0.25344	695.02166
9	0.26268	704.44389	34	0.27016	711.99329
10	0.25637	698.01943	35	0.25350	695.08239
11	0.26245	704.20789	36	0.26460	706.38526
12	0.25282	694.38391	37	0.26062	702.35029
13	0.25451	696.11411	38	0.26127	703.01185
14	0.24975	691.22516	39	0.26710	708.91073
15	0.26687	708.67517	40	0.25543	697.05638
16	0.25072	692.22657	41	0.24551	686.84588
17	0.25934	701.04886	42	0.25833	700.01542
18	0.25510	696.71591	43	0.25884	700.53738
19	0.26155	703.29918	44	0.26067	702.39642
20	0.25894	700.63958	45	0.25563	697.26751
21	0.27099	712.82284	46	0.27383	715.66822
22	0.26033	702.05381	47	0.26527	707.06551
23	0.26579	707.59089	48	0.26601	707.81352
24	0.25822	699.90434	49	0.25427	695.87480
25	0.26222	703.97587	50	0.26697	708.77451
			Mean	0.25966	701.34253
			Standard Deviation	0.00698	7.10856
			$\Delta T$	7.1	7.1

<sup>a</sup> Calculated using  $R(T) = 4.131 \exp(-1985.90/T) + 0.0162$

**Table 3.8.** Temperature Resolution of Na<sub>5</sub>La<sub>0.5</sub>Dy<sub>0.5</sub>(WO<sub>4</sub>)<sub>4</sub> at 350 K

Spectrum #	R(350 K)	Calculated $T^a$	Spectrum #	R(350 K)	Calculated $T^a$
1	0.02255	351.86990	26	0.02252	351.77547
2	0.02225	351.08964	27	0.02225	351.07979
3	0.02196	350.33916	28	0.02251	351.77072
4	0.02258	351.94231	29	0.02258	351.93311
5	0.02249	351.70913	30	0.02272	352.28972
6	0.02275	352.37755	31	0.02274	352.36214
7	0.02281	352.54111	32	0.02282	352.54922
8	0.02241	351.49645	33	0.02310	353.27866
9	0.02226	351.11792	34	0.02297	352.94396
10	0.02271	352.26827	35	0.02255	351.87291
11	0.02246	351.62455	36	0.02249	351.71568
12	0.02244	351.58084	37	0.02270	352.25040
13	0.02235	351.35685	38	0.02269	352.22576
14	0.02235	351.33882	39	0.02249	351.70458
15	0.02264	352.09624	40	0.02257	351.91770
16	0.02263	352.07796	41	0.02255	351.87005
17	0.02250	351.72238	42	0.02259	351.96703
18	0.02293	352.83334	43	0.02288	352.70255
19	0.02264	352.10291	44	0.02281	352.52395
20	0.02264	352.09170	45	0.02281	352.52985
21	0.02285	352.62492	46	0.02231	351.24184
22	0.02277	352.42179	47	0.02237	351.40244
23	0.02276	352.39538	48	0.02257	351.92618
24	0.02206	350.58876	49	0.02262	352.05415
25	0.02256	351.88964	50	0.02247	351.64619
			Mean	0.02258	351.94063
			Standard Deviation	0.00022	0.57482
			$\Delta T$ (K)	0.58	0.57

<sup>a</sup> Calculated using  $R(T) = 1.727 \exp(-1372.41/T) - 0.0124$

### 3.4. Conclusions

The potential of  $\text{NaLa}_{1-x}\text{Dy}_x(\text{MO}_4)_2$  and  $\text{Na}_5\text{La}_{1-x}\text{Dy}_x(\text{MO}_4)_4$  as thermosensitive phosphors in the 300–700 K temperature range was assessed. Their relative thermometric sensitivity was systematically mapped as a function of host composition and activator concentration. Doing so, we identified compositions that provide maximum thermometric sensitivity. At 350 K, the highest relative sensitivity was observed for  $\text{Na}_5\text{La}_{0.5}\text{Dy}_{0.5}(\text{WO}_4)_4$  ( $1.8 \times 10^{-2} \text{ K}^{-1}$ ), while at 700 K the sensitivity was maximum for  $\text{NaDy}(\text{MoO}_4)_2$  ( $3.8 \times 10^{-3} \text{ K}^{-1}$ ). Comparison of these values with those reported for other dysprosium-activated phosphors revealed the potential of scheelite-type oxides as optical sensors for intermediate temperatures. Quantitative evaluation of the temperature resolution, accuracy, and repeatability of  $\text{NaDy}(\text{MoO}_4)_2$  and  $\text{Na}_5\text{La}_{0.5}\text{Dy}_{0.5}(\text{WO}_4)_4$  further highlighted this potential. From the perspective of utilizing compositional tuning to maximize the thermometric sensitivity of dysprosium-activated scheelites, we observed that sensitivity values spanned a narrow range regardless of the host composition and activator concentration. Therefore, we propose that coupling dysprosium to other rare-earth metals and exploiting temperature-dependent energy-transfer between both emitters may serve as the best alternative to provide a significant increase in the thermometric sensitivity of scheelite-type oxides.

## CHAPTER 4. SYNTHESIS, STRUCTURAL CHARACTERIZATION, AND ROOM TEMPERATURE PHOTOLUMINESCENCE OF $\text{NaYb}(\text{MO}_4)_2$ ( $\text{M} = \text{Mo}, \text{W}$ )

*CrystEngComm* **2016**, 18, 5818–5825

### 4.1. Introduction.

Owing to their compositional flexibility, structural versatility, and photoluminescence, double molybdates and tungstates of formula  $\text{ARE}(\text{MO}_4)_2$  ( $\text{A} = \text{Li}, \text{Na}, \text{K}$ ;  $\text{RE} = \text{Y}$ , rare-earth;  $\text{M} = \text{Mo}, \text{W}$ ) are being intensively investigated. Much of this research effort has focused on understanding composition–structure–luminescence relationships in metalates of formula  $\text{ARE}_{1-x}\text{RE}'_x(\text{MO}_4)_2$ , where  $\text{RE}$  is an optically inert ion (e.g.,  $\text{Y}^{3+}$ ,  $\text{La}^{3+}$ ,  $\text{Gd}^{3+}$ ) and  $\text{RE}'$  is an optically active rare-earth ion or pair of ions (e.g.,  $\text{Eu}^{3+}$ ,  $\text{Yb}^{3+}\text{--Er}^{3+}$ ,  $\text{Yb}^{3+}\text{--Tm}^{3+}$ ); the latter are typically incorporated in the host at concentrations below 20 mol. %.<sup>5,44</sup> Investigation of the crystallochemical basis of energy-transfer processes in hosts featuring near unity concentrations of the optically active ions has comparatively languished. Bridging this fundamental knowledge gap is critical to enable the rational design and screening of metalates whose full potential as photoluminescent materials is yet to be realized.

Probing energy-transfer processes in stoichiometric  $\text{NaYb}(\text{MoO}_4)_2$  and  $\text{NaYb}(\text{WO}_4)_2$  and elucidating their chemical and structural bases were the objectives of this investigation. These metalates display a scheelite-type structure with space-group  $I4_1/a$  and a tetragonal unit cell (**Figure 4.1**).  $\text{M}^{6+}$   $d^0$  cations are coordinated by four oxide ions, forming isolated tetrahedra.  $\text{Na}^+$  and  $\text{Yb}^{3+}$  cations are coordinated by eight oxide anions, forming  $\text{NaO}_8$  and  $\text{YbO}_8$  edge-sharing polyhedra. Substitutional disorder is intrinsic to metalates belonging to the  $\text{NaRE}'(\text{MO}_4)_2$  family.

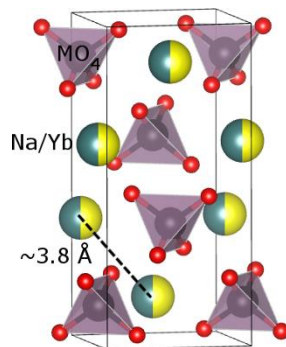


**Figure 4.1.** Crystal structure of  $\text{NaYb}(\text{MoO}_4)_2$ .  $\text{Na}^+$  and  $\text{Yb}^{3+}$  are depicted as statistically distributed over the same crystallographic site. The shortest distance between two adjacent Na/Yb sites in the unit cell is  $\sim 3.8 \text{ \AA}$ .

Ideally,  $\text{Na}^+$  and  $\text{Yb}^{3+}$  are statistically distributed over a  $4b$  site. Recently, however, Arakcheeva et al. proposed a structural picture that goes beyond statistical distribution and in which clustering of the rare-earth ions takes place.<sup>78</sup> Using polycrystalline  $\text{Na}_x\text{Eu}_{(2-x)/3}\text{MoO}_4$  ( $0 \leq x \leq 0.5$ ) synthesized via solid-state reaction, these investigators demonstrated that changing the compositional variable  $x$  leads to modulated structures exhibiting a fully ordered distribution of the  $\text{Eu}^{3+}$  cations. Modulated structures were identified by a series of weak diffraction maxima (i.e., satellites) in the low-angle region of the X-ray diffraction (XRD) patterns. More importantly, it was shown that  $\text{Eu}^{3+}\text{-Eu}^{3+}$  dimers were present in the modulated structures and that the photoluminescence properties of the metalates (e.g., quantum yield, activator's lifetime, host-sensitization efficiency) could be rationalized invoking the concentration of these dimers. This finding highlights the importance of accounting for local clustering of optically active ions to rationalize energy-transfer processes in metalate hosts exhibiting substitutional disorder.

In this work, energy-transfer processes responsible for NIR-to-NIR and NIR-to-blue light upconversion in polycrystalline  $\text{NaYb}(\text{MoO}_4)_2$  and  $\text{NaYb}(\text{WO}_4)_2$  were investigated. Emphasis was placed on elucidating the chemical units responsible for the strong NIR ( $\sim 795 \text{ nm}$ ) and bright



blue (~475 nm) luminescence both metalates exhibited under 973 nm laser excitation. A combination of steady-state and time-dependent spectrofluorometry, elemental analysis, and Rietveld analysis of synchrotron XRD data was employed to this end. Steady-state spectrofluorometry along with chemical analysis showed that NIR emission resulted from energy-transfer from  $\text{Yb}^{3+}$  to  $\text{Tm}^{3+}$  ions, which were found to be present at the trace level (~1 ppm) in both  $\text{NaYb}(\text{MoO}_4)_2$  and  $\text{NaYb}(\text{WO}_4)_2$ . In the case of the blue emission, power-dependence and time-dependent spectrofluorometric studies favored cooperative luminescence of  $\text{Yb}^{3+}\text{-Yb}^{3+}$  dimers,<sup>79</sup> rather than three-photon upconversion from  $\text{Yb}^{3+}$ -sensitized  $\text{Tm}^{3+}$ . Rietveld analysis showed that local clustering of  $\text{Yb}^{3+}$  ions to yield  $\text{Yb}^{3+}\text{-Yb}^{3+}$  dimers that have the potential to interact cooperatively was feasible. The significance of these findings is discussed from the perspective of expanding the compositional library of upconverting metalates, as well as of understanding the structural bases of energy-transfer processes relevant to light absorption and emission in this family of materials.

## 4.2. Experimental

### 4.2.1. Synthesis of $\text{NaYb}(\text{MoO}_4)_2$ and $\text{NaYb}(\text{WO}_4)_2$

Conventional solid-state reaction was employed to synthesize polycrystalline  $\text{NaYb}(\text{MoO}_4)_2$  and  $\text{NaYb}(\text{WO}_4)_2$ . Stoichiometric amounts of  $\text{Na}_2\text{CO}_3$  (99.999%, Sigma-Aldrich),  $\text{Yb}_2\text{O}_3$  (99.99%, Sigma-Aldrich),  $\text{WO}_3$  (99.995%, Sigma-Aldrich) and  $\text{MoO}_3$  (99.999%, Acros Organics) were mixed and ground in an agate mortar. Unreacted powder mixtures were heated under optimized synthesis (see **section 2.2.1.1**) conditions to obtain phase-pure products.

### 4.2.2. Synchrotron Powder X-ray Diffraction

Synchrotron XRD patterns of  $\text{NaYb}(\text{MoO}_4)_2$  and  $\text{NaYb}(\text{WO}_4)_2$  were collected at the 11-BM beamline of the Advanced Photon Source at Argonne National Laboratory. Samples were

packed in Kapton tubes and diffraction patterns were collected in transmission mode at room temperature. An incident photon energy of 29.936 keV ( $\lambda = 0.4141650 \text{ \AA}$ ) was used. The step size and scan speed were  $0.001^\circ$  and  $0.01 \text{ s}^{-1}$ , respectively.

#### 4.2.3. Rietveld Analysis

Rietveld refinements<sup>80-81</sup> of synchrotron XRD patterns were performed using the General Structure Analysis System (GSAS) with the graphical user interphase (EXPGUI) software.<sup>82-83</sup> as mentioned in **section 2.2.2.3**. Experimental data and atomic X-ray scattering factors were corrected for sample absorption and anomalous scattering, respectively. Fractional atomic coordinates of the oxygen atom ( $x_O, y_O, z_O$ ), and an isotropic displacement parameter for each of the atoms of the structure ( $U_{\text{Na/Yb}}, U_M, U_O$ ) were refined. The Na and Yb occupancies of the  $4b$  site ( $x = 0.500, y = 0.750, z = 0.125$ ) were fixed at 0.50.  $R_{\text{wp}}$  and  $\chi^2$  residuals were employed to assess the quality of the refined structural models.<sup>83</sup>

#### 4.2.4. Elemental Analysis.

Inductively coupled plasma mass spectrometry (ICP–MS) was employed to determine the thulium and erbium concentrations in  $\text{NaYb}(\text{MoO}_4)_2$  and  $\text{NaYb}(\text{WO}_4)_2$ . ICP–MS analyses were performed using a 7700 Series ICP–MS analyzer (Agilent Technologies). ~50 mg of powder sample were dissolved in concentrated HCl at  $60^\circ\text{C}$ . Thulium ( $1000 \pm 4 \mu\text{g/mL}$ , 2%  $\text{HNO}_3$ , High Purity Standards) and erbium ( $989 \pm 4 \text{ mg/L}$ , 2%  $\text{HNO}_3$ , Fluka) were used as standards.

#### 4.2.5. Upconversion Spectrofluorometry

Spectrofluorometric analyses were carried out using a Fluorolog 3–222 fluorometer (Horiba Scientific). A PSU–III–LED (Opto Engine, LLC) continuous-wave 973 nm laser ( $140\text{--}930 \text{ mW}$ , beam dimensions  $\sim 5 \times 8 \text{ mm}^2$ ) was used as the excitation source. Spectra in the

300–850 and 900–1050 nm ranges were collected using R928p and R2658p photomultiplier tubes, respectively. Decay curves were collected using the 973 nm laser in pulsed mode (pulse width ~50–100  $\mu$ s). Spectra were recorded at room temperature using a 1–5 nm slit width in the emission monochromator.

### 4.3. Results and Discussion

Rietveld analysis of synchrotron XRD patterns of  $\text{NaYb}(\text{MoO}_4)_2$  and  $\text{NaYb}(\text{WO}_4)_2$  was performed to probe their phase purity, average crystal structure, and relevant interatomic distances. Fits of the scheelite-type tetragonal structure to the experimental patterns are shown in **Figure 4.2**.

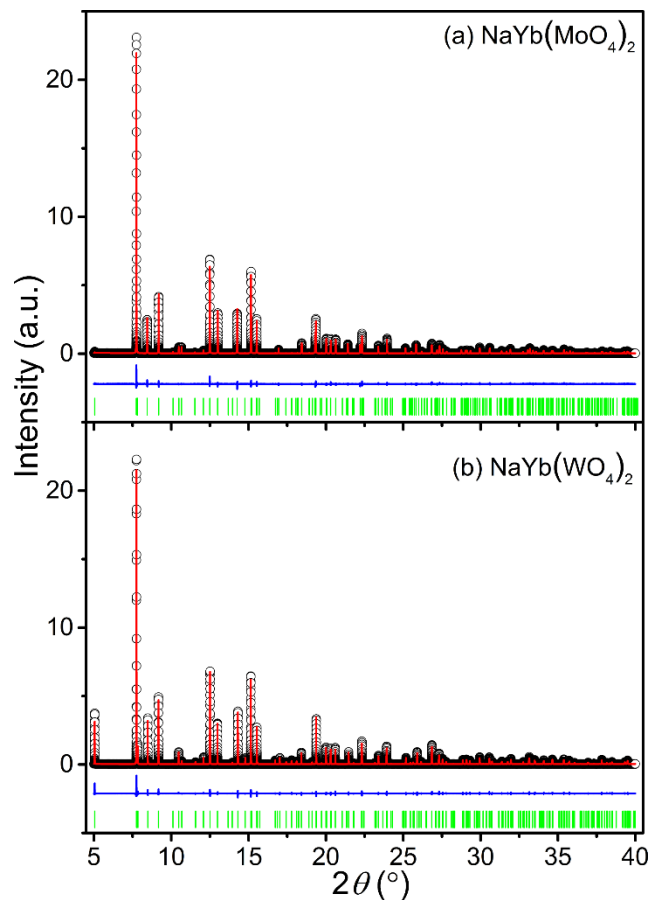


**Figure 4.2.** Rietveld analyses of the synchrotron XRD patterns of (a)  $\text{NaYb}(\text{MoO}_4)_2$  and (b)  $\text{NaYb}(\text{WO}_4)_2$ . The experimental ( $\circ$ ) and calculated ( $—$ ) patterns are shown along with the difference curve ( $—$ ) and the tick marks ( $|$ ).

**Table 4.1.** Structural Parameters of NaYb(MoO<sub>4</sub>)<sub>2</sub> and NaYb(WO<sub>4</sub>)<sub>2</sub>

	NaYb(MoO <sub>4</sub> ) <sub>2</sub>	NaYb(WO <sub>4</sub> ) <sub>2</sub>
<i>a</i> (Å)	5.170642(6)	5.176930(6)
<i>c</i> (Å)	11.245401(18)	11.196785(17)
<i>V</i> (Å <sup>3</sup> )	300.652(2)	300.081(2)
<i>x</i> <sub>O</sub>	0.1526(4)	0.1576(6)
<i>y</i> <sub>O</sub>	0.4900(5)	0.4873(6)
<i>z</i> <sub>O</sub>	0.20841(18)	0.2099(3)
<i>U</i> <sub>Na/Yb</sub> (Å <sup>2</sup> ) <sup>a</sup>	0.64(2)	0.275(9)
<i>U</i> <sub>M</sub> (Å <sup>2</sup> ) <sup>a</sup>	0.548(19)	0.461(6)
<i>U</i> <sub>O</sub> (Å <sup>2</sup> ) <sup>a</sup>	2.19(6)	1.81(9)
<i>R</i> <sub>wp</sub>	9.9	11.6
$\chi^2$	1.21	1.52

<sup>a</sup> Given as 100 × *U*.

Structural parameters extracted from Rietveld analysis are given in **Table 4.1**. All diffraction maxima were indexed to the corresponding molybdate or tungstate phase; no extra peaks corresponding to secondary crystalline phases were observed. Structural parameters given in **Table 4.1** show that the unit cells of NaYb(MoO<sub>4</sub>)<sub>2</sub> and NaYb(WO<sub>4</sub>)<sub>2</sub> were nearly isometric, as expected on the basis of the radii of four-coordinated Mo<sup>6+</sup> (41 pm) and W<sup>6+</sup> (42 pm).<sup>65</sup> The shortest distances between two adjacent Na/Yb sites were 3.81937 and 3.81256 Å for NaYb(MoO<sub>4</sub>)<sub>2</sub> and NaYb(WO<sub>4</sub>)<sub>2</sub>, respectively. The agreement between the experimental and calculated XRD patterns was adequate, as shown by the difference curves in Figure 4.2. The values of the *R*<sub>wp</sub> residuals, however, remained in the 10–12 % range for both structures, suggesting that deviations from the average tetragonal structure were present. Experimental diffraction data did not support a compositional modulation as the origin of these deviations. Indeed, satellite reflections resulting from the long-range ordering of Na<sup>+</sup> and Yb<sup>3+</sup> were not observed, despite the very high signal-to-noise ratio of the diffraction data. As shown by upconversion

spectrofluorometric studies (vide infra), local clustering of  $\text{Yb}^{3+}$  ions may be invoked to rationalize deviations from the average tetragonal structure.

Steady-state emission spectra of  $\text{NaYb}(\text{MoO}_4)_2$  and  $\text{NaYb}(\text{WO}_4)_2$  under 973 nm excitation are shown in **Figure 4.3**. Both spectra were dominated by a strong and broad NIR emission band centered at  $\sim 795$  nm. Additionally, they exhibited weak emission bands in the blue ( $\sim 475$  nm),

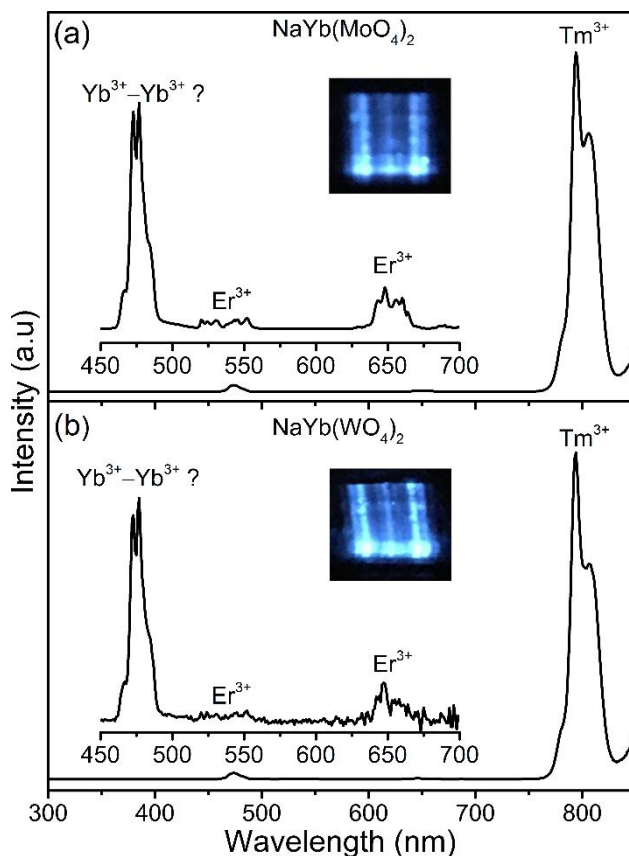


**Figure 4.3.** Upconversion luminescence spectra of (a)  $\text{NaYb}(\text{MoO}_4)_2$  and (b)  $\text{NaYb}(\text{WO}_4)_2$  under 973 nm excitation (490 mW). Spectra collected between 300 and 850 nm (slit width  $\sim 5$  nm) revealed strong NIR emission ( $\sim 795$  nm) due to two-photon upconversion of  $\text{Yb}^{3+}$ -sensitized  $\text{Tm}^{3+}$  impurities ( $\sim 1$  ppm). Insets: spectra collected between 450 and 700 nm (slit width  $\sim 1$  nm) exhibited blue ( $\sim 475$  nm), green ( $\sim 510$ – $560$  nm), and red ( $\sim 640$ – $670$  nm) emission bands. Green and red emissions resulted from two-photon upconversion of  $\text{Yb}^{3+}$ -sensitized  $\text{Er}^{3+}$  impurities ( $\sim 1$  ppm). The likely origin of the blue emission was the cooperative interaction between a pair of neighboring  $\text{Yb}^{3+}$  ions (see text for details). Digital pictures of the polycrystalline powders showing blue emission under 973 nm excitation (650 mW) are provided.

green (~525 and 545 nm), and red (~650 nm) regions. The integrated intensity of the band at ~475 nm was between 60 and 180 times weaker than that of the band at ~795 nm, depending on chemical composition. Despite its weakness relative to the NIR emission, the blue emission was remarkably bright and clearly observable in the entire excitation power range (140–930 mW). Elemental analysis, power-dependence, and time-dependent spectrofluorometric studies were employed to identify the chemical units responsible for the observed NIR and visible upconversion emissions. Owing to the large cross-section of its  $^2F_{7/2} \rightarrow ^2F_{5/2}$  intraconfigurational  $f-f$  transition,  $\text{Yb}^{3+}$  is an efficient NIR absorber (~973 nm). Although single  $\text{Yb}^{3+}$  ions are not visible emitters, they can efficiently sensitize NIR and visible emitters such as  $\text{Tm}^{3+}$  and  $\text{Er}^{3+}$  by sequentially transferring the energy of two, three, or four absorbed NIR photons.<sup>84-85</sup> This results in NIR-to-NIR and NIR-to-visible light upconversion. It has been shown that these sequential energy-transfer steps are efficient enough to observe NIR and visible emission bands even in hosts where the  $\text{Tm}^{3+}$  and  $\text{Er}^{3+}$  activators are present at impurity levels (>10 ppm).<sup>86-88</sup> Unfortunately, the concentration of these impurities is often estimated but seldom quantified.<sup>88</sup> According to ICP-MS, the concentrations of thulium and erbium in  $\text{NaYb}(\text{MoO}_4)_2$  were 1.40 and 1.23 ppm, respectively. This is equivalent to replacing  $8.1 \times 10^{-4}$  mol. % of  $\text{Yb}^{3+}$  with  $\text{Tm}^{3+}$  and  $\text{Er}^{3+}$  and corresponds to a chemical formula  $\text{NaYb}_{0.9999919}\text{Tm}_{0.0000043}\text{Er}_{0.0000038}(\text{MoO}_4)_2$ . Likewise, thulium and erbium concentrations of 1.34 and 1.36 ppm, respectively, were obtained in the case of  $\text{NaYb}(\text{WO}_4)_2$ . This is equivalent to replacing  $1.1 \times 10^{-3}$  mol. % of  $\text{Yb}^{3+}$  with  $\text{Tm}^{3+}$  and  $\text{Er}^{3+}$  and corresponds to a chemical formula  $\text{NaYb}_{0.9999889}\text{Tm}_{0.0000055}\text{Er}_{0.0000056}(\text{WO}_4)_2$ . Therefore, the concentration of  $\text{Tm}^{3+}$  and  $\text{Er}^{3+}$  impurities in the metalate hosts is an order of magnitude smaller than those reported in previous studies of  $\text{Yb}^{3+}$ -sensitized energy-transfer upconversion luminescence. Double logarithmic plots of the emission intensity as a function of the excitation power are given

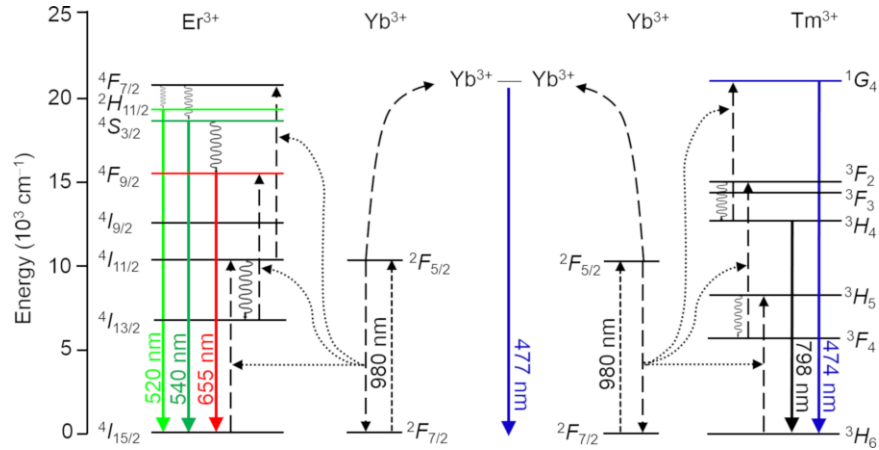


**Figure 4.4.** Dieke diagrams of  $\text{Er}^{3+}$ ,  $\text{Yb}^{3+}$ ,  $\text{Yb}^{3+}\text{-Yb}^{3+}$  dimers, and  $\text{Tm}^{3+}$ . Non-radiative energy-transfer from the  $\text{Yb}^{3+}$  sensitizer to the  $\text{Er}^{3+}$  and  $\text{Tm}^{3+}$  activators is depicted with dotted arrows. Curly arrows indicate vibrational relaxation. Radiative emissions from  $\text{Er}^{3+}$ ,  $\text{Tm}^{3+}$ , and  $\text{Yb}^{3+}\text{-Yb}^{3+}$  dimers are indicated with solid arrows.

in **Figure 4.4** for NIR and visible emission bands. In the low-power regime (i.e., where upconversion to a higher lying level is not the dominant depopulation mechanism), linear fits to these plots serve to estimate the number of upconverted photons.<sup>89</sup> Slopes of 1.6 and 1.7 were obtained for the green bands observed in the spectra of  $\text{NaYb}(\text{MoO}_4)_2$  and  $\text{NaYb}(\text{WO}_4)_2$ , respectively. On this basis, and considering that the  ${}^2\text{H}_{11/2}$  and  ${}^4\text{S}_{3/2}$  levels of  $\text{Er}^{3+}$  are populated via a two-photon upconversion process ( ${}^4\text{I}_{15/2} \xrightarrow{h\nu} {}^4\text{I}_{11/2} \xrightarrow{h\nu} {}^4\text{F}_{7/2} \rightarrow \{{}^2\text{H}_{11/2}, {}^4\text{S}_{3/2}\}$ , see **Figure 4.5**), these bands were assigned to the  ${}^2\text{H}_{11/2} \rightarrow {}^4\text{I}_{15/2}$  ( $\sim 525$  nm) and  ${}^4\text{S}_{3/2} \rightarrow {}^4\text{I}_{15/2}$  ( $\sim 545$  nm) transitions. Similarly, slopes of 1.7 and 1.6 were obtained for the red band observed in the spectra of  $\text{NaYb}(\text{MoO}_4)_2$  and  $\text{NaYb}(\text{WO}_4)_2$ , respectively. Considering that the  ${}^4\text{F}_{9/2}$  level of  $\text{Er}^{3+}$  is populated via two-photon upconversion processes ( ${}^4\text{I}_{15/2} \xrightarrow{h\nu} {}^4\text{I}_{11/2} \xrightarrow{h\nu} {}^4\text{I}_{13/2} \xrightarrow{h\nu} {}^4\text{F}_{9/2}$  and  ${}^4\text{I}_{15/2} \xrightarrow{h\nu} {}^4\text{I}_{11/2} \xrightarrow{h\nu} {}^4\text{F}_{7/2} \rightarrow {}^4\text{F}_{9/2}$ ), the red band was assigned to the  ${}^4\text{F}_{9/2} \rightarrow {}^4\text{I}_{15/2}$  transition.

In light of the results from elemental analysis, the strong NIR band centered at  $\sim 795$  nm was assigned to emission from  $\text{Tm}^{3+}$ .  $\text{Tm}^{3+}$  is a well-known emitter at that wavelength

as a result of its  ${}^3H_4 \rightarrow {}^3H_6$  transition. The  ${}^3H_4$  level of  $Tm^{3+}$  is populated via a two-photon upconversion process ( ${}^3H_6 \xrightarrow{h\nu} {}^3H_5 \rightarrow {}^3F_4 \xrightarrow{h\nu} {}^3F_2 \rightarrow {}^3H_4$ , see **Figure 4.5**). Interestingly, a slope of 1.1 was obtained for the dependence of the emission intensity on the excitation power for both  $NaYb(MoO_4)_2$  and  $NaYb(WO_4)_2$ . This linear dependence demonstrated that the  $Yb^{3+}({}^2F_{5/2}) + Tm^{3+}({}^3F_4) \rightarrow Yb^{3+}({}^2F_{7/2}) + Tm^{3+}({}^3F_2)$  energy-transfer process needed to populate the  ${}^3H_4$  state was saturated throughout the entire excitation power range. This saturation stemmed from the high efficiency of the energy-transfer from the  ${}^2F_{5/2}$  manifold of  $Yb^{3+}$  to the  ${}^3F_4$  level of  $Tm^{3+}$ . This resulted in the rate of the  ${}^3F_4 \rightarrow {}^3F_2$  upconversion being much larger than the radiative decay rate of the  ${}^3F_4$  level, thus making upconversion the dominant depopulation mechanism.<sup>9, 90</sup> The remarkable efficiency of the  $Yb^{3+}({}^2F_{5/2})$ -to- $Tm^{3+}({}^3F_4)$  energy-transfer at high  $Yb^{3+}$  concentrations was previously highlighted by several authors.

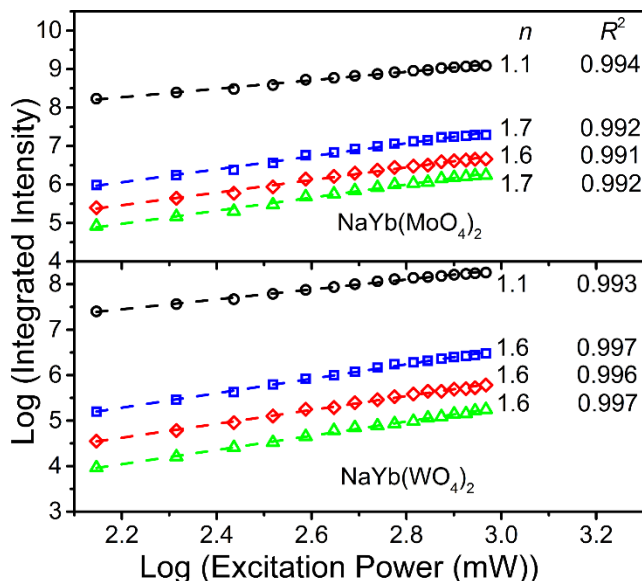


**Figure 4.5.** Double logarithmic plot showing the power dependence of the integrated intensities of the NIR (O, 795 nm), blue (□, 475 nm), green (△, 525 nm), and red (◇, 650 nm) emission bands of  $NaYb(MoO_4)_2$  and  $NaYb(WO_4)_2$  under 973 nm excitation. Linear fits are shown as dashed lines; the corresponding slopes ( $n$ ) and fit residuals ( $R^2$ ) are given. Note the linear dependence of the NIR upconversion emission in the entire power range.



Suyver et al. investigated energy-transfer processes in bulk NaYF<sub>4</sub> codoped with 0.3 and 25 mol. % of Tm<sup>3+</sup> and Yb<sup>3+</sup>, respectively, and showed that 35% of the absorbed NIR photons are upconverted and re-emitted via the <sup>3</sup>H<sub>4</sub> → <sup>3</sup>H<sub>6</sub> transition.<sup>34</sup> Johnson and coworkers observed saturation of the NIR-to-NIR upconversion in bulk BaYF<sub>5</sub> codoped with 0.1 and 49.9 mol. % of Tm<sup>3+</sup> and Yb<sup>3+</sup>, respectively. Vetrone et al. reported a similar observation in ~17 nm BaYF<sub>5</sub> nanocrystals codoped with 0.5 and 15 mol. % of Tm<sup>3+</sup> and Yb<sup>3+</sup>, respectively.<sup>9</sup> Finally, Stecher et al. observed a linear dependence of the intensity of the NIR emission on excitation power in sub-10 nm LaF<sub>3</sub> nanocrystals codoped with 0.5 and 20 mol. % of Tm<sup>3+</sup> and Yb<sup>3+</sup>, respectively; this occurred at excitation densities as low as 2.5 W cm<sup>-2</sup>.<sup>91</sup> Mita and coworkers demonstrated these observations can be rationalized by considering the dependence of the Yb<sup>3+</sup>-to-Tm<sup>3+</sup> energy-transfer coefficient on the Yb<sup>3+</sup> concentration.<sup>92</sup> In a combined theoretical and experimental study that employed bulk BaY<sub>2</sub>F<sub>8</sub> and YF<sub>3</sub> codoped with Yb<sup>3+</sup> and Tm<sup>3+</sup>, they showed that the Yb<sup>3+</sup>-to-Tm<sup>3+</sup> energy-transfer coefficient saturates upon increasing the Yb<sup>3+</sup> concentration above 10 mol. %. The linear dependence of the emission intensity on excitation power implies that the highest possible efficiencies for upconversion via energy-transfer have been achieved for a given chemical composition of the phosphor. In the case of the double molybdates and tungstates studied in this work, kinetically limited sensitizer-to-activator energy-transfer was observed in hosts featuring concentrations of ~100 mol. % of the sensitizer (Yb<sup>3+</sup>) and ~10<sup>-4</sup> mol. % of the activator (Tm<sup>3+</sup>). Therefore, kinetically limited energy-transfer occurred at Yb<sup>3+</sup> and Tm<sup>3+</sup> concentrations that were almost an order of magnitude higher and three orders of magnitude lower, respectively, than those typically encountered in upconverting phosphors codoped with Yb<sup>3+</sup> and Tm<sup>3+</sup> (vide supra). This finding prompts for an expansion of the library of upconverting metalates through the use of the sensitizer and activator concentrations as compositional levers to tune the kinetics of energy-

transfer processes relevant to light absorption and emission. Target compositions should include metalates featuring sensitizer (i.e.,  $\text{Yb}^{3+}$ ) concentrations near unity and trace concentrations of the activator ions (i.e.,  $\text{Tm}^{3+}$ ,  $\text{Er}^{3+}$ ).

Regarding the chemical units responsible for the bright blue emission ( $\sim 475$  nm), two alternatives were considered: sensitized upconversion via three-photon energy-transfer from  $\text{Yb}^{3+}$  to  $\text{Tm}^{3+}$  and cooperative luminescence by a pair of neighboring  $\text{Yb}^{3+}$  ions. As expected, discriminating between these two alternatives was not exempt from ambiguity.<sup>93</sup>  $\text{Tm}^{3+}$  is a well-known blue emitter due to its  $^1G_4 \rightarrow ^3H_6$  transition ( $\sim 480$  nm). When coupled to  $\text{Yb}^{3+}$  the  $^1G_4$  level gets populated via a three-photon energy-transfer process ( $^3H_6 \xrightarrow{h\nu} ^3H_5 \rightarrow ^3F_4 \xrightarrow{h\nu} ^3F_2 \rightarrow ^3H_4 \xrightarrow{h\nu} ^1G_4$ , see **Figure 4.5**). However, slopes of 1.7 and 1.6 were obtained for the blue band observed in the spectra of  $\text{NaYb}(\text{MoO}_4)_2$  and  $\text{NaYb}(\text{WO}_4)_2$ , respectively. This finding suggested that the blue emission resulted from a two-photon process, rather than a three-photon one. More importantly, the process giving rise to this band  $\sim 475$  nm did not show a linear dependence on the excitation power, unlike the NIR emission band centered at  $\sim 795$  nm. The latter was conclusively assigned to emission from  $\text{Tm}^{3+}$  and its linear power-dependence demonstrated that the entire power range employed corresponds to the high-power regime for this ion (i.e., where upconversion to a higher-lying energy state is the dominant depopulation mechanism). Suyver et al. showed that in this regime the intensity of any emission band of  $\text{Tm}^{3+}$  must exhibit a linear dependence on the excitation power.<sup>94</sup> Therefore, the fact that the band at  $\sim 475$  nm did not have a linear dependence on the excitation power indicates that it did not result from radiative relaxation of  $\text{Tm}^{3+}$  after energy-transfer from  $\text{Yb}^{3+}$ . Thus, we turned our attention to the alternative chemical units that could give rise to the band at  $\sim 475$  nm; that is, to

Yb<sup>3+</sup>–Yb<sup>3+</sup> dimers. The principle of cooperative photoluminescence by Yb<sup>3+</sup>–Yb<sup>3+</sup> dimers is depicted in **Figure 4.5**. It can be described as a two-photon process in which a pair of neighboring Yb<sup>3+</sup> ions excited each by a NIR photon simultaneously decays by emitting a blue photon at nearly twice the excitation energy (i.e.,  $2 \text{ Yb}^{3+}(^2F_{7/2}) \xrightarrow{2h\nu} 2 \text{ Yb}^{3+}(^2F_{5/2}) \rightarrow 2 \text{ Yb}^{3+}(^2F_{7/2}) + h\nu'$ ;  $\nu' = 2\nu$ ).<sup>79</sup> As mentioned earlier, the intensity of the blue emission observed in polycrystalline NaYb(MoO<sub>4</sub>)<sub>2</sub> and NaYb(WO<sub>4</sub>)<sub>2</sub> has a nearly quadratic dependence on the excitation power, consistent with a two-photon process. The efficiency of cooperative luminescence is ~4–5 orders of magnitude lower than that of sensitized upconversion luminescence; as a consequence, emission bands resulting from the former display much weaker intensity.<sup>93, 95</sup> The relative intensities of the bands at ~475 and ~795 nm observed in the emission spectra of NaYb(MoO<sub>4</sub>)<sub>2</sub> and NaYb(WO<sub>4</sub>)<sub>2</sub> were consistent with that expectation. Cooperative blue emission by Yb<sup>3+</sup>–Yb<sup>3+</sup> dimers under ~980 nm excitation was first observed by Nakazawa and Shionoya in YbPO<sub>4</sub>.<sup>79</sup> Later on, it was observed in glasses<sup>86-88, 95-97</sup> and crystalline solids containing Yb<sup>3+</sup> clusters.<sup>43</sup> Cooperative luminescence is experimentally observed in cases where these clusters feature Yb<sup>3+</sup>–Yb<sup>3+</sup> interatomic distances shorter than 6 Å.<sup>43, 86, 93</sup> From a structural standpoint, local clustering of Yb<sup>3+</sup> ions to create Yb<sup>3+</sup>–Yb<sup>3+</sup> dimers in NaYb(MoO<sub>4</sub>)<sub>2</sub> and NaYb(WO<sub>4</sub>)<sub>2</sub> is possible due to the intrinsic disorder of Na<sup>+</sup> and Yb<sup>3+</sup> over the same crystallographic site. Arakcheeva et al. showed that Eu<sup>3+</sup>–Eu<sup>3+</sup> dimers are indeed present in an analogous system such as Na<sub>x</sub>Eu<sub>(2-x)/3</sub>MoO<sub>4</sub> (0 ≤ x ≤ 0.5).<sup>78</sup> Further, the shortest distance between two adjacent Yb<sup>3+</sup> ions in the NaYb(MoO<sub>4</sub>)<sub>2</sub> and NaYb(WO<sub>4</sub>)<sub>2</sub> unit cells is ~3.81 Å. This distance is within the range typically required to observe cooperative blue luminescence from Yb<sup>3+</sup>–Yb<sup>3+</sup> dimers. Therefore, the presence of Yb<sup>3+</sup>–Yb<sup>3+</sup>

dimers that can interact cooperatively under NIR excitation is feasible. Altogether, the quadratic power-dependence of the intensity of the blue emission, the intrinsic  $\text{Na}^+/\text{Yb}^{3+}$  substitutional disorder, and the  $\text{Yb}^{3+}-\text{Yb}^{3+}$  interatomic distances, gave support to the hypothesis that local clustering of  $\text{Yb}^{3+}$  ions in  $\text{NaYb}(\text{MoO}_4)_2$  and  $\text{NaYb}(\text{WO}_4)_2$  results in  $\text{Yb}^{3+}-\text{Yb}^{3+}$  dimers that interact in a cooperative fashion under NIR excitation. Finally, it should be noted that the fine structure of the blue emission band consisted of two peaks at 473 and 477 nm, indicating that the coupled levels were located at 21141 and 20964  $\text{cm}^{-1}$ , respectively. These estimates are in excellent agreement with those derived from the absorption and cooperative luminescence spectra of  $\text{Yb}^{3+}$ -doped  $\text{LiLa}(\text{WO}_4)_2$ , for which coupled states at 20957 and 20641  $\text{cm}^{-1}$  were observed.<sup>61</sup>  $\text{LiLa}(\text{WO}_4)_2$  is isostructural and its unit cell is isometric ( $a = 5.23$ ,  $c = 11.34$  Å) with that of  $\text{NaYb}(\text{MoO}_4)_2$  and  $\text{NaYb}(\text{WO}_4)_2$ .

The hypothesis of cooperative blue luminescence by  $\text{Yb}^{3+}-\text{Yb}^{3+}$  dimers was further supported by probing the decay time of the blue emission at 475 nm and comparing it to that of a single  $\text{Yb}^{3+}$  ion at  $\sim 1000$  nm. One of the signatures of cooperative luminescence is that the emission from the  $\text{Yb}^{3+}-\text{Yb}^{3+}$  dimer should decay twice as fast as that of a single  $\text{Yb}^{3+}$  ion.<sup>79</sup> The downconversion emission spectra of  $\text{NaYb}(\text{MoO}_4)_2$  and  $\text{NaYb}(\text{WO}_4)_2$  under excitation with 973 nm radiation exhibited a broad band centered  $\sim 1000$  nm (see **Figure 4.6**). This emission band resulted from the decay of the  $^2F_{5/2}$  manifold of  $\text{Yb}^{3+}$  into the four-fold degenerate  $^2F_{7/2}$  manifold. The time evolution of the blue (upconverted) and NIR (downconverted) emissions under 973 nm excitation (650 mW) was monitored at 475 and 1003 nm, respectively. Decay curves are shown in **Figure 4.7** for both  $\text{NaYb}(\text{MoO}_4)_2$  and  $\text{NaYb}(\text{WO}_4)_2$ . Decays were adequately fit with a monoexponential function and the corresponding lifetimes ( $\tau$ ) were extracted. Lifetimes of 113 and 248  $\mu\text{s}$  were estimated for the 475 and 1003 nm

emissions in  $\text{NaYb}(\text{MoO}_4)_2$ , respectively. Very similar estimates were obtained in the case of  $\text{NaYb}(\text{WO}_4)_2$ ; these were 127 and 255  $\mu\text{s}$  for the 475 and 1003 nm emissions, respectively. More importantly, the decay of the blue emission in both hosts occurred nearly twice as fast as that of the NIR emission from a single  $\text{Yb}^{3+}$  ion. This finding was in good agreement with the quadratic power-dependence of the intensity of the blue emission, and gave further support to the hypothesis that local clustering of  $\text{Yb}^{3+}$  ions in these hosts resulted in cooperative luminescence from  $\text{Yb}^{3+}\text{-Yb}^{3+}$  dimers.

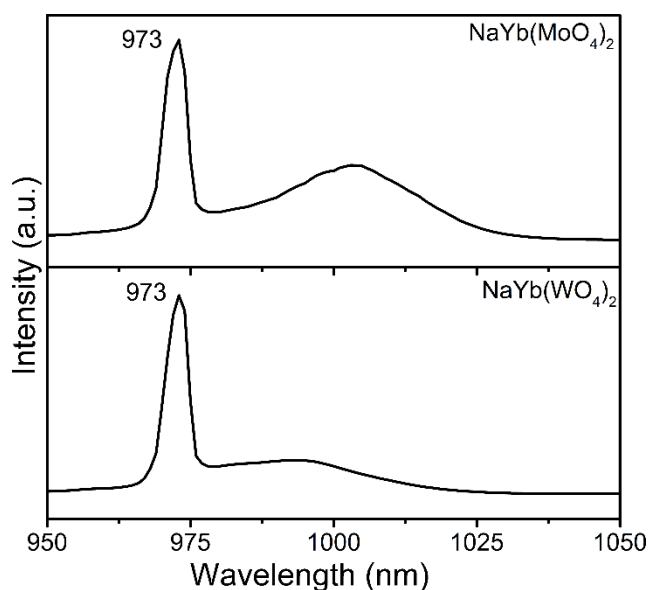


**Figure 4.6.** Downconversion luminescence spectra of  $\text{NaYb}(\text{MoO}_4)_2$  and  $\text{NaYb}(\text{WO}_4)_2$  under 973 nm excitation (650 mW).

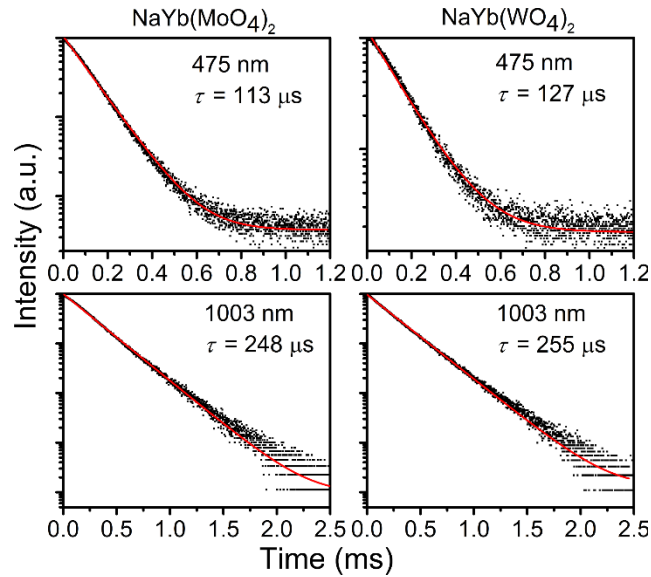


**Figure 4.7.** Decay curves of the 475 and 1003 nm emissions of  $\text{NaYb}(\text{MoO}_4)_2$  (left panels) and  $\text{NaYb}(\text{WO}_4)_2$  (right panels) under 973 nm excitation (650 mW). Monoexponential fits are depicted as solid red lines; the corresponding lifetimes  $\tau$  are given.

#### 4.4. Conclusions

In summary, energy-transfer processes responsible for NIR-to-NIR and NIR-to-blue light upconversion in polycrystalline  $\text{NaYb}(\text{MoO}_4)_2$  and  $\text{NaYb}(\text{WO}_4)_2$  were investigated using a combination of steady-state and time-dependent spectrofluorometry, elemental analysis, and Rietveld analysis of X-ray diffraction data. The strong NIR emission at  $\sim 795$  nm was assigned to the  ${}^3H_4 \rightarrow {}^3H_6$  transition of  $\text{Tm}^{3+}$ , which was found to be present at the trace level in both hosts ( $\sim 1$  ppm). Owing to the high efficiency of the energy-transfer from the  ${}^2F_{5/2}$  manifold of  $\text{Yb}^{3+}$  to the  ${}^3F_4$  level of  $\text{Tm}^{3+}$ , the intensity of the NIR emission exhibited a linear dependence on excitation power throughout the entire power range. Two distinct chemical units were discussed as the possible origin of the bright blue emission at  $\sim 475$  nm:  $\text{Tm}^{3+}$  (via three-photon energy-transfer from  $\text{Yb}^{3+}$ ) and  $\text{Yb}^{3+}\text{-Yb}^{3+}$  dimers (via cooperative luminescence). Cooperative luminescence by  $\text{Yb}^{3+}\text{-Yb}^{3+}$  dimers was favored by three facts: (i) the emission intensity did not exhibit the linear dependence on the excitation power observed for the radiative

${}^3H_4 \rightarrow {}^3H_6$  NIR transition of  $Tm^{3+}$ ; (ii) the quadratic dependence of the emission intensity on the excitation power; and (iii) the decay of the blue emission, which occurred nearly twice as fast as that of the NIR emission from a single  $Yb^{3+}$  ion. From a structural standpoint, the feasibility of having  $Yb^{3+}-Yb^{3+}$  dimers that can interact cooperatively under NIR excitation was supported by (i) the substitutional disorder of  $Na^+$  and  $Yb^{3+}$  over the same crystallographic site, and (ii) the shortest distance between two adjacent  $Yb^{3+}$  ions being within the range required to observe cooperative luminescence.

Findings presented in this work prompt for an expansion of the library of upconverting metalates through the use of the sensitizer and activator concentrations as compositional levers to tune the kinetics of energy-transfer processes relevant to photoluminescence. Metalates featuring sensitizer concentrations near unity and trace concentrations of the activator ions should be the focus of future synthetic and spectroscopic investigations. From a methodological standpoint, results presented in this work demonstrate the utility of  $Yb^{3+}$  as a probe of short-range ordered clusters in systems with intrinsic chemical disorder.

## CHAPTER 5. EUROPIUM-ACTIVATED $\text{NaYb}(\text{MO}_4)_2$ ( $\text{M} = \text{Mo}, \text{W}$ ) AS A DUAL-EMITTER THERMOSENSITIVE PHOSPHOR

### 5.1. Introduction

Temperature-dependent luminescence response of rare-earth activated phosphors has been investigated with the aim of employing them as thermosensitive phosphors.<sup>14, 77</sup> Rare-earth activated scheelite-type phosphors of chemical formula  $\text{NaRE}(\text{MO}_4)_2$  ( $\text{Y}$  and  $\text{RE} =$  rare-earth,  $\text{M} = \text{Mo}, \text{W}$ ) is an interesting class of materials due to the intrinsic disorder of  $\text{Na}^+$  and  $\text{RE}^{3+}$  ions present in the crystal structure. Also, rare-earth ion being a stoichiometric component in the composition of  $\text{NaRE}(\text{MO}_4)_2$  allows incorporation of activator ions such as  $\text{Dy}^{3+}$ ,  $\text{Eu}^{3+}$ , and  $\text{Ho}^{3+}$  whose photoluminescence emission exhibit distinct changes with temperature.<sup>53</sup> However, thermometric sensitivity of single-emitter thermosensitive phosphors featuring abovementioned activator ions decreases with temperature due to thermal quenching.<sup>99-100</sup> Chemical composition of phosphor can be used as a lever to manipulate the temperature-dependent luminescence response and mitigate the effect of thermal quenching on thermometric sensitivity. As a strategy to manipulate the temperature-dependent luminescence response, two emitters that show different thermal quenching characteristics are employed.<sup>48</sup> According to the findings of the investigations on photoluminescence properties of stoichiometric  $\text{NaYb}(\text{MO}_4)_2$  (see **Chapter 4**),  $\text{Yb}^{3+}$ - $\text{Yb}^{3+}$  dimers present in these systems have the potential to perform as blue emitters. Further,  $\text{Yb}^{3+}$ - $\text{Yb}^{3+}$  dimers to  $\text{Eu}^{3+}$  energy-transfer, which leads to a red emission from  $\text{Eu}^{3+}$  under 973 nm excitation has been reported.<sup>101-103</sup> However, blue cooperative luminescence from  $\text{Yb}^{3+}$ - $\text{Yb}^{3+}$  dimers has not been employed for optical temperature sensing. Importantly, reports on employing blue cooperative luminescence coupled with emission of another rare-earth emitter for temperature sensing are absent. Herein, two  $\text{Eu}^{3+}$ -activated  $\text{NaYb}(\text{MO}_4)_2$  phosphors that utilize simultaneous



photoluminescence emission from  $\text{Yb}^{3+}\text{-Yb}^{3+}$  dimers and  $\text{Eu}^{3+}$  activators are investigated. The intrinsic disorder in the crystal structure of  $\text{NaRE}(\text{MO}_4)_2$  and  $\text{Yb}^{3+}\text{-to-Eu}^{3+}$  ratio were employed as levers to tune the luminescence response of the phosphor. In this system, energy-transfer from  $\text{Yb}^{3+}\text{-Yb}^{3+}$  dimers to  $\text{Eu}^{3+}$  can be controlled using the distance between the emitter and the acceptor ions.<sup>104</sup> Energy-transfer from  $\text{Yb}^{3+}\text{-Yb}^{3+}$  dimers to  $\text{Eu}^{3+}$  activators take place when  $\text{Eu}^{3+}$  ions are in the vicinity of  $\text{Yb}^{3+}\text{-Yb}^{3+}$  dimers.<sup>103, 105</sup> On the other hand, high  $\text{Eu}^{3+}$  concentrations could prevent the formation of  $\text{Yb}^{3+}\text{-Yb}^{3+}$  dimers, which reduces the luminescence intensity of the blue emission. Therefore, in this investigation,  $\text{Yb}^{3+}\text{-to-Eu}^{3+}$  ratio was tuned to obtain comparable emission intensities for both blue and red bands. Thermometric response of both phosphors is evaluated. The potential of employing  $\text{Eu}^{3+}$ -activated  $\text{NaYb}(\text{MO}_4)_2$  phosphors for temperature sensing is discussed. Moreover, the advantage of employing two emitters to mitigate the effect of thermal quenching on thermometric sensitivity is highlighted. Finally, thermometric performance of the two phosphors under investigation are compared with other reported dual-emitter thermosensitive phosphors.

## 5.2. Experimental

### 5.2.1. Solid-State Synthesis of $\text{NaYb}_{0.95}\text{Eu}_{0.05}(\text{MoO}_4)_2$ and $\text{NaYb}_{0.95}\text{Eu}_{0.05}(\text{WO}_4)_2$

Conventional solid-state reaction was employed to synthesize polycrystalline  $\text{NaYb}_{0.95}\text{Eu}_{0.05}(\text{MoO}_4)_2$  and  $\text{NaYb}_{0.95}\text{Eu}_{0.05}(\text{WO}_4)_2$ . Stoichiometric amounts of  $\text{Na}_2\text{CO}_3$  (99.999 %, Sigma-Aldrich),  $\text{Yb}_2\text{O}_3$  (99.99 %, Sigma-Aldrich),  $\text{Eu}_2\text{O}_3$  (99.99%, Sigma-Aldrich),  $\text{WO}_3$  (99.995 %, Sigma-Aldrich) and  $\text{MoO}_3$  (99.999 %, Acros Organics) were mixed with small amount of acetone and ground in an agate mortar for ~20 min. The unreacted homogeneous powder mixtures were heated under the optimized synthesis conditions mentioned in **section 2.2.1.1**.

### 5.2.2. Powder X-ray Diffraction (XRD)

Powder XRD patterns were collected using a Bruker D2 Phaser diffractometer operated at 30 kV and 10 mA. Diffractograms were collected in the 10–80°  $2\theta$  range using a step size of 0.0125° and a step time of 1.25 s. Diffraction patterns were recorded at room temperature.

### 5.2.3. Rietveld Analysis

Rietveld refinements of powder XRD patterns were performed using the General Structure Analysis System (GSAS) with the graphical user interphase (EXPGUI) software<sup>106</sup> as mentioned in **section 2.2.2.3**. Fractional atomic coordinates of the oxygen atoms ( $x_O$ ,  $y_O$ ,  $z_O$ ) and an isotropic displacement parameter for all metal atoms in the structure ( $U_{iso}^M$ ) were refined. The isotropic displacement parameter for the oxygen atom ( $U_{iso}^O$ ) was constrained according to  $U_{iso}^O = 1.5 \times U_{iso}^M$ . The occupancies of the rare-earth containing  $4b$  site was fixed according to the nominal Na:Yb:Eu molar ratio of 0.5:[0.5 × (1 –  $x$ ):[0.5 ×  $x$ ]]. Residual  $R_{wp}$  values and visual inspection of the difference curves of the Rietveld fits were employed to assess the quality of the refined structural models.

### 5.2.4. Variable-Temperature Upconversion Spectrofluorometry

Spectrofluorometric analyses were carried out using a Fluorolog 3–222 fluorometer (Horiba Scientific), and the methods reported in **section 2.2.2.6** was followed. The emission spectra were collected in the 100–500 and 100–700 K temperature range at 25 K intervals for NaYb<sub>0.95</sub>Eu<sub>0.05</sub>(MoO<sub>4</sub>)<sub>2</sub> and NaYb<sub>0.95</sub>Eu<sub>0.05</sub>(WO<sub>4</sub>)<sub>2</sub>, respectively.

### 5.3. Results and Discussion

#### 5.3.1. Structural Characterization of $\text{NaYb}_{0.95}\text{Eu}_{0.05}(\text{MO}_4)_2$

Rietveld analysis of powder XRD data of  $\text{NaYb}_{0.95}\text{Eu}_{0.05}(\text{MoO}_4)_2$  and  $\text{NaYb}_{0.95}\text{Eu}_{0.05}(\text{WO}_4)_2$  was performed to probe their phase-purity. Fits of the scheelite-type tetragonal structure to the experimental patterns are shown in **Figures 5.1a** and **5.1b**, respectively. The structural parameters extracted from the Rietveld refinements are provided in **Table 5.1**. As evident from the difference curves of the fits, the agreement between the calculated and the experimental XRD patterns was adequate. All the diffraction maxima were indexed to corresponding molybdate or tungstate phase. No extra peaks corresponding to a secondary crystalline phase was observed, confirming the phase-purity of the phosphors.

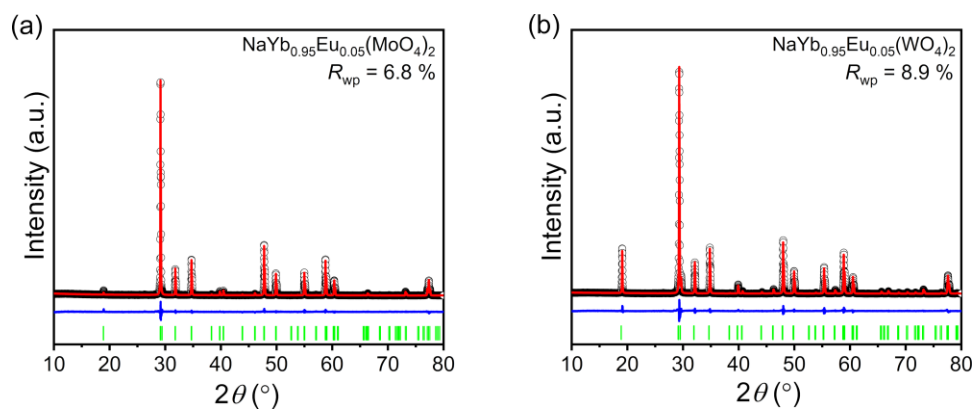


**Figure 5.1.** Rietveld analysis of the PXRD patterns of (a)  $\text{NaYb}_{0.95}\text{Eu}_{0.05}(\text{MoO}_4)_2$  and (b)  $\text{NaYb}_{0.95}\text{Eu}_{0.05}(\text{WO}_4)_2$ . Experimental ( $\circ$ ) and calculated ( $—$ ) patterns are shown along with the difference curve ( $—$ ). Tick marks ( $|$ ) correspond to the calculated positions of the diffraction maxima.

**Table 5.1.** Structural Parameters of NaYb<sub>0.95</sub>Eu<sub>0.05</sub>(MoO<sub>4</sub>)<sub>2</sub> and NaYb<sub>0.95</sub>Eu<sub>0.05</sub>(WO<sub>4</sub>)<sub>2</sub>

	NaYb <sub>0.95</sub> Eu <sub>0.05</sub> (MoO <sub>4</sub> ) <sub>2</sub>	NaYb <sub>0.95</sub> Eu <sub>0.05</sub> (WO <sub>4</sub> ) <sub>2</sub>
<i>a</i> (Å)	5.17218(3)	5.17782(4)
<i>c</i> (Å)	11.26383(8)	11.20658(11)
<i>V</i> (Å <sup>3</sup> )	301.324(5)	300.447(6)
<i>x</i> <sub>0</sub>	0.1543(7)	0.7316(9)
<i>y</i> <sub>0</sub>	0.0258(8)	0.5940(11)
<i>z</i> <sub>0</sub>	0.2065(3)	0.0417(5)
<i>U</i> <sub>iso</sub> <sup>M</sup> (Å <sup>2</sup> ) <sup>a</sup>	1.05(3)	1.25(3)
<i>U</i> <sub>iso</sub> <sup>O</sup> (Å <sup>2</sup> ) <sup>a</sup>	1.57(4)	1.42(5)
<i>R</i> <sub>wp</sub>	6.8	8.9

<sup>a</sup> Given as 100 × *U*.

### 5.3.2. Temperature-Dependent Photoluminescence

The temperature-dependent photoluminescence response of NaYb<sub>0.95</sub>Eu<sub>0.05</sub>(MoO<sub>4</sub>)<sub>2</sub> and NaYb<sub>0.95</sub>Eu<sub>0.05</sub>(WO<sub>4</sub>)<sub>2</sub> under 973 nm excitation was investigated using steady-state spectrofluorometry. The emission spectra of NaYb<sub>0.95</sub>Eu<sub>0.05</sub>(MoO<sub>4</sub>)<sub>2</sub> and NaYb<sub>0.95</sub>Eu<sub>0.05</sub>(WO<sub>4</sub>)<sub>2</sub> were collected in 100–500 and 100–600 K temperature ranges and are shown in **Figures 5.2a and 5.2b**, respectively. Low signal-to-noise ratio prevented collecting meaningful emission spectra for NaYb<sub>0.95</sub>Eu<sub>0.05</sub>(MoO<sub>4</sub>)<sub>2</sub> and NaYb<sub>0.95</sub>Eu<sub>0.05</sub>(WO<sub>4</sub>) at temperatures above 500 and 600 K, respectively. Temperature-dependent emission spectra of both phosphors are dominated by two bands: blue and red emission bands centering at ~21065 (~474 nm) and ~16260 cm<sup>-1</sup> (~615 nm), respectively. The structural and chemical bases related to the origin of the blue emission observed in Yb<sup>3+</sup>-rich scheelite-type molybdate and tungstate compounds have previously been reported and discussed in detail in **Chapter 4**.<sup>49</sup> Based on that, the emission band centered at ~21065 cm<sup>-1</sup> was assigned to the cooperative blue emission from Yb<sup>3+</sup>–Yb<sup>3+</sup> dimers under 973 nm (10204.08 cm<sup>-1</sup>) excitation without ambiguity. The intraconfigurational *f*–*f* transition (<sup>5</sup>*D*<sub>0</sub> → <sup>7</sup>*F*<sub>2</sub>) of Eu<sup>3+</sup> was

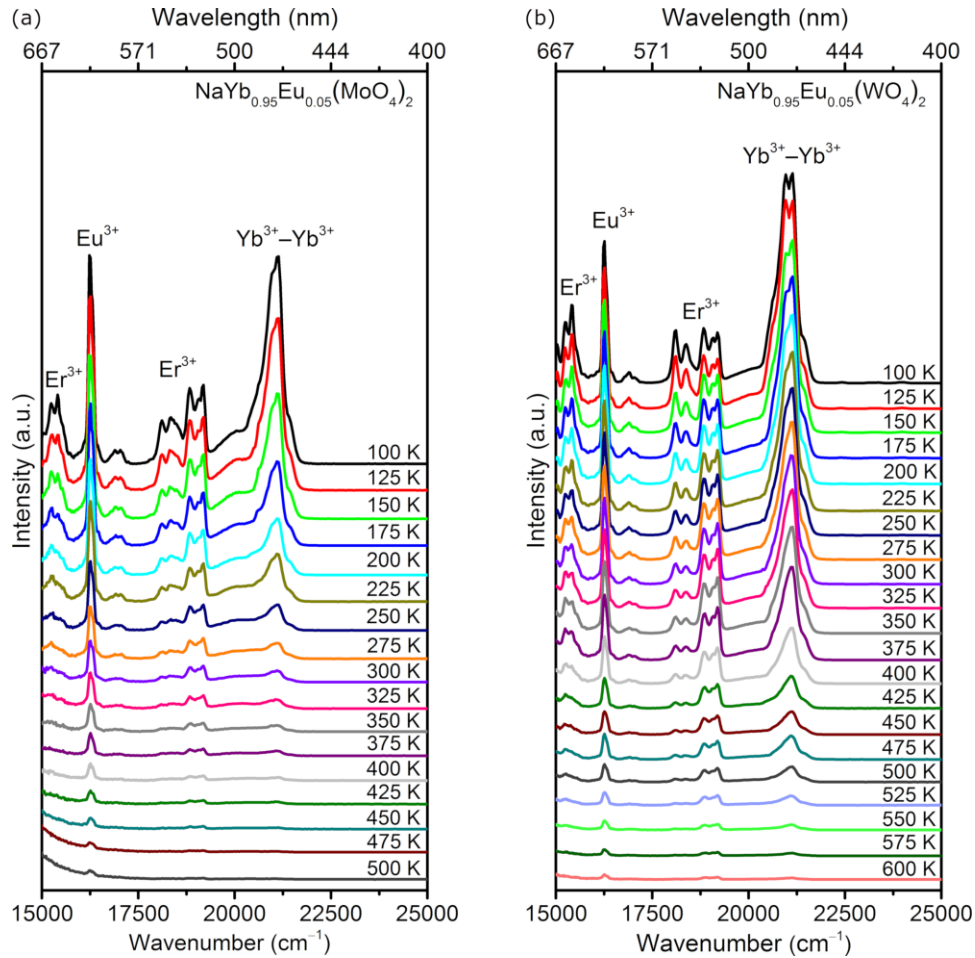


**Figure 5.2.** Temperature-dependent emission spectra of (a)  $\text{NaYb}_{0.95}\text{Eu}_{0.05}(\text{MoO}_4)_2$  and (b)  $\text{NaYb}_{0.95}\text{Eu}_{0.05}(\text{WO}_4)_2$  collected under 973 nm excitation. Spectra for  $\text{NaYb}_{0.95}\text{Eu}_{0.05}(\text{MoO}_4)_2$  and  $\text{NaYb}_{0.95}\text{Eu}_{0.05}(\text{WO}_4)_2$  were recorded in 100–500 and 100–600 K temperature range, respectively. The blue emission band centered at  $\sim 21065 \text{ cm}^{-1}$  ( $\sim 474 \text{ nm}$ ) originate from the cooperative emission of  $\text{Yb}^{3+}-\text{Yb}^{3+}$  dimers. The red emission band centered at  $16260 \text{ cm}^{-1}$  ( $\sim 615 \text{ nm}$ ) is due to the intraconfigurational f–f transition of  $\text{Eu}^{3+}$ . Weak bands in the green (at  $\sim 19000$  and  $18350 \text{ cm}^{-1}$ ) and red ( $\sim 15350 \text{ cm}^{-1}$ ) regions are due to the two-photon upconversion from  $\text{Er}^{3+}$  impurities.

identified as the origin of the red band resulted from  $\text{Yb}^{3+}$ -sensitized upconversion of  $\text{Eu}^{3+}$ . In addition to the blue and red emission bands originated from  $\text{Yb}^{3+}-\text{Yb}^{3+}$  dimers and  $\text{Eu}^{3+}$ , weak bands in the green ( $\sim 19000$  and  $18350 \text{ cm}^{-1}$ ) and red ( $\sim 15350 \text{ cm}^{-1}$ ) regions of the emission spectra were observed. These bands were assigned to the green ( ${}^2H_{11/2}, {}^4S_{3/2} \rightarrow {}^4I_{15/2}$ ) and red ( ${}^4F_{9/2} \rightarrow$

$^4I_{15/2}$ ) emission due to the well-known two-photon upconversion from  $\text{Yb}^{3+}$ -sensitized  $\text{Er}^{3+}$ , which is found to be present at trace levels ( $\sim 1$  ppm) in  $\text{Yb}^{3+}$ -rich phosphors.<sup>96</sup> Blue and red emission bands are of interest in this investigation. Therefore, temperature-dependent response of these two bands was investigated with an eye towards employing them for optical temperature sensing. Inspection of the temperature-dependent emission spectra recorded for  $\text{NaYb}_{0.95}\text{Eu}_{0.05}(\text{MoO}_4)_2$  and  $\text{NaYb}_{0.95}\text{Eu}_{0.05}(\text{WO}_4)_2$  revealed that the intensity of both blue and the red emissions decreased with temperature. However, the blue emission band resulted from the cooperative interaction of  $\text{Yb}^{3+}$ - $\text{Yb}^{3+}$  dimers is more sensitive to temperature than the red emission of  $\text{Eu}^{3+}$  ( $^5D_0 \rightarrow ^7F_2$ ). This was expected as the efficiency of the cooperative luminescence of  $\text{Yb}^{3+}$ - $\text{Yb}^{3+}$  dimers are  $\sim 3$ – $5$  orders of magnitude lower than that of  $\text{Yb}^{3+}$ -sensitized upconversion processes.<sup>93</sup> Further, the difference in temperature-dependent responses of these two bands was quantitatively analyzed by computing the quenching temperatures. The quenching temperature ( $T_Q$ ) is defined as the temperature at which the intensity of a photoluminescence emission becomes half of its initial emission magnitude lower than that of  $\text{Yb}^{3+}$ -sensitized upconversion processes.<sup>107</sup> Further, the difference in temperature-dependent responses of these two bands was quantitatively analyzed by computing the quenching temperatures. The quenching temperature ( $T_Q$ ) is defined as the temperature at which the intensity of a photoluminescence emission becomes half of its initial emission intensity. **Figures 5.3a** and **5.3b** display the integrated intensities of blue and red emission bands of  $\text{NaYb}_{0.95}\text{Eu}_{0.05}(\text{MoO}_4)_2$  and  $\text{NaYb}_{0.95}\text{Eu}_{0.05}(\text{WO}_4)_2$  as a function of temperature, respectively. Insets show the digital pictures of  $\text{NaYb}_{0.95}\text{Eu}_{0.05}(\text{MoO}_4)_2$  (at 100 and 500 K) and  $\text{NaYb}_{0.95}\text{Eu}_{0.05}(\text{WO}_4)_2$  (at 100 and 600 K) phosphors luminescing under 973 nm excitation. In  $\text{NaYb}_{0.95}\text{Eu}_{0.05}(\text{MoO}_4)_2$ ,  $T_Q$  values computed for blue and red bands were 162 and 225 K, respectively. In the case of  $\text{NaYb}_{0.95}\text{Eu}_{0.05}(\text{WO}_4)_2$ , these values were 331 and 370 K, respectively.

In both cases,  $T_Q$  values obtained for red bands were larger than that of blue bands, confirming cooperative blue emission from  $\text{Yb}^{3+}\text{-Yb}^{3+}$  dimers is more susceptible to thermal quenching than the red emission from  $\text{Eu}^{3+}$ . Despite the compositional and structural similarities of these two phosphors,  $T_Q$  values computed for blue and red bands of  $\text{NaYb}_{0.95}\text{Eu}_{0.05}(\text{WO}_4)_2$  were higher than the corresponding values obtained for  $\text{NaYb}_{0.95}\text{Eu}_{0.05}(\text{MoO}_4)_2$ . This suggests that energy-transfer processes related to the thermal quenching of blue and red emissions are host-dependent. Interestingly, different thermal quenching properties of blue and red emissions lead to a temperature-driven color change of the photoluminescence emission. As depicted in the insets of **Figures 5.3a** and **5.3b**, the color of the photoluminescence emission of both phosphors changed from blue to red with temperature. In  $\text{NaYb}_{0.95}\text{Eu}_{0.05}(\text{MoO}_4)_2$  ( $\text{NaYb}_{0.95}\text{Eu}_{0.05}(\text{WO}_4)_2$ ), this color change was witnessed as the temperature of the phosphor increased from 100 to 500 K (600 K), respectively. Power-dependent studies were employed to understand the energy-transfer processes

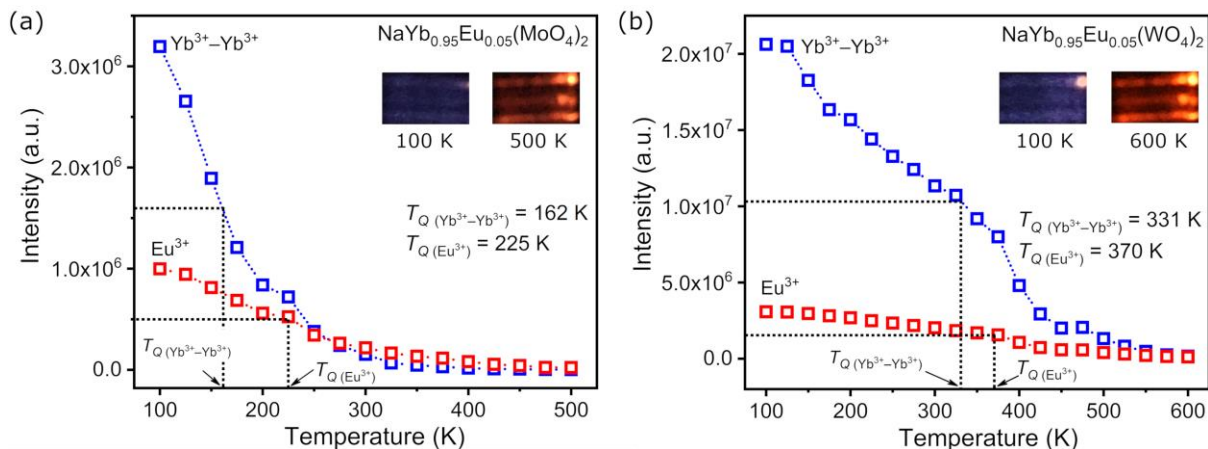


**Figure 5.3.** Integrated intensities of blue and red bands of (a)  $\text{NaYb}_{0.95}\text{Eu}_{0.05}(\text{MoO}_4)_2$  and (b)  $\text{NaYb}_{0.95}\text{Eu}_{0.05}(\text{WO}_4)_2$  as a function of temperature. Quenching temperatures computed for both blue and red bands of  $\text{NaYb}_{0.95}\text{Eu}_{0.05}(\text{MoO}_4)_2$  are lower than the corresponding values computed for  $\text{NaYb}_{0.95}\text{Eu}_{0.05}(\text{WO}_4)_2$ . Digital pictures of the phosphors showing luminescence under 973 nm excitation are shown as the insets.

responsible for blue and red emission in the phosphors under investigation. Double logarithmic plots of the emission intensities of blue and red bands as a function of the excitation power are given in **Figure 5.4**. Slopes of 2.1 and 1.6 were obtained for the linear fits to the blue and red bands, respectively. The quadratic power dependence of both blue and red emission bands suggests that two-photon processes are involved in NIR-to-blue and -red light upconversion observed in these phosphors. Two-photon processes have been reported for NIR-to-blue light upconversion from cooperative luminescence of  $\text{Yb}^{3+}$ - $\text{Yb}^{3+}$  dimers.<sup>49, 108</sup> Further, NIR-to-red upconversion from  $\text{Yb}^{3+}$ -sensitized  $\text{Eu}^{3+}$  have also been investigated as two-photon processes in  $\text{Eu}^{3+}$ -activated  $\text{Yb}^{3+}$ -rich systems such as  $\text{Eu}^{3+}:\text{LiYb}(\text{MoO}_4)_2$ ,<sup>104</sup>  $\text{Eu}:\text{Yb}:\text{Y}_2\text{O}_3$ ,<sup>103</sup>  $\text{Eu}$ -doped oxyfluoride,<sup>105</sup> silica, and tellurite glasses.<sup>96</sup> The energy-transfer processes related to the simultaneous NIR-to-blue and NIR-to-red light upconversion in  $\text{Eu}$ -activated  $\text{NaYb}(\text{MoO}_4)_2$  under 980 nm excitation are summarized in **Figure 5.5**. As discussed in **Chapter 4**,  $\text{Yb}^{3+}$ - $\text{Yb}^{3+}$  dimers were identified as the chemical units responsible for the blue emission observed in  $\text{Yb}^{3+}$ -rich compounds under 973 nm excitation.

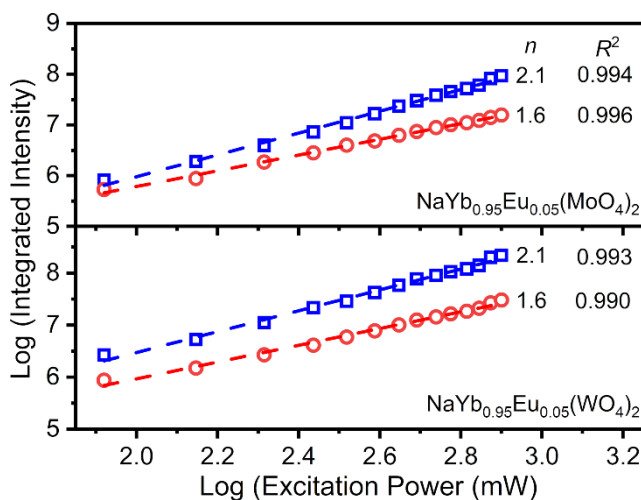


**Figure 5.4.** Double logarithmic plots showing the power dependence of the integrated intensities of the blue ( $21065\text{ cm}^{-1}$ ) and red ( $16260\text{ cm}^{-1}$ ) emission bands of  $\text{NaYb}_{0.95}\text{Eu}_{0.05}(\text{MoO}_4)_2$  and  $\text{NaYb}_{0.95}\text{Eu}_{0.05}(\text{WO}_4)_2$  under 973 nm excitation. Linear fits are shown as dashed lines; the corresponding slopes ( $n$ ) and fit residuals ( $R^2$ ) are given.



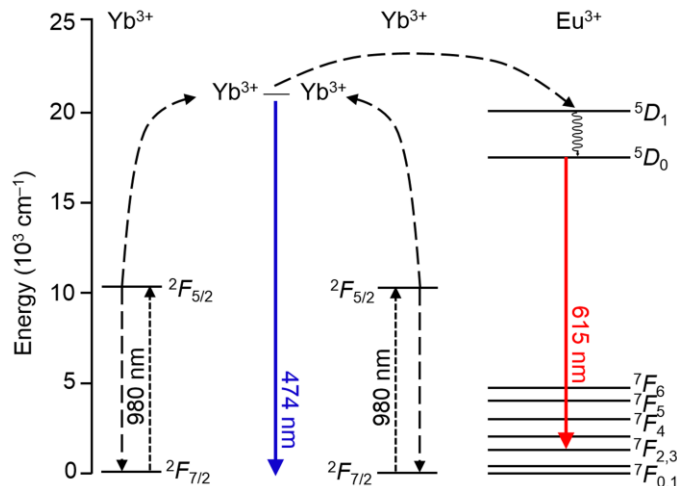


**Figure 5.5.** Dieke diagrams of  $\text{Yb}^{3+}$ ,  $\text{Yb}^{3+}\text{-Yb}^{3+}$  dimers, and  $\text{Eu}^{3+}$ . Non-radiative energy-transfer from  $\text{Yb}^{3+}\text{-Yb}^{3+}$  dimers to neighboring  $\text{Eu}^{3+}$  is depicted with a dashed-arrow. Curly arrows indicate vibrational relaxations. Radiative emission from  $\text{Yb}^{3+}\text{-Yb}^{3+}$  dimers and  $\text{Eu}^{3+}$  are indicated with solid arrows.

The emphasis is placed on understanding the energy-transfer processes related to  $\text{Yb}^{3+}$ -sensitized NIR-to-red light upconversion observed in the phosphors under investigation. The energy-transfer from  $\text{Yb}^{3+}$ -to- $\text{Eu}^{3+}$  can be described as a two-photon cooperative upconversion process in which a pair of neighboring  $\text{Yb}^{3+}$  ions are excited each by a NIR photon, and subsequently transfer that energy to nearby  $\text{Eu}^{3+}$  ions. The energy-transfer from  $\text{Yb}^{3+}\text{-Yb}^{3+}$  dimers to the  $^5D_1$  energy level of  $\text{Eu}^{3+}$  followed by vibrational relaxations populate the  $^5D_0$  energy level. The red emission band centered at  $\sim 16260\text{ cm}^{-1}$  (615 nm) was observed due to  $^5D_0 \rightarrow ^7F_2$  intraconfigurational  $f$ - $f$  transition of  $\text{Eu}^{3+}$ .

Emission spectra were quantitatively analyzed to assess the performance of  $\text{Eu}^{3+}$ -activated  $\text{NaYb}(\text{MO}_4)_2$  as thermosensitive phosphors. To this end, three metrics were computed using the temperature-dependent emission spectra: luminescence intensity ratio  $R(T)$  (equation 5.1), absolute sensitivity ( $S_A$ ) (equation 1.3), and relative sensitivity ( $S_R$ ) (equation 1.4).

$$R(T) = \frac{I_{\text{Red}}(615 \text{ nm})}{I_{\text{Blue}}(474 \text{ nm})} \quad (5.1)$$

Luminescence intensity ratio values were computed using the integrated intensities of blue and red emission bands centered at  $\sim 21065 \text{ cm}^{-1}$  and  $16260 \text{ cm}^{-1}$ , respectively. In all cases, both blue and red bands were fit with two Gaussian curves to obtain the integrated intensities. Luminescence intensity ratio, absolute and relative sensitivities computed for both  $\text{NaYb}_{0.95}\text{Eu}_{0.05}(\text{MoO}_4)_2$  and  $\text{NaYb}_{0.95}\text{Eu}_{0.05}(\text{WO}_4)_2$  were plot as a function of temperature and are shown in **Figures 5.6a–c**, respectively. The luminescence intensity ratios computed for both phosphors increased with temperature. The maximum  $R(T)$  value for  $\text{NaYb}_{0.95}\text{Eu}_{0.05}(\text{MoO}_4)_2$  was observed at 500 K, whereas for  $\text{NaYb}_{0.95}\text{Eu}_{0.05}(\text{WO}_4)_2$ , it was observed at 600 K. Interestingly, the maximum  $R(T)$  value obtained for  $\text{NaYb}_{0.95}\text{Eu}_{0.05}(\text{MoO}_4)_2$  was one order of magnitude larger than what was observed for  $\text{NaYb}_{0.95}\text{Eu}_{0.05}(\text{WO}_4)_2$  ( $\sim 8.4$  vs  $0.7$ ). Local clustering of rare-earth ions is possible in these crystal systems owing to the intrinsic disorder of  $\text{Na}^+$  and rare-earth ions.<sup>49, 71</sup> Changes in temperature-dependent energy-transfer pathways due to the formation of rare-earth clusters could be a possible reason for the differences observed in the luminescence response of phosphors. As shown in **Figure 5.6a**, the experimental  $R(T)$  values were fit with the equation 5.4.

$$R(T) = A \exp\left(-\frac{B}{T}\right) + C \quad (5.4)$$

Here,  $A$ ,  $B$ , and  $C$  are constants,  $T$  is the absolute temperature. Adequate fits were obtained for  $R(T)$  values computed for both  $\text{NaYb}_{0.95}\text{Eu}_{0.05}(\text{MoO}_4)_2$  and  $\text{NaYb}_{0.95}\text{Eu}_{0.05}(\text{WO}_4)_2$ . Inspection of the  $R(T)$  plot of  $\text{NaYb}_{0.95}\text{Eu}_{0.05}(\text{WO}_4)_2$  revealed the luminescence intensity ratios in 100–300 K temperature range exhibited little dependence on temperature. As shown in **Figure 5.3b**,

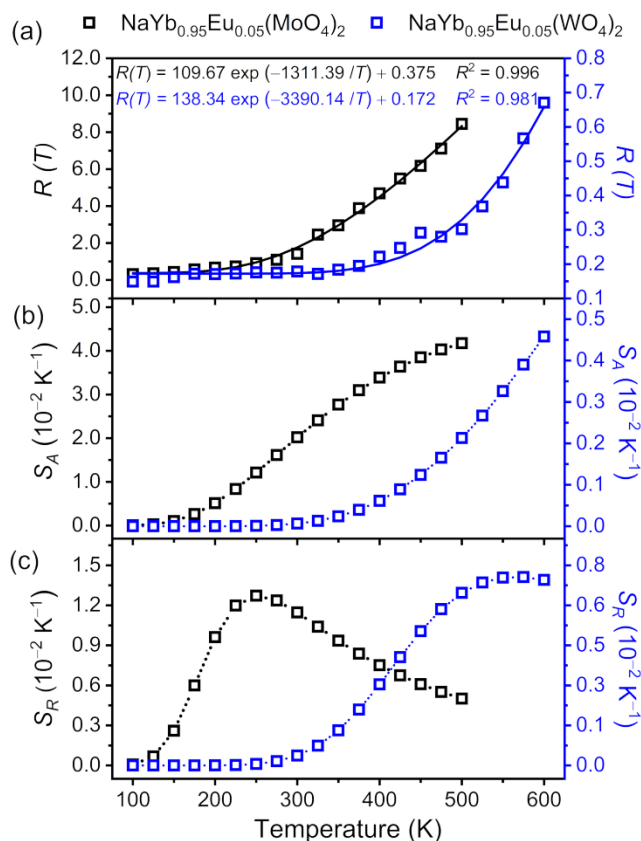


**Figure 5.6.** (a) Luminescence intensity ratio ( $R(T)$ ), (b) absolute sensitivity ( $S_A$ ), and (c) relative sensitivity ( $S_R$ ) of  $\text{NaLa}_{0.95}\text{Eu}_{0.05}(\text{MoO}_4)_2$  and  $\text{NaLa}_{0.95}\text{Eu}_{0.05}(\text{WO}_4)_2$ . Analytical expressions used to fit experimental  $R(T)$  values are given. The corresponding fits are depicted as dashed lines and  $R^2$  residuals are given. Dotted lines shown in (b) and (c) are guides-to-the-eye.

the absolute sensitivities ( $S_A$ ) increased with temperature and reached their maxima at 500 ( $4.1 \times 10^{-2} \text{K}^{-1}$ ) and 600 K ( $0.46 \times 10^{-2} \text{K}^{-1}$ ) for  $\text{NaYb}_{0.95}\text{Eu}_{0.05}(\text{MoO}_4)_2$  and  $\text{NaYb}_{0.95}\text{Eu}_{0.05}(\text{WO}_4)_2$ , respectively. The dependence of the  $S_A$  with temperature was not noticeable in the 100–300 K temperature range. Relative thermometric sensitivities ( $S_R$ ) computed for  $\text{NaYb}_{0.95}\text{Eu}_{0.05}(\text{MoO}_4)_2$  and  $\text{NaYb}_{0.95}\text{Eu}_{0.05}(\text{WO}_4)_2$  in 100–500 and 100–600 K temperature ranges are shown in **Figure 5.6c**, respectively.  $\text{NaYb}_{0.95}\text{Eu}_{0.05}(\text{MoO}_4)_2$  displayed its maximum relative sensitivity of  $1.27 \times 10^{-2} \text{K}^{-1}$  at 250 K and then gradually decreased with temperature. In contrast, maximum relative sensitivity of  $0.71 \times 10^{-2} \text{K}^{-1}$  was observed for  $\text{NaYb}_{0.95}\text{Eu}_{0.05}(\text{WO}_4)_2$  at 575 K. As far as thermometric sensitivity is concerned, it can be suggested that  $\text{NaYb}_{0.95}\text{Eu}_{0.05}(\text{MoO}_4)_2$  is

suitable to be used for cryogenic temperature sensing (i.e. near 250 K). Inspection of relative sensitivity plot of  $\text{NaYb}_{0.95}\text{Eu}_{0.05}(\text{WO}_4)_2$  reveals that values obtained in 100–325 K temperature range are close to zero, suggesting that  $\text{NaYb}_{0.95}\text{Eu}_{0.05}(\text{WO}_4)_2$  is unable to serve as a temperature sensor at temperatures below 325 K. However, interestingly,  $\text{NaYb}_{0.95}\text{Eu}_{0.05}(\text{WO}_4)_2$  is more suitable for sensing of intermediate temperatures as it shows its maximum relative sensitivity at a temperature above 500 K (i.e. at 575 K). Recently, phosphors featuring two rare-earth emitters have been extensively studied for temperature sensing. As shown in **Table 5.2**, maximum thermometric sensitivities of  $\text{NaYb}_{0.95}\text{Eu}_{0.05}(\text{MoO}_4)_2$  and  $\text{NaYb}_{0.95}\text{Eu}_{0.05}(\text{WO}_4)_2$  were compared with the values reported for other dual-emitter oxide thermosensitive phosphors.<sup>24, 48, 109-110</sup> This comparison shows the majority of the dual-emitter phosphors have exhibited their maximum sensitivities at temperatures below 500 K, whereas  $\text{NaYb}_{0.95}\text{Eu}_{0.05}(\text{WO}_4)_2$  exhibits its maximum thermometric sensitivity at 575 K. This reveals the potential of employing  $\text{NaYb}_{0.95}\text{Eu}_{0.05}(\text{WO}_4)_2$  for intermediate temperature sensing.

**Table 5.2.** Maximum Relative Thermometric Sensitivities ( $S_{R \max}$ ) of Dual-Emitter Phosphors

Composition	$S_{R \max}$	$T_{\max}$ (K)	Reference
Tb <sup>3+</sup> :Pr <sup>3+</sup> :NaGd(MoO <sub>4</sub> ) <sub>2</sub>	$2.05 \times 10^{-2} \text{ K}^{-1}$	400	110
Tb <sup>3+</sup> :Pr <sup>3+</sup> :NaLu(MoO <sub>4</sub> ) <sub>2</sub>	$2.51 \times 10^{-2} \text{ K}^{-1}$	303	110
Tb <sup>3+</sup> :Pr <sup>3+</sup> :NaLu(WO <sub>4</sub> ) <sub>2</sub>	$1.45 \times 10^{-2} \text{ K}^{-1}$	725	110
Eu <sup>3+</sup> :NaYb(MoO <sub>4</sub> ) <sub>2</sub>	$1.27 \times 10^{-2} \text{ K}^{-1}$	275	This work
Eu <sup>3+</sup> :NaYb(WO <sub>4</sub> ) <sub>2</sub>	$0.71 \times 10^{-2} \text{ K}^{-1}$	575	This work
Tb <sup>3+</sup> :Pr <sup>3+</sup> :LaVO <sub>4</sub>	$5.30 \times 10^{-2} \text{ K}^{-1}$	303	24
Tb <sup>3+</sup> :Pr <sup>3+</sup> :La <sub>2</sub> Ti <sub>3</sub> O <sub>9</sub>	$3.47 \times 10^{-2} \text{ K}^{-1}$	303	109
Tb <sup>3+</sup> :Pr <sup>3+</sup> :LuNbO <sub>4</sub>	$1.26 \times 10^{-2} \text{ K}^{-1}$	475	24
Eu <sup>3+</sup> :Mn <sup>4+</sup> :YAG	$4.81 \times 10^{-2} \text{ K}^{-1}$	350	48
Tb <sup>3+</sup> :Mn <sup>4+</sup> :YAG	$3.73 \times 10^{-2} \text{ K}^{-1}$	320	48
Dy <sup>3+</sup> :Mn <sup>4+</sup> :YAG	$3.16 \times 10^{-2} \text{ K}^{-1}$	340	48
Eu <sup>3+</sup> :Cr <sup>3+</sup> :YAG	$2.43 \times 10^{-2} \text{ K}^{-1}$	573	48
Dy <sup>3+</sup> :Cr <sup>3+</sup> :YAG	$2.32 \times 10^{-2} \text{ K}^{-1}$	450	48

#### 5.4. Conclusions

The potential of NaYb<sub>0.95</sub>Eu<sub>0.05</sub>(MoO<sub>4</sub>)<sub>2</sub> and NaYb<sub>0.95</sub>Eu<sub>0.05</sub>(WO<sub>4</sub>)<sub>2</sub> as thermosensitive phosphors in 100–500 and 100–600 K temperature ranges were evaluated, respectively. Luminescence emission of NaYb<sub>0.95</sub>Eu<sub>0.05</sub>(MoO<sub>4</sub>)<sub>2</sub> was more susceptible to temperature quenching than that of NaYb<sub>0.95</sub>Eu<sub>0.05</sub>(WO<sub>4</sub>)<sub>2</sub>. Maximum thermometric sensitivity of  $1.27 \times 10^{-2} \text{ K}^{-1}$  was observed at 250 K for NaYb<sub>0.95</sub>Eu<sub>0.05</sub>(MoO<sub>4</sub>)<sub>2</sub>, whereas NaYb<sub>0.95</sub>Eu<sub>0.05</sub>(WO<sub>4</sub>)<sub>2</sub> displayed the maximum sensitivity of  $0.71 \times 10^{-2} \text{ K}^{-1}$  at 575 K. Comparison of these values with those reported for other dual-emitter thermosensitive phosphors revealed the potential of employing NaYb<sub>0.95</sub>Eu<sub>0.05</sub>(WO<sub>4</sub>)<sub>2</sub> to probe intermediate temperatures. The strategy of using two emitters that show different thermal quenching characteristics allows manipulation of thermometric response of phosphors by mitigating the effect of thermal quenching. Therefore, coupling Yb<sup>3+</sup>–Yb<sup>3+</sup> dimers

with rare-earth ions that exhibit luminescence emission due to  $\text{Yb}^{3+}$ -sensitized upconversion can be used as a strategy to develop thermosensitive phosphors with enhanced thermometric performance.

## CHAPTER 6. DYSPROSIUM AND PRASEODYMIUM-COACTIVATED NaLa(MoO<sub>4</sub>)<sub>2</sub> THERMOSENSITIVE PHOSPHOR SYNTHESIZED USING MICROWAVE HEATING

### 6.1. Introduction

Rare-earth ions featuring thermally coupled levels such as Eu<sup>3+</sup>, Dy<sup>3+</sup>, Er<sup>3+</sup>, and Tm<sup>3+</sup> have incorporated as activators in NaLa(MoO<sub>4</sub>)<sub>2</sub> to develop materials for optical temperature sensing.<sup>23, 47, 109</sup> Much of this research has focused on employing the luminescence emission from thermally coupled levels of a single activator ion for temperature sensing. However, the luminescence response of rare-earth activator ions decreases with temperature due to thermal quenching, which is detrimental to the thermometric sensitivity of single-activator thermosensitive phosphors. Very recently, luminescence emission from two activators that exhibit distinct thermal quenching characteristics has employed for optical temperature sensing. This strategy allows manipulating the temperature-dependent luminescence response by tuning the chemical composition of phosphors. Temperature-dependent luminescence response of phosphors featuring Dy<sup>3+</sup> and Pr<sup>3+</sup> as an activator has been reported.<sup>111</sup> However, despite the significant differences in thermal quenching characteristics of luminescence emission of these two activators,<sup>112</sup> Dy<sup>3+</sup> and Pr<sup>3+</sup>-coactivated phosphors have not been investigated for optical temperature sensing. As shown in **Figure 6.1**, upon ultraviolet excitation, Dy<sup>3+</sup> activated NaLa(MoO<sub>4</sub>)<sub>2</sub> displays blue (~484 nm) and green (~574 nm) emissions,<sup>23</sup> whereas Pr<sup>3+</sup> displays bands in the red region (~603 and ~649) of the emission spectrum.<sup>113-114</sup> Herein, temperature-dependent luminescence response of Dy<sup>3+</sup> and Pr<sup>3+</sup> coactivated NaLa(MoO<sub>4</sub>)<sub>2</sub> was investigated with the aim of employing green and red emission from Dy<sup>3+</sup> and Pr<sup>3+</sup> for temperature sensing, respectively. NaLa<sub>0.95</sub>Dy<sub>0.025</sub>Pr<sub>0.025</sub>(MoO<sub>4</sub>)<sub>2</sub> was synthesized using microwave heating method, which provides an energy-efficient synthetic route compared to conventional solid-state reactions. The thermometric response was quantitatively

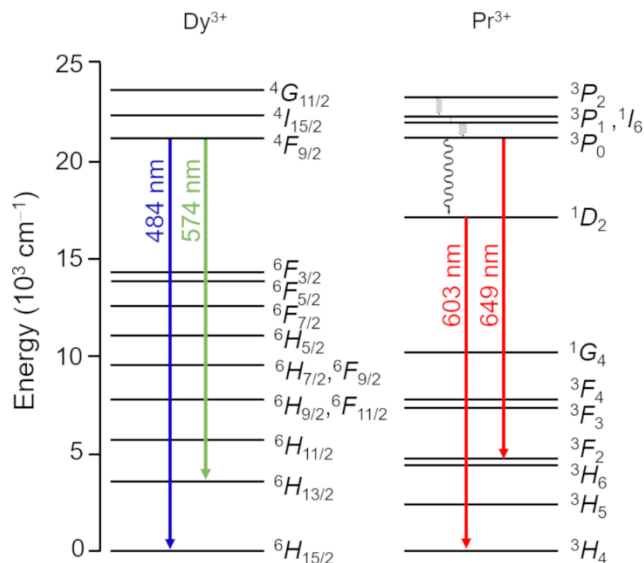


**Figure 6.1.** Dieke diagram of  $\text{Dy}^{3+}$  and  $\text{Pr}^{3+}$  ions. Intraconfigurational  $f-f$  transitions responsible for emissions from  $\text{Dy}^{3+}$  (blue and green) and  $\text{Pr}^{3+}$  (red) observed in  $\text{NaLa}_{0.95}\text{Dy}_{0.025}\text{Pr}_{0.025}(\text{MoO}_4)_2$ .

investigated in the 250–700 K temperature range using luminescence intensity ratio approach. Thermometric sensitivity of  $\text{NaLa}_{0.95}\text{Dy}_{0.025}\text{Pr}_{0.025}(\text{MoO}_4)_2$  was compared with other reported single-activator thermosensitive phosphors featuring  $\text{Dy}^{3+}$  or  $\text{Pr}^{3+}$ . The potential of employing  $\text{NaLa}_{0.95}\text{Dy}_{0.025}\text{Pr}_{0.025}(\text{MoO}_4)_2$  as a sensor to probe intermediate temperatures was highlighted.

## 6.2. Experimental

### 6.2.1. Synthesis

#### 6.2.1.1. Synthesis of $\text{NaLa}_{0.95}\text{Dy}_{0.025}\text{Pr}_{0.025}(\text{MoO}_4)_2$ Using Microwave Heating

Polycrystalline  $\text{NaLa}_{0.975}\text{Dy}_{0.025}\text{Pr}_{0.025}(\text{MoO}_4)_2$  powder was synthesized using microwave heating methods as stated in **section 2.2.1.5**.  $\text{Na}_2\text{CO}_3$  (99.5 %),  $\text{La}_2\text{O}_3$  (99.9 %),  $\text{Dy}_2\text{O}_3$  (99.99 %),  $\text{Pr}(\text{C}_5\text{H}_7\text{O}_2)_3$  (99.9 %), and  $\text{MoO}_3$  (99.5 %) were used as starting materials. Stoichiometric amounts of starting materials were mixed with a small amount of acetone and ground in an agate mortar for ~30 min. The unreacted powder mixture was placed in an alumina crucible. Next, the alumina crucible was placed in a secondary porcelain crucible filled with activated charcoal granules



(See **Figure 2.1** in **Chapter 2**). Crucible system was heated in a microwave oven operating at a frequency of 2450 MHz with 1200 W maximum output power. Six heating cycles were employed; a typical heating cycle includes three minutes of continuous heating at a power of 900 W followed by a cooling step. An Intermittent grinding step was employed after the 4<sup>th</sup> heating cycle to improve the homogeneity of the powder. The powder mixture was heated for a total of 18 minutes (six cycles) to obtain a phase-pure product.

### 6.2.1.2. Conventional Solid-State Synthesis of $\text{NaLa}_{0.975}\text{Dy}_{0.025}\text{Pr}_{0.025}(\text{MoO}_4)_2$

Polycrystalline  $\text{NaLa}_{0.975}\text{Dy}_{0.025}\text{Pr}_{0.025}(\text{MoO}_4)_2$  powder was synthesized using conventional solid-state reactions.  $\text{Na}_2\text{CO}_3$  (99.5 %),  $\text{La}_2\text{O}_3$  (99.9 %),  $\text{Dy}_2\text{O}_3$  (99.99 %),  $\text{Pr}(\text{C}_5\text{H}_7\text{O}_2)_3$  (99.9 %), and  $\text{MoO}_3$  (99.5 %) were used as starting materials. Stoichiometric amounts of starting materials were heated under the optimized synthesis conditions (see **section 2.2.1.1**) to obtain phase-pure product.

### 6.2.2. Rietveld Analysis

Rietveld refinements of powder XRD pattern of  $\text{NaLa}_{0.975}\text{Dy}_{0.025}\text{Pr}_{0.025}(\text{MoO}_4)_2$  synthesized using microwave heating was performed using the General Structure Analysis System (GSAS) with the graphical user interphase (EXPGUI) software<sup>83</sup> according to method stated in **section 2.2.3.5**. Fractional atomic coordinates of the oxygen atoms ( $x_{\text{O}}$ ,  $y_{\text{O}}$ ,  $z_{\text{O}}$ ) and an isotropic displacement parameter for all metal atoms in the structure ( $U_{\text{iso}}^M$ ) were refined. The isotropic displacement parameter for the oxygen atom ( $U_{\text{iso}}^{\text{O}}$ ) was constrained according to  $U_{\text{iso}}^{\text{O}} = 1.5 \times U_{\text{iso}}^M$ . The occupancies of the rare-earth containing  $4b$  site were fixed according to the nominal Na:La:Dy:Pr molar ratio of 0.5:0.475:0.0125:0.0125. Residual  $R_{\text{wp}}$  values and visual inspection of the difference curves of the Rietveld fits were employed to assess the quality of the refined structural models.

### 6.2.3. Spectrofluorometry

Spectrofluorometric analyses were carried out using a Fluorolog 3–222 fluorometer (Horiba Scientific) featuring a continuous wave Xe lamp (450 W). Excitation and emission spectra were recorded in the front-face geometry. Appropriate band-pass filters were used for the data collection. Temperature-dependent steady-state excitation and emission spectra of  $\text{NaLa}_{0.95}\text{Dy}_{0.025}\text{Pr}_{0.025}(\text{MoO}_4)_2$  were collected according to the method stated in **section 2.2.2.6**. The excitation and emission spectra were collected in the 250–700 K temperature range at 50 K intervals. A heating rate of  $5 \text{ K min}^{-1}$  was employed. Samples were allowed to dwell for  $\sim 10$  min at the target temperature prior to data collection.

## 6.3. Results and Discussion

### 6.3.1. Structural Characterization of $\text{NaLa}_{0.95}\text{Dy}_{0.025}\text{Pr}_{0.025}(\text{MoO}_4)_2$

Rietveld analysis of powder XRD data of microwave synthesized  $\text{NaLa}_{0.95}\text{Dy}_{0.025}\text{Pr}_{0.025}(\text{MoO}_4)_2$  was performed to probe the phase-purity. Fits of the scheelite-type tetragonal structure to the experimental patterns are shown in **Figures 6.2a**. The structural parameters extracted from the Rietveld refinement is provided in **Table 6.1**. As evident from the difference curves of the fits, the agreement between the calculated and the experimental XRD patterns was adequate. All the diffraction maxima were indexed to the corresponding molybdate phase. No extra peaks corresponding to a secondary crystalline phase was observed, confirming the phase-purity of the phosphors. X-ray diffraction patterns of  $\text{NaLa}_{0.95}\text{Dy}_{0.025}\text{Pr}_{0.025}(\text{MoO}_4)_2$  phosphors synthesized using the microwave and conventional solid-state heating methods were compared. As shown in **Figure 6.2b**, identical X-ray diffraction patterns were obtained for both powders confirming the structural similarity of the phosphors resulted from two heating methods.

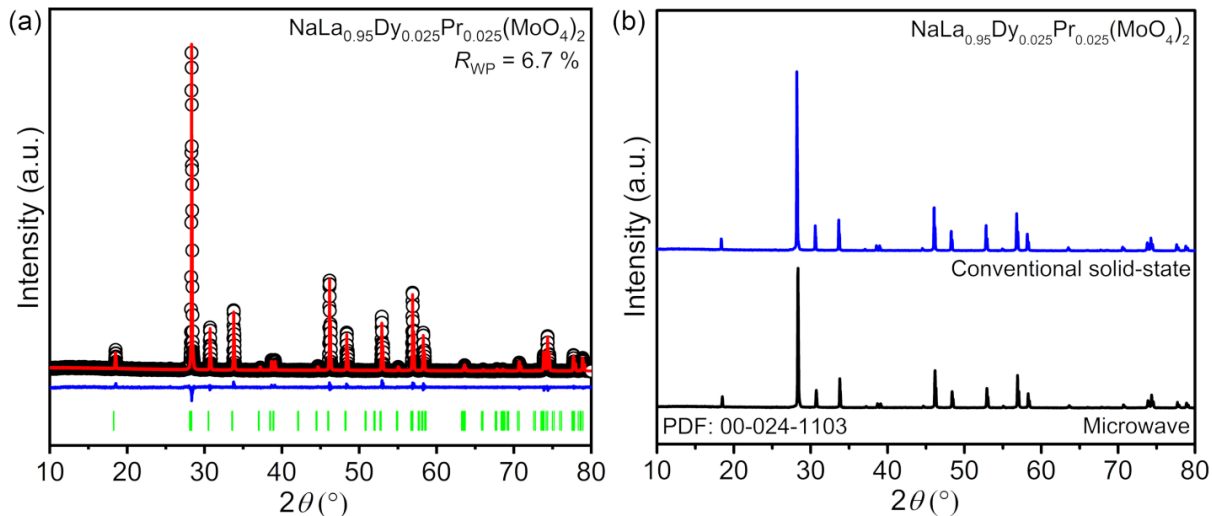


**Figure 6.2.** Rietveld analysis of the PXRD pattern of (a)  $\text{NaLa}_{0.95}\text{Dy}_{0.025}\text{Pr}_{0.025}(\text{MoO}_4)_2$  experimental (○) and calculated (—) patterns are shown along with the difference curve (—). Tick marks (|) correspond to the calculated positions of the diffraction maxima. (b) Comparison between the PXRD patterns of  $\text{NaLa}_{0.95}\text{Dy}_{0.025}\text{Pr}_{0.025}(\text{MoO}_4)_2$  synthesized using conventional solid-state and microwave heating methods.

**Table 6.1.** Structural Parameters of  $\text{NaLa}_{0.95}\text{Dy}_{0.025}\text{Pr}_{0.025}(\text{MoO}_4)_2$

$a$ (Å)	5.33990 (3)
$c$ (Å)	11.72520 (7)
$V$ (Å <sup>3</sup> )	334.338(4)
$x_0$	0.1340 (6)
$y_0$	0.4816 (6)
$z_0$	0.2054 (3)
$U_{\text{iso}}^M$ (Å <sup>2</sup> ) <sup>a</sup>	0.52 (7)
$U_{\text{iso}}^O$ (Å <sup>2</sup> ) <sup>a</sup>	0.930(9)
$R_{\text{wp}}$	6.7

<sup>a</sup> Given as  $100 \times U$ .

### 6.3.2. Steady-State Photoluminescence

#### 6.3.2.1. Room-Temperature Steady-State Photoluminescence

Photoluminescence response of  $\text{NaLa}_{0.95}\text{Dy}_{0.025}\text{Pr}_{0.025}(\text{MoO}_4)_2$  prepared using two synthetic routes (i.e., conventional solid-state and microwave heating) was investigated at room temperature. **Figures 6.3a and 6.3b** show the comparison between the excitation and emission spectra recorded for  $\text{NaLa}_{0.95}\text{Dy}_{0.025}\text{Pr}_{0.025}(\text{MoO}_4)_2$  resulted from two synthetic routes. Comparison of spectra reveals phosphors prepared from both methods have almost identical luminescence response at room temperature. This confirms the potential of employing microwave heating method as a new synthetic route to prepare rare-earth activated double molybdates.

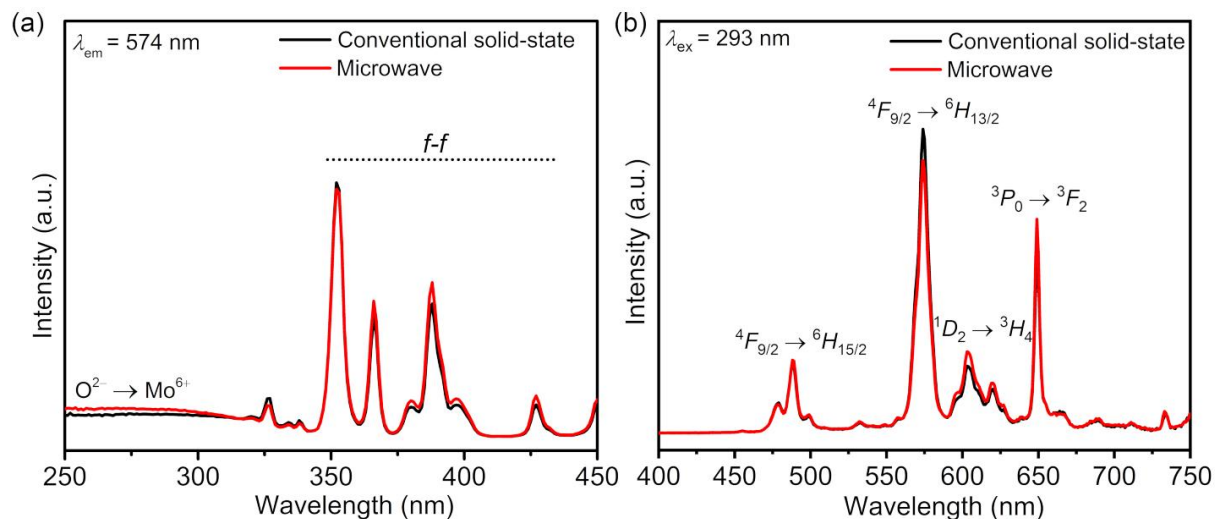


**Figure 6.3.** Comparison of the photoluminescence (a) excitation and (b) emission spectra collected for  $\text{NaLa}_{0.95}\text{Dy}_{0.025}\text{Pr}_{0.025}(\text{MoO}_4)_2$  synthesized using conventional solid-state and microwave heating methods. Nearly identical luminescence response was observed for both samples.

#### 6.3.2.2. Temperature-Dependent Steady-State Photoluminescence

Temperature-dependent luminescence response of  $\text{NaLa}_{0.95}\text{Dy}_{0.025}\text{Pr}_{0.025}(\text{MoO}_4)_2$  synthesized using microwave heating was investigated to reveal its potential as an optical temperature sensor. **Figure 6.4a** shows the temperature-dependent excitation spectra recorded in

the 250–700 K temperature-range at 50 K intervals. Excitation spectra were collected at 574 nm ( $^4F_{9/2} \rightarrow ^6H_{13/2}$  transition of  $Dy^{3+}$ ) as it offered a better signal-to-noise ratio than the spectra collected at 603 nm ( $^1D_2 \rightarrow ^3H_4$  transition of  $Pr^{3+}$ ). Excitation spectra consist of a broad  $O^{2-} \rightarrow Mo^{6+}$  charge-transfer band and a series of narrow bands resulting from intraconfigurational  $f-f$  transitions of  $Dy^{3+}$ . Rare-earth activated scheelite phosphors show a strong charge-transfer band, which is an indication of efficient host-activator energy-transfer.<sup>6, 40</sup> However, in the case of  $NaLa_{0.95}Dy_{0.025}Pr_{0.025}(MoO_4)_2$ , the charge-transfer band was weaker than the bands corresponding to intraconfigurational  $f-f$  transitions, indicating the host-activator energy-transfer is less efficient than the direct excitation of activator ions. Despite the weak charge-transfer band observed for  $NaLa_{0.95}Dy_{0.025}Pr_{0.025}(MoO_4)_2$ , emission spectra were collected using the excitation of the host's charge-transfer (293 nm) and subsequent energy-transfer to activator ions to obtain emission from both activators simultaneously. Temperature-dependent emission spectra recorded in the 250–700 K temperature range are shown in **Figure 6.4b**. The bands in blue and green regions of the emission spectra are due to the  $^4F_{9/2} \rightarrow ^6H_{15/2}$  (~484 nm) and  $^4F_{9/2} \rightarrow ^6H_{13/2}$  (~574 nm) transitions of  $Dy^{3+}$ .<sup>115</sup> The red bands centering at ~603 and ~649 nm originated from  $^1D_2 \rightarrow ^3H_4$  and  $^3P_0 \rightarrow ^3F_2$  radiative transitions of  $Pr^{3+}$ , respectively.<sup>116</sup> Intensities of all emission bands decreased with temperature due to thermal quenching. Inspection of temperature-dependent emission spectra reveals  $Dy^{3+}$  and  $Pr^{3+}$  have different thermal quenching characteristics when incorporated in  $NaLa(MoO_4)_2$  host. This was expected as  $Dy^{3+}$  and  $Pr^{3+}$  have significantly different activation energies for thermal quenching for their photoluminescence emissions.<sup>112</sup> Interestingly, red bands originated from the radiative transitions of  $Pr^{3+}$  exhibited different thermal quenching characteristics. Specifically, band centered at ~649 nm ( $^3P_0 \rightarrow ^3F_2$ ) was more sensitive to temperature than the band centered at ~603 nm ( $^1D_2 \rightarrow ^3H_4$ ). This

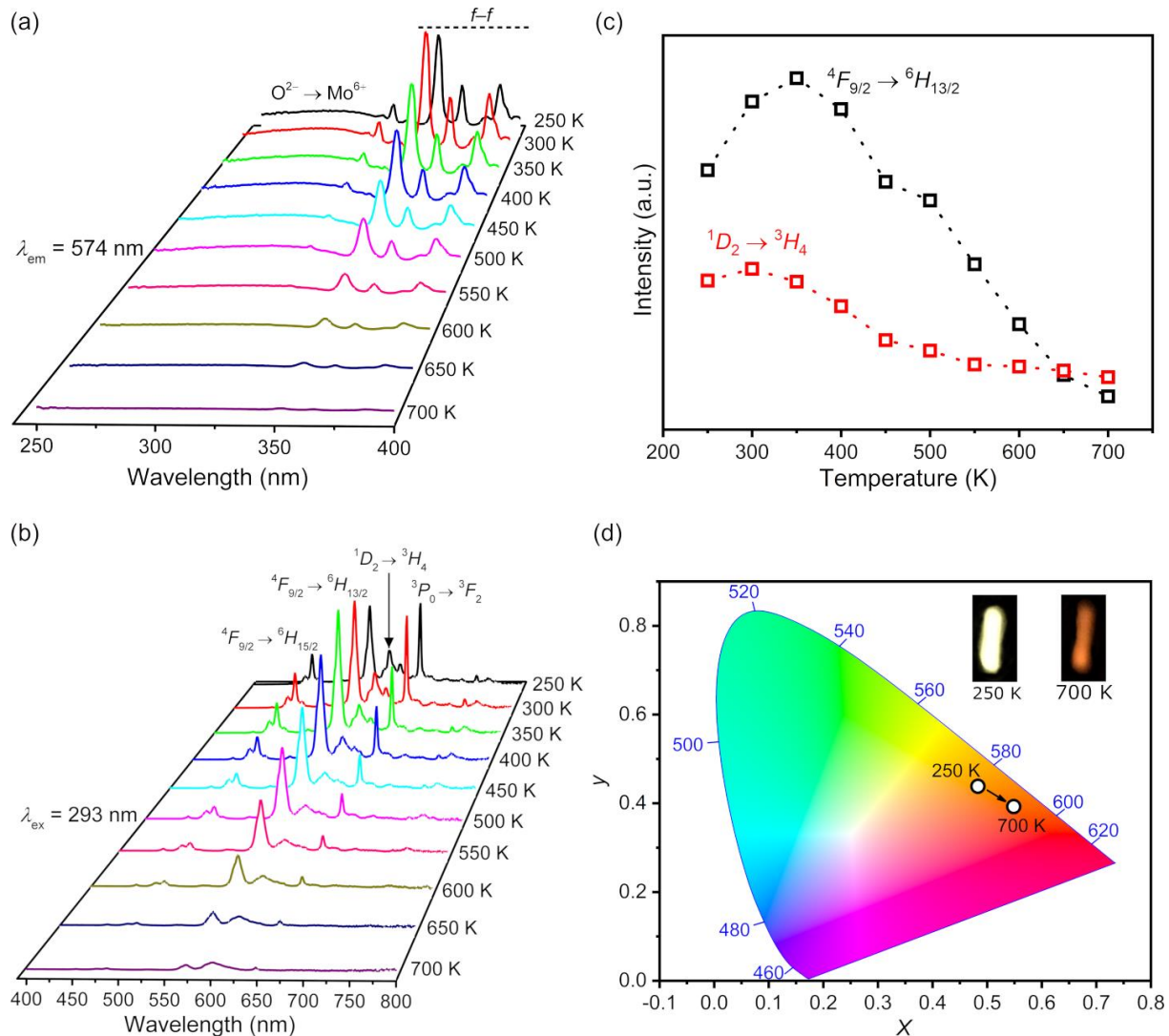


**Figure 6.4.** Temperature-dependent (a) excitation and (b) emission spectra recorded in the 250–700 K temperature range for  $\text{NaLa}_{0.95}\text{Dy}_{0.025}\text{Pr}_{0.05}(\text{MoO}_4)_2$ . Excitation spectra consisting of a series of narrow bands responsible for  $f-f$  transitions are stronger than the charge-transfer band. Emission spectra exhibits bands originate from  $\text{Dy}^{3+}$  (blue and green) and  $\text{Pr}^{3+}$  (red). (c) Integrated intensities of the green ( ${}^4F_{9/2} \rightarrow {}^6H_{13/2}$ ) and red ( ${}^1D_2 \rightarrow {}^3H_4$ ) bands as a function of temperature. (d) The temperature-driven color change is displayed in the CIE diagram.  $\text{NaLa}_{0.95}\text{Dy}_{0.025}\text{Pr}_{0.05}(\text{MoO}_4)_2$  powder luminescing at 250 (yellow) and 700 K (red) are shown in the insets.

observation is comparable to what was observed for  $\text{Pr}^{3+}$ -activated  $\text{KLa}(\text{MoO}_4)_2$  and  $\text{Na}_5\text{Lu}(\text{WO}_4)_4$ .<sup>113-114</sup> The energy gap between the  ${}^3P_0$  level and the next lower lying  ${}^1D_2$  level is approximately  $\sim 3700 \text{ cm}^{-1}$ .<sup>110, 117</sup> Therefore, depopulation of  ${}^3P_0$  level is possible via multiphonon

relaxations since the phonon energy cut-off for  $\text{NaLa}(\text{MoO}_4)_2$  was  $\sim 900 \text{ cm}^{-1}$  (i.e., 4<sup>th</sup> order process).<sup>118</sup> In contrast, red emission originates from  $^1D_2 \rightarrow ^3H_4$  radiative-transition is less sensitive to temperature due to the large activation energy for thermal quenching ( $\Delta E_{\text{activation}} > 5000 \text{ cm}^{-1}$ ).<sup>113,</sup>  
<sup>119</sup> Owing to the distinct thermal quenching characteristics of the green ( $\sim 574 \text{ nm}$ ) and red band centered at  $\sim 603 \text{ nm}$ , their temperature-dependent response was investigated in the 250–700 K temperature with the aim of employing them for optical temperature sensing. The plot of integrated intensities of the green and red emissions as a function of temperature are shown in the **Figure 6.4c**. The integrated intensities of both bands initially increased with temperature and then decreased due to thermal quenching. The highest integrated intensity for the green and red emission bands was observed at 350 and 300 K respectively. The integrated intensity of the green band was higher than that of the red band in the 250–600 K temperature range. Although the integrated intensities of both bands decreased with temperature, the green band was more susceptible to thermal quenching. As a result, at temperatures above 650 K, red emission was prominent. The difference in temperature-dependent response of the green and the red emission bands led to a temperature-driven color change in the photoluminescence emission, which was visible to the naked eye. photoluminescence emission changed from yellow to red as the temperature of the phosphor increased from 250 to 700 K. As shown in **Figure 6.4d**, a CIE diagram was employed to quantitatively evaluate this temperature-dependent color change of the photoluminescence emission.

Temperature-dependent emission spectra were qualitatively analyzed to assess the performance of  $\text{NaLa}_{0.95}\text{Dy}_{0.025}\text{Pr}_{0.025}(\text{MoO}_4)_2$  as a thermosensitive phosphor. To this end, three metrics were computed using the temperature-dependent emission spectra: luminescence intensity

ratio  $R(T)$  (equation 6.3), absolute sensitivity ( $S_A$ ) (equation 1.3), and relative sensitivity ( $S_R$ ) (equation 1.4).

$$R(T) = \frac{I_{\text{Red (603 nm)}}}{I_{\text{Green (574 nm)}}} \quad (6.1)$$

Luminescence intensity ratio was computed using the integrated intensities of the green and the red bands centered at ~574 and ~603 nm, respectively. In all cases, both green and red bands were fit with Gaussian curves to obtain the integrated intensities. Two Gaussian curves were employed to fit the green band, whereas the red band was fit with three curves. Plots of luminescence intensity ratio, absolute and relative sensitivities as a function of temperature are shown in **Figures 6.5a–f**, respectively. Luminescence intensity ratios computed for  $\text{NaLa}_{0.95}\text{Dy}_{0.025}\text{Pr}_{0.025}(\text{MoO}_4)_2$  decreased with temperature in the 250–500 K temperature range and then, gradually increased to the maxima at 700 K. Therefore, thermometric performance of the phosphor was investigated in two temperature regimes: Low-temperature (250–450 K) and high-temperature (500–700 K). As shown in **Figures 6.5a and 6.5b**, in the low-temperature regime, the maximum  $R(T)$  value of 0.53 was observed at 250 K, whereas in the high-temperature regime, the maximum of 2.8 was observed at 700 K, respectively. The experimental  $R(T)$  values were fit with the equation 6.4.

$$R(T) = A \exp\left(-\frac{B}{T}\right) + C \quad (6.2)$$



**Table 6.2.** Relative Thermometric Sensitivities of Dy<sup>3+</sup> and Pr<sup>3+</sup>-Activated Phosphors

Composition	$S_R$ at 700 K (K <sup>-1</sup> )	Reference
NaDy(MoO <sub>4</sub> ) <sub>2</sub>	$3.8 \times 10^{-3}$	22
Dy <sup>3+</sup> :Na <sub>5</sub> La(WO <sub>4</sub> ) <sub>4</sub>	$3.0 \times 10^{-3}$	22
Dy <sup>3+</sup> :Y <sub>4</sub> Al <sub>2</sub> O <sub>9</sub>	$4.0 \times 10^{-3}$	77
Dy <sup>3+</sup> :Ca <sub>2</sub> Al <sub>2</sub> SiO <sub>7</sub>	$3.2 \times 10^{-3}$	77
Dy <sup>3+</sup> :YNbO <sub>3</sub>	$3.4 \times 10^{-3}$	24
Dy <sup>3+</sup> :Y <sub>3</sub> Al <sub>5</sub> O <sub>12</sub>	$4.4 \times 10^{-3}$	77
Dy <sup>3+</sup> :Y <sub>2</sub> SiO <sub>5</sub>	$4.1 \times 10^{-3}$	77
Pr <sup>3+</sup> :Y <sub>2</sub> Ti <sub>2</sub> O <sub>7</sub>	$9.3 \times 10^{-3}$	119
Pr <sup>3+</sup> :Y <sub>3</sub> Al <sub>5</sub> O <sub>12</sub>	$5.0 \times 10^{-3}$	118
Pr <sup>3+</sup> :Ba <sub>0.7</sub> Sr <sub>0.3</sub> TiO <sub>3</sub>	$8.7 \times 10^{-3}$	121
Pr <sup>3+</sup> :MgLaTiO <sub>6</sub>	$1.0 \times 10^{-2}$	121
Pr <sup>3+</sup> :(K <sub>0.5</sub> Na <sub>0.5</sub> )NbO <sub>3</sub>	$1.6 \times 10^{-2}$	120
Pr <sup>3+</sup> :Dy <sup>3+</sup> :NaLa(MoO <sub>4</sub> ) <sub>2</sub>	$1.8 \times 10^{-2}$	This work

Here,  $A$ ,  $B$ , and  $C$  are constants,  $T$  is the absolute temperature. Adequate fits were obtained for  $R(T)$  plots in both low and high-temperature regimes. Plots of absolute sensitivity ( $S_A$ ) values computed for the low and high-temperature regimes are shown in **Figures 6.5c and 6.5d**, respectively. In the low temperature regime, the maximum  $S_A$  value of  $0.20 \times 10^{-2} \text{ K}^{-1}$  was obtained at 250 K, whereas for the high-temperature regime, maximum of  $4.90 \times 10^{-2} \text{ K}^{-1}$  was observed at 700 K. Relative thermometric sensitivities computed ( $S_R$ ) for low and high temperature regimes were plot as a function of temperature and are shown in **Figures 6.5e and 6.5f**, respectively. In the low- temperature regime, the maximum  $S_R$  of  $0.4 \times 10^{-2} \text{ K}^{-1}$  was observed at 250 K. Contrary to what has observed for single-activator thermosensitive phosphors, in the high-temperature regime,  $S_R$  increased with temperature and reached the maxima ( $1.8 \times 10^{-2} \text{ K}^{-1}$ ) at 700 K. This

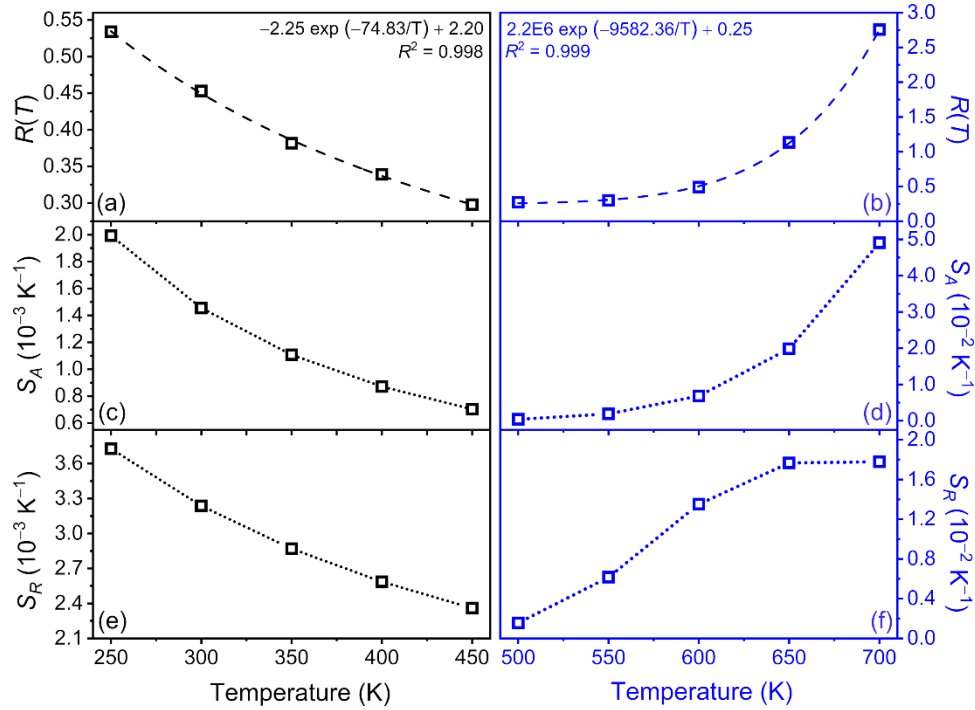


**Figure 6.5.** (a) Luminescence intensity ratio ( $R(T)$ ), (b) absolute sensitivity ( $S_A$ ), and (c) relative sensitivity ( $S_R$ ) of  $\text{NaLa}_{0.95}\text{Dy}_{0.025}\text{Pr}_{0.025}(\text{MoO}_4)_2$  in the low and high temperature regimes. Analytical expressions used to fit experimental  $R(T)$  values are given. The corresponding fits are depicted as dashed lines and  $R^2$  residuals are given. Dotted lines shown in (c)–(f) are guides-to-the-eye.

suggests that employing the luminescence response of two activator ions incorporated into a single host serves as a strategy to overcome the effect of thermal quenching on thermometric sensitivity. Thermometric sensitivity of  $\text{NaLa}_{0.95}\text{Dy}_{0.025}\text{Pr}_{0.025}(\text{MoO}_4)_2$  at 700 K was compared with the values reported for other phosphors featuring  $\text{Dy}^{3+}$  or  $\text{Pr}^{3+}$ . Inspection of  $S_R$  values given in **Table 6.2** shows that thermometric sensitivity of  $\text{NaLa}_{0.95}\text{Dy}_{0.025}\text{Pr}_{0.025}(\text{MoO}_4)_2$  at 700 K is higher than that reported for other  $\text{Dy}^{3+}$  or  $\text{Pr}^{3+}$ -activated oxides<sup>23-24, 77, 119-121</sup> phosphors revealing the potential of employing  $\text{NaLa}_{0.95}\text{Dy}_{0.025}\text{Pr}_{0.025}(\text{MoO}_4)_2$  as a sensor to probe intermediate temperatures.

## 6.4 Conclusions

Microwave heating serves as an efficient method to synthesize rare-earth activated  $\text{NaLa}(\text{MoO}_4)_2$ .  $\text{Dy}^{3+}$  and  $\text{Pr}^{3+}$ -coactivated  $\text{NaLa}(\text{MoO}_4)_2$  was synthesized using microwave heating method, and its temperature-dependent luminescence response was investigated in the 250–700 K temperature range. Maximum thermometric sensitivity of  $1.8 \times 10^{-2} \text{ K}^{-1}$  was observed at 700 K. Comparison of thermometric sensitivity of  $\text{NaLa}_{0.95}\text{Dy}_{0.025}\text{Pr}_{0.025}(\text{MoO}_4)_2$  at 700 K with those reported for  $\text{Dy}^{3+}$  or  $\text{Pr}^{3+}$ -activated phosphors revealed the potential of employing  $\text{NaLa}_{0.95}\text{Dy}_{0.025}\text{Pr}_{0.025}(\text{MoO}_4)_2$  as a thermosensitive phosphor to probe intermediate temperatures. Employing photoluminescence emission from two activators that exhibit distinct thermal quenching serves as a strategy to enhance the thermometric performance of phosphors. Therefore, coupling two rare-earth ions or rare-earth and a transition metal ion that show different thermal quenching characteristics should be the focus to develop phosphors with an enhanced thermometric response.

## CHAPTER 7. CONCLUSIONS AND PERSPECTIVES

Thermometric response of a series of phosphors derived from group VI  $d^0$  scheelite and scheelite-type metal oxides of chemical formula  $\text{Na}_x\text{RE}(\text{MO})_w$  (RE = Y and rare-earth, M = Mo, W) were investigated. Single- and dual-emitter thermosensitive phosphors were developed by substituting the optically silent  $\text{La}^{3+}$  ion in hosts with optically active rare-earth ions. Their potential as thermosensitive phosphors to probe intermediate temperatures was revealed. The experimental results of the investigations were discussed with the perspective of understanding how to tailor the thermometric response by using the composition and the crystal structure of phosphor as levers.

Thermometric response of a series of  $\text{Dy}^{3+}$ -activated scheelite and scheelite-related phosphors were investigated, and their potential as single-emitter thermosensitive phosphors was revealed. Maximum thermometric sensitivities observed at 350 and 750 K were comparable to those reported for the other  $\text{Dy}^{3+}$ -activated phosphors. However, thermometric sensitivities of these phosphors were nearly independent of the host's crystal structure and the  $\text{Dy}^{3+}$  concentration. In this investigation, upon changing the crystal structure of the host and the  $\text{Dy}^{3+}$  concentration, it was expected to observe systematic changes in the thermometric sensitivity of phosphors. Absence of such systematic changes in the thermometric sensitivity restricted the utilization of experimental results to build a relationship between the thermometric response and chemical and structural variables related to the phosphors under investigation. Exploring a new family of materials that can be employed as hosts for thermosensitive phosphors should be the focus of future research on single-emitter thermosensitive phosphors. Such a family of materials should allow manipulation of the composition of phosphor via chemical substitution leading to systematic changes in the thermometric response. Thermometric sensitivity of these single-emitter phosphors decreased with

temperature, which hindered their ability to perform as thermosensitive phosphors particularly at intermediate temperatures. To improve the thermometric sensitivity at intermediate temperatures, dual-emitter thermosensitive phosphors were developed.

In the case of dual-emitter thermosensitive phosphors, the luminescence emission from two rare-earth ions that exhibit different thermal quenching characteristics was employed as a strategy to mitigate the effect of thermal quenching on thermometric sensitivity. This strategy enhanced the control over the temperature-dependent thermometric response of phosphors as it allowed to utilize the photoluminescence emission originate from two emitters. In  $\text{Eu}^{3+}$ -activated  $\text{NaYb}(\text{MO}_4)_2$  dual-activator thermosensitive phosphors, intrinsic disorder present in  $\text{NaYb}(\text{MO}_4)_2$  host allowed to tailor the thermometric response via manipulation of the chemical composition. The potential of employing the blue cooperative luminescence from  $\text{Yb}^{3+}$ - $\text{Yb}^{3+}$  dimers and the red emission of  $\text{Eu}^{3+}$  due to  $\text{Yb}^{3+}$ -sensitized upconversion for temperature sensing was revealed. Significant differences in the thermal quenching characteristics of the blue and red emissions led to a temperature-driven color change of the photoluminescence emission under 980 nm excitation. Different thermometric responses were observed for  $\text{NaYb}_{0.95}\text{Eu}_{0.05}(\text{MoO}_4)_2$  and  $\text{NaYb}_{0.95}\text{Eu}_{0.05}(\text{WO}_4)_2$  phosphors under investigation regardless of the similarities in their composition and the crystal structure. Clustering of rare-earth ions due to the intrinsic disorder present in the crystal structure of  $\text{NaYb}(\text{MO}_4)_2$  was suggested as the origin of these discrepancies.  $\text{NaYb}_{0.95}\text{Eu}_{0.05}(\text{MoO}_4)_2$  and  $\text{NaYb}_{0.95}\text{Eu}_{0.05}(\text{WO}_4)_2$  displayed their maximum relative sensitivities of  $1.27 \times 10^{-2} \text{ K}^{-1}$  and  $0.71 \times 10^{-2} \text{ K}^{-1}$ , respectively. It was suggested that  $\text{NaYb}_{0.95}\text{Eu}_{0.05}(\text{WO}_4)_2$  is suitable to be employed as a thermosensitive phosphor to probe intermediate temperatures as it displayed its maximum sensitivity at 575 K. We propose that  $\text{NaYb}(\text{MO}_4)_2$  host should be activated with other rare-earth ions such as  $\text{Tb}^{3+}$  and  $\text{Nd}^{3+}$ , which exhibit photoluminescence

emission due to  $\text{Yb}^{3+}$ -sensitized upconversion processes. This will enable to employ the cooperative blue emission coupled with the emission due to  $\text{Yb}^{3+}$ -sensitized upconversion from rare-earth ions for temperature sensing. Further, new and existing rare-earth-activated oxides with a positional disorder in their crystal structures should be explored as thermosensitive phosphors. This will pave the way to understand how to employ the intrinsic structural features present in the crystal structures as levers to tailor the thermometric response.

$\text{NaLa}(\text{MoO}_4)_2$  was activated with two rare-earth ions that have different activation energies for thermal quenching to develop a dual-emitter thermosensitive phosphor.  $\text{Dy}^{3+}$  and  $\text{Pr}^{3+}$ -co activated  $\text{NaLa}(\text{MoO}_4)_2$  was synthesized using microwave heating method. A novel synthetic protocol was developed to prepare rare-earth-activated  $\text{NaLa}(\text{MoO}_4)_2$ . This method provided an energy-efficient and rapid synthetic route. Although there is a wealth of information available in the literature confirming the versatility of conventional solid-state reactions to synthesize various rare-earth-activated oxide materials, literature reports on microwave heating methods are scarce. Therefore, new synthetic protocols to prepare rare-earth-activated metalates using microwave heating method should be developed. Investigations on temperature-dependent luminescence response of  $\text{Dy}^{3+}$  and  $\text{Pr}^{3+}$ -coactivated  $\text{NaLa}(\text{MoO}_4)_2$  phosphor confirmed that employing the photoluminescence emission from two rare-earth ions that exhibit different thermal quenching characteristics serves a successful strategy to overcome the effect of thermal quenching on thermometric sensitivity. In  $\text{NaLa}_{0.95}\text{Dy}_{0.025}\text{Pr}_{0.025}(\text{MoO}_4)_2$ , green emission was more susceptible to thermal quenching than the red emission from  $\text{Pr}^{3+}$ . The significant differences in thermal quenching characteristics of the green and red emissions led to a temperature-driven color change of the photoluminescence emission. Thermometric performance of  $\text{NaLa}_{0.95}\text{Dy}_{0.025}\text{Pr}_{0.025}(\text{MoO}_4)_2$  was investigated in two temperature regimes. Maximum relative sensitivity of  $1.8 \times 10^{-2} \text{ K}^{-1}$  was

obtained at 700 K. Comparison of this value with those reported for other  $\text{Dy}^{3+}$  or  $\text{Pr}^{3+}$ -activated single-emitter thermosensitive phosphors revealed that  $\text{NaLa}_{0.95}\text{Dy}_{0.025}\text{Pr}_{0.025}(\text{MoO}_4)_2$  exhibits a comparable relative sensitivity at 700 K. To further maximize the relative sensitivity of dual emitter thermosensitive phosphors, a rare-earth ion should be coupled with a transition metal ion (e.g.  $\text{Cr}^{3+}$  and  $\text{Mn}^{4+}$ ) whose photoluminescence emission is more sensitive to temperature. The energy-transfer between rare-earth and transition metal ions can be detrimental to the thermometric response of phosphors. As a solution, hosts that have two specific crystallographic sites for rare-earth and transition metal ions could be used to develop dual-emitter thermosensitive phosphors. This will enable to utilize intrinsic structural features of hosts as tools to tailor the luminescence response. Further, dual-emitter thermosensitive phosphors should be developed using other metalate hosts such as niobates, tantalates, and vanadates. Thermometric performance of these phosphors should be investigated to reveal their potential as sensors to probe intermediate temperatures.

## REFERENCES

1. Shionoya, S.; Yen, W. M.; Yamamoto, H., *Phosphor handbook*, CRC press: 2018.
2. Cano-Torres, J. M.; Rico, M.; Han, X.; Serrano, M. D.; Cascales, C.; Zaldo, C.; Petrov, V.; Griebner, U.; Mateos, X.; Koopmann, P.; Kränkel, C., *Phys. Rev., B* **2011**, 84, 174207.
3. Cascales, C.; Serrano, M. D.; Esteban-Betegón, F.; Zaldo, C.; Peters, R.; Petermann, K.; Huber, G.; Ackermann, L.; Rytz, D.; Dupré, C.; Rico, M.; Liu, J.; Griebner, U.; Petrov, V., *Phys. Rev. B.*, **2006**, 74, 174114.
4. Guo, W.; Chen, Y.; Lin, Y.; Luo, Z.; Gong, X.; Huang, Y., *J. Appl. Phys.*, **2008**, 103, 093106.
5. Li, T.; Guo, C.; Zhao, P.; Li, L.; Jeong, J. H., *J. Am. Ceram. Soc.*, **2013**, 96, 1193.
6. Liu, Y.; Liu, G.; Wang, J.; Dong, X.; Yu, W., *Inorg. Chem.*, **2014**, 53, 11457.
7. Neeraj, S.; Kijima, N.; Cheetham, A. K., *Chem. Phy. Lett.*, **2004**, 387, 2.
8. Allison, S. W.; Gillies, G. T., *Review of Scientific Instruments*, **1997**, 68, 2615.
9. Vetrone, F.; Mahalingam, V.; Capobianco, J. A., *Chem. Mater.*, **2009**, 21, 1847.
10. Brites, C. D. S.; Lima, P. P.; Silva, N. J. O.; Millán, A.; Amaral, V. S.; Palacio, F.; Carlos, L. D., *Nanoscale*, **2012**, 4, 4799.
11. Khalid, A. H.; Kontis, K.; Behtash, H.-Z., *Proceedings of the Institution of Mechanical Engineers, Part G: J. Aerosp. Eng.*, **2010**, 224, 745.
12. Lawrence, M.; Zhao, H.; Ganippa, L., *Opt. Express*, **2013**, 21, 12260.
13. Haouari, M.; Maaoui, A.; Saad, N.; Bulou, A., *Sens. Actuator. A: Phys.*, **2017**, 261, 235.
14. Chambers, M. D.; Clarke, D. R., *Annu Rev Mater Res.*, **2009**, 39, 325.
15. Čulubrk, S.; Lojpur, V.; Ahrenkiel, S. P.; Nedeljković, J. M.; Dramićanin, M. D., *J. Lumin.*, **2016**, 170, 395.
16. Cao, Z.; Zhou, S.; Jiang, G.; Chen, Y.; Duan, C.; Yin, M., *Curr. Appl. Phys.*, **2014**, 14, 1067.



17. Cerón, E. N.; Ortgies, D. H.; del Rosal, B.; Ren, F.; Benayas, A.; Vetrone, F.; Ma, D.; Sanz-Rodríguez, F.; Solé, J. G.; Jaque, D.; Rodríguez, E. M., *Adv. Mater.*, **2015**, *27*, 4781.
18. Cui, Y.; Xu, H.; Yue, Y.; Guo, Z.; Yu, J.; Chen, Z.; Gao, J.; Yang, Y.; Qian, G.; Chen, B., *J. Am. Ceram. Soc.*, **2012**, *134*, 3979.
19. Hertle, E.; Chepyga, L.; Batentschuk, M.; Zigan, L., *J. Lumin.*, **2017**, *182*, 200.
20. Heyes, A. L., *J. Lumin.*, **2009**, *129*, 2004..
21. Lojpur, V.; Nikolic, M.; Mancic, L.; Milosevic, O.; Dramicanin, M. D., *Ceram. Int.*, **2013**, *39*, 1129.
22. Perera, S. S.; Dissanayake, K. T.; Rabuffetti, F. A., *J. Lumin.*, **2019**, *207*, 416.
23. Perera, S. S.; Rabuffetti, F. A., *J. Mater. Chem., C* **2019**, *7*, 7601.
24. Wu, Y.; Suo, H.; Zhao, X.; Zhou, Z.; Guo, C., *Inorg. Chem. Front.*, **2018**, *5*, 2456.
25. Hernández, I.; Pathumakanthar, N.; Wyatt, P.; Gillin, W., *Adv. Mater.*, **2010**; 5356.
26. Zhou, S.; Duan, C.; Yin, M.; Zhang, S.; Wang, C., *J. Alloy. Compd.*, **2019**, *784*, 970.
27. Pandey, A.; Som, S.; Kumar, V.; Kumar, V.; Kumar, K.; Rai, V. K.; Swart, H. C. *Sens. Actuator B: Chem*, **2014**, *202*, 1305.
28. Miyata, K.; Konno, Y.; Nakanishi, T.; Kobayashi, A.; Kato, M.; Fushimi, K.; Hasegawa, Y., *Angew. Chem. Int. Ed.*, **2013**, *52*, 6413.
29. Shen, X.; Yan, B., *Dalton Trans.*, **2015**, *44*, 1875.
30. Meert, K. W.; Morozov, V. A.; Abakumov, A. M.; Hadermann, J.; Poelman, D.; Smet, P. F., *Opt. Express*, **2014**, *22*, A961.
31. Pisarski, W. A.; Pisarska, J.; Lisiecki, R.; Ryba-Romanowski, W., *Sens. and Actuators A: Physical*, **2016**, *252*, 54.

32. Quintanilla, M.; Cantelar, E.; Cussó, F.; Villegas, M.; Caballero, A. C., *Appl. Phys. Express*, **2011**, 4, 022601.
33. Yang, X.; Fu, Z.; Yang, Y.; Zhang, C.; Wu, Z.; Sheng, T. J. J. o. t. A. C. S., *J. Am. Ceram. Soc.* **2015**, 98, 2595.
34. Suyver, J. F.; Grimm, J.; van Veen, M. K.; Biner, D.; Kramer, K. W.; Gudel, H. U., *J. Lumin.*, **2006**, 117, 1.
35. Abram, C.; Fond, B.; Beyrau, F., *Prog. Energy Combust. Sci.*, **2018**, 64, 93.
36. Husberg, T.; Gjirja, S.; Denbratt, I.; Omrane, A.; Aldén, M.; Engström, J., SAE International, **2005**.
37. Aldén, M.; Omrane, A.; Richter, M.; Särner, G., *Prog. Energy Combust. Sci.*, **2011**, 37, 422.
38. Omrane, A.; Petersson, P.; Aldén, M.; Linne, M. A., *Appl. Phys., B* **2008**, 92, 99.
39. Omrane, A.; Juhlin, G.; Ossler, F.; Aldén, M., *Appl. Opt.*, **2004**, 43, 3523.
40. Neeraj, S.; Kijima, N.; Cheetham, A. K., *Chem. Phys. Lett.*, **2004**, 387, 2.
41. Qin, D.; Tang, W., *RSC Adv.*, **2016**, 6, 45376.
42. Volkov, V.; Cascales, C.; Kling, A.; Zaldo, C., *Chem. Mater.* **2005**, 17, 291.
43. Huang, X., *Chin. Opt. Lett.*, **2010**, 8, 780.
44. He, D.; Guo, C.; Zhou, S.; Zhang, L.; Yang, Z.; Duan, C.; Yin, M., *CrystEngComm*, **2015**, 17, 7745.
45. Stedman, N. J.; Cheetham, A. K.; Battle, P. D., *J. Mater. Chem.*, **1994**, 4, 707.
46. Li, L.; Dong, D.; Zhang, J.; Zhang, C.; Jia, G., *Mater. Lett.*, **2014**, 131, 298.
47. Li, L.; Zi, W.; Li, G.; Lan, S.; Ji, G.; Gan, S.; Zou, H.; Xu, X., *J. Solid State Chem.*, **2012**, 191, 175.
48. Chen, D.; Liu, S.; Zhou, Y.; Wan, Z.; Huang, P.; Ji, Z., *J. Mater. Chem., C* **2016**, 4, 9044.

49. Perera, S. S.; Rabuffetti, F. A., *CrystEngComm*, **2016**, 18, 5818.
50. Grebenkemper, J. H.; Bocarsly, J. D.; Levin, E. E.; Seward, G.; Heikes, C.; Brown, C.; Misra, S.; Seeler, F.; Schierle-Arndt, K.; Wilson, S. D.; Seshadri, R., *ACS App. Mater. Inter.*, **2018**, 10, 7208.
51. Wade, S. A.; Collins, S. F.; Baxter, G. W., *J. App. Phys.*, **2003**, 94, 4743.
52. Kusama, H.; Sovers, O. J.; Yoshioka, T., *Jpn. J. Appl. Phys.*, **1976**, 15, 2349.
53. Wang, X.; Liu, Q.; Bu, Y.; Liu, C.-S.; Liu, T.; Yan, X., *RSC. Adv.*, **2015**; 5, 86219.
54. Dramićanin, M., *Methods, Materials, and Applications*, Woodhead Publishing **2018**.
55. Wang, J.; Bu, Y.; Wang, X.; Seo, H. J. *Sci. rep.*, **2017**,6023.
56. Teller, R., *Acta Crystallogr. C*, **1992**, 48, 2101.
57. Brübach, J.; Kissel, T.; Frotscher, M.; Euler, M.; Albert, B.; Dreizler, A., *J. Lumin.*, **2011**, 131, 559.
58. Xu, W.; Zhao, H.; Li, Y. X.; Zheng, L. J.; Zhang, Z. G.; Cao, W. W., *Sens. Actuators B-Chem.*, **2013**, 188, 1096.
59. Efremov, V. A.; Trunov, V. K.; Berezina, T. A., *Kristallografiya*, **1982**, 27, 134.
60. Zhang, Z. Y.; Grattan, K. T. V.; Palmer, A. W.; Meggitt, B. T., *Revi. Sci. Instrum.*, **1997**, 68, 2759.
61. Yang, X.; Fu, Z.; Yang, Y.; Zhang, C.; Wu, Z.; Sheng, T., *J. Am.Ceram. Soc.* **2015**, 98, 2595.
62. Savchuk, O. A.; Carvajal, J. J.; Pujol, M. C.; Barrera, E. W.; Massons, J.; Aguilo, M.; Diaz, F., *J. Phys. Chem. C* **2015**, 119, 18546.
63. Thompson, P.; Cox, D. E.; Hastings, J. B., *J. Appl. Crystallog.*, **1987**, 20, 79.
64. Pan, J.; Yau, L.-z.; Chen, L.-g.; Zhao, G.-w.; Zhou, G.-e.; Guo, C.-x., *J. Lumin.*, **1988**, 40-41, 856.

65. Shannon, R., *Acta Crystallog. A*, **1976**, 32, 751.
66. Ryba-Romanowski, W.; Dominiak-Dzik, G.; Solarz, P.; Lisiecki, R., *Opt. Mater.*, **2009**, 31, 1547.
67. Xu, W.; Song, Q.; Zheng, L.; Zhang, Z.; Cao, W., *Opt. Lett.*, **2014**, 39, 4635.
68. Nagli, L.; Bunimovich, D.; Katzir, A.; Gorodetsky, O.; Molev, V., *J. Non-Cryst. Solids*, **1997**, 217, 208.
69. Lupei, A.; Lupei, V.; Gheorghe, C.; Ikesue, A.; Enculescu, M., *J. Appl. Phys.* **2011**, 110, 083120.
70. Nikolić, M. G.; Jovanović, D. J.; Dramićanin, M. D., *Appl. Opt.* **2013**, 52, 1716.
71. Arakcheeva, A.; Logvinovich, D.; Chapuis, G.; Morozov, V.; Eliseeva, S. V.; Bunzli, J. C. G.; Pattison, P., *Chem. Sci.*, **2012**, 3, 384.
72. Culver, S. P.; Brutchey, R. L., *CrystEngComm.*, **2016**, 18, 4485.
73. Rabuffetti, F. A.; Culver, S. P.; Suescun, L.; Brutchey, R. L., *Inorg. Chem.*, **2014**, 53, 1056.
74. Antić, Ž.; Dramićanin, M. D.; Prashanthi, K.; Jovanović, D.; Kuzman, S.; Thundat, T., *Adv. Mater.*, **2016**, 28, 7745.
75. Đaćanin Far, L.; Lukić-Petrović, S. R.; Đorđević, V.; Vuković, K.; Glais, E.; Viana, B.; Dramićanin, M. D., *Sen. Actuators A-Physical*, **2018**, 270, 89.
76. Boruc, Z.; Kaczkan, M.; Fetlinski, B.; Turczynski, S.; Malinowski, M., *Opt. Lett.* **2012**, 37, 5214.
77. Hertle, E.; Chepyga, L.; Batentschuk, M.; Will, S.; Zigan, L., *J. Lumin.*, **2018**, 204, 64.
78. Arakcheeva, A.; Logvinovich, D.; Chapuis, G.; Morozov, V.; Eliseeva, S. V.; Bunzli, J.-C. G.; Pattison, P., *Chem. Sci.*, **2012**, 3, 384.
79. Nakazawa, E.; Shionoya, S., *Phys. Rev. Lett.*, **1970**, 25, 1710.

80. Rietveld, H. M., *J. Acta Crystallogr.* **1967**, 22, 151.
81. Rietveld, H. M., *J. Appl. Crystallogra.*, **1969**, 2, 65.
82. Larson, A. C.; Von Dreele, R. B. *General Structure Analysis System (GSAS)*; Los Alamos National Laboratory, **2000**.
83. Toby, B. H., *J. Appl. Crystallogra.* **2001**, 34, 210.
84. Auzel, F., *Comptes Rendus Hebdomadaires Des Seances De L'Academie Des Sciences Serie B*, **1966**, 263, 1016.
85. Auzel, F., *Comptes Rendus Hebdomadaires Des Seances De L'Academie Des Sciences Serie B*, **1966**, 262, 1016.
86. Auzel, F.; Meichenin, D.; Pelle, F.; Goldner, P., *Opt. Mater.*, **1994**, 4, 35.
87. Goldner, P.; Schaudel, B.; Prassas, M.; Auzel, F., *J. Lumin.*, **2000**, 87, 688.
88. Schaudel, B.; Goldner, P.; Prassas, M.; Auzel, F., *J. Alloys and Compd.*, **2000**, 300, 443.
89. Suyver, J. F.; Aebischer, A.; García-Revilla, S.; Gerner, P.; Güdel, H. U., *Phys. Rev. B.*, **2005**, 71, 125123.
90. Johnson, L. F.; Guggenheim, H. J.; Rich, T. C.; Ostermayer, F. W., *J. Appl. Phys.* **1972**, 43, 1125.
91. Stecher, J. T.; Rohlifing, A. B.; Therein, M. J., *Nanomaterials*, **2014**, 4, 69.
92. Mita, Y.; Ide, T.; Katase, T.; Yamamoto, H., *J. Lumin.* **1997**, 72, 959.
93. Auzel, F., *Chem. Rev.*, **2004**, 104, 139.
94. Pollnau, M.; Gamelin, D. R.; Lüthi, S. R.; Güdel, H. U.; Hehlen, M. P., *Phys. Rev. B.*, **2000**, 61, 3337.
95. Auzel, F.; Goldner, P., *Opti. Mater.*, **2001**, 16, 93.

96. dos Santos, P. V.; Vermelho, M. V. D.; Gouveia, E. A.; de Araújo, M. T.; Gouveia-Neto, A. S.; Cassanjes, F. C.; Ribeiro, S. J. L.; Messaddeq, Y., *J. Chem. Phys.*, **2002**, 116, 6772.
97. Maciel, G. S.; Biswas, A.; Kapoor, R.; Prasad, P. N., *Appl. Phys. Lett.*, **2000**, 76, 1978.
98. Goldner, P.; Pellé, F.; Meichenin, D.; Auzel, F., *J. Lumin.*, **1997**, 71, 137.
99. Cheng, Y.; Gao, Y.; Lin, H.; Huang, F.; Wang, Y., *J. Mater. Chem. C.*, **2018**, 6, 7462.
100. Sameera Perera, S.; A. Rabuffetti, F., *J. Mater. Chem. C.*, **2019**, 7, 7601.
101. Liu, X.; Li, Y.; Aidilibike, T.; Guo, J.; Di, W.; Qin, W., *J. Lumin.*, **2017**, 185, 247.
102. Streck, W.; Dereń, P. J.; Bednarkiewicz, A.; Kalisky, Y.; Boulanger, P., *J. Alloys Compd.*, **2000**, 300, 180.
103. Wang, H.; Duan, C.-k.; Tanner, P. A., *J. Phys. Chem. C.*, **2008**, 112, 16651.
104. Qiao, X.; Tsuboi, T.; Seo, H., *J. Alloys Compd.*, **2016**, 687, 179.
105. Dwivedi, Y.; Thakur, S. N.; Rai, S. B., *Appl. Phys. B.*, **2007**, 89, 45.
106. Toby, B., *J. Appl. Crystallogr.* **2001**, 34, 210.
107. Witkowski, D.; Rothamer, D. A., *J. Lumin.*, **2017**, 192, 1250.
108. Jubera, V.; Garcia, A.; Chaminade, J. P.; Guillen, F.; Sablayrolles, J.; Fouassier, C., *J. Lumin.*, **2007**, 124, 10.
109. Gao, Y.; Huang, F.; Lin, H.; Xu, J.; Wang, Y., *Sens. Actuators B: Chemical*, **2017**, 243, 137.
110. Gao, Y.; Huang, F.; Lin, H.; Zhou, J.; Xu, J.; Wang, Y., *Adv. Funct. Mater.*, **2016**, 26, 3139.
111. Pawar, P. P.; Munishwar, S. R.; Gedam, R. S., *J. Alloys Compd.*, **2016**, 660, 347.
112. Struck, C. W.; Fonger, W. H., *J. Appl. Phys.*, **1971**, 42, 4515.
113. Cavalli, E.; Boutinaud, P.; Bettinelli, M.; Dorenbos, P., *J. Solid State Chem.*, **2008**, 181, 1025.
114. Donega, C. d. M.; Schenker, S.; Folkerts, H. F.; Meijerink, A.; Blasse, G., *J. Phys. Condens. Matter*, **1994**, 6, 6043.

115. Wei, Y.; Tu, C.; Wang, H.; Yang, F.; Jia, G.; You, Z.; Lu, X.; Li, J.; Zhu, Z.; Wang, Y., *J. Alloys Compd.*, **2007**, 438, 310.
116. Guo, W.; Lin, Y.; Gong, X.; Chen, Y.; Luo, Z.; Huang, Y., *J. Appl. Phys.*, **2008**, 104, 053105.
117. De Mello Donegá, C.; Meijerink, A.; Blasse, G., *J. Phy. Chem. Solids*, **1995**, 56, 673.
118. Ramakrishnan, V.; Dhas, G. A.; Narayanan, P. S., *J. Raman Spectrosc.*, **1986**, 17, 273.
119. Tang, W.; Wang, S.; Li, Z.; Sun, Y.; Zheng, L.; Zhang, R.; Yang, B.; Cao, W.; Yu, M., *Appl. Phys. Lett.*, **2016**, 108, 061902.
120. Lei, R.; Luo, X.; Yuan, Z.; Wang, H.; Huang, F.; Deng, D.; Xu, S., *J. Lumin.*, **2019**, 205, 440.
121. Wei, T.; Haiyong, N.; QiuHong, Z.; Jianhong, D., *RSC Adv.*, **2018**, 8, 23996.

## APPENDIX A. PERMISSION/LICENSE AGREEMENTS FOR COPYRIGHTED MATERIALS

Permission for: *J. Mater. Chem. C*, **2019**, **7**, 7601–7608 Copyright 2019, The Royal Society of Chemistry. The Royal Society of Chemistry authors do not require to obtain official permission to reproduce the content of published papers in their own dissertation as long as appropriate acknowledgment is given.



## **APPENDIX B. PERMISSION/LICENSE AGREEMENTS FOR COPYRIGHTED MATERIALS**

Permission for: *CrystEngComm* **2016**, 18, 5818–5825 Copyright 2016, The Royal Society of Chemistry. The Royal Society of Chemistry authors do not require to obtain official permission to reproduce the content of published papers in their own dissertation as long as appropriate acknowledgment is given.

**ABSTRACT****RARE-EARTH-ACTIVATED GROUP VI  $d^0$  METAL OXIDES AS  
THERMOSENSITIVE PHOSPHORS**

by

**SAMARAGE SAMEERA PRASAD PERERA****DECEMBER 2019****Advisor:** Dr. Federico A. Rabuffetti**Major:** Chemistry**Degree:** Doctor of Philosophy

Thermosensitive phosphors are solid-state materials that demonstrate distinct dependence of luminescence emission on temperature. These materials enable optical temperature sensing in environments where conventional thermometry is not possible (e.g., gas turbines, combustion engines, surface temperature distributions). However, the design of thermosensitive phosphors that show adequate sensitivity and low thermal quenching in the intermediate temperature range (i.e., 500–1000 K) remains challenging. This challenge can be addressed by understanding how to rationally manipulate the phosphor's chemical composition and the crystal structure to tailor their thermometric response. With the aim of bridging this knowledge gap, this dissertation presents an investigation of the temperature-dependent luminescence response of a series of chemically and structurally tunable phosphors. Solid-state synthesis, structural characterization, and temperature-dependent luminescence response of rare-earth-activated scheelite and scheelite-related phosphors are presented to this end. Thermometric response of a series of Dy<sup>3+</sup>-activated NaLa(MO<sub>4</sub>)<sub>2</sub> and Na<sub>5</sub>La(MO<sub>4</sub>)<sub>4</sub> single-emitter phosphors in 300–700 K temperature range was investigated. Their potential as thermosensitive phosphors were revealed. Dual-emitter phosphors featuring two rare-

earth ions with different thermal quenching characteristics were developed. Upon investigating their thermometric response, the advantage of using dual-emitter phosphors over single-emitter phosphors to overcome the effect of thermal quenching on relative sensitivity was revealed. Finally, the importance of coupling rare-earth and transition metal ions to develop dual-emitter phosphors to improve the thermometric sensitivity and exploring new host for thermosensitive phosphors was highlighted.

## AUTOBIOGRAPHICAL STATEMENT

### SAMARAGE SAMEERA PRASAD PERERA

#### EDUCATION

**Wayne State University, MI, USA** 2014–2019

Ph.D. (Inorganic Chemistry)

Advisor: Prof. Federico A. Rabuffetti

Thesis title: “Rare-Earth-Activated Group VI  $d^0$  Metal Oxides as Thermosensitive Phosphors”

**University of Sri Jayewardenepura, Sri Lanka** 2012–2014

M.Sc., Chemistry (Polymer Chemistry and Technology)

Advisor: Prof. S. D. M. Chinthaka

Thesis title: “Synthesis and Characterization of Polyvinyl Alcohol–g–Fulvic Acid Hydrogel and its Applications in the Removal of Heavy Metal Ions from Aqueous Solutions”

**University of Sri Jayewardenepura, Sri Lanka** 2006–2010

B.Sc., Chemistry (Materials Chemistry/Polymer Chemistry)

First Class Honors degree

#### PUBLICATIONS

5. **Perera, S.S.** and Rabuffetti, F.A. “Dysprosium-Activated Scheelite-Type Oxides as Thermosensitive Phosphors.” *J. Mater. Chem. C.*, **2019**, 7, 7601-7608.
4. Shumaker, F.A.; **Perera, S.S.**; Fennell, C.J.; Rabuffetti, F.A.; Kelterer, A. M.; and Weinert, C.S. “Structural Origin of the Broadband Blue Emission in the Hexagermane  $\text{Pr}^3\text{Ge}(\text{GePh}_2)_4\text{GePr}^3$ ”. Submitted.
3. **Perera, S.S.**; Dissanayake, K.T.; and Rabuffetti, F.A. “Temperature-Dependent Luminescence Response of Er:Yb:SrFX (X = Cl, Br) Upconverting Nanocrystals”. *Journal of Luminescence* **2019**, 207, 416-423.
2. **Perera, S.S.**; Amarasinghe, D.K.; Dissanayake, K.T.; and Rabuffetti, F.A. “Average and Local Crystal Structure of  $\beta$ -Er:Yb:NaYF<sub>4</sub> Upconverting Nanocrystals Probed by X-ray Total Scattering”. *Chemistry of Materials* **2017**, 29, 6287- 6297.
1. **Perera, S.S.** and Rabuffetti, F.A. "NIR-to-NIR and NIR-to-Blue Light Upconversion in Stoichiometric NaYb(MO<sub>4</sub>)<sub>2</sub> (M = Mo, W)". *CrystEngComm* **2016**, 18, 5818-5825.

#### AWARDS

- Esther and Stanley Kirschner Graduate Award in Inorganic Chemistry, Wayne State University, **2019**.
- Thomas C. Rumble University Graduate Fellowship, Department of Chemistry, Wayne State University, **2018**.
- Joseph Jasper Scholarship for Graduate Students in Chemistry, Wayne State University, **2018**.
- Graduate School Citation for Excellence in Teaching, Department of Chemistry, Wayne State University, **2018**.
- Herbert K. Livingston Award for Excellence as a Teaching Assistant in Chemistry, Wayne State University, **2016**.